

**CORRECTION, VALIDATION, AND
CHARACTERIZATION OF MOTION IN
RESTING-STATE FUNCTIONAL MAGNETIC
RESONANCE IMAGES OF PEDIATRIC PATIENTS**

by

Jenna Marie Schabdach

B. S. Electrical Engineering, Drexel University, 2016

M. S. Electrical Engineering, Drexel University, 2016

M. S. Biomedical Informatics, University of Pittsburgh, 2018

Submitted to the Graduate Faculty of
the Department of Biomedical Informatics in partial fulfillment
of the requirements for the degree of

Doctor of Philosophy

University of Pittsburgh

2020

UNIVERSITY OF PITTSBURGH

SCHOOL OF MEDICINE

This dissertation was presented

by

Jenna Marie Schabdach

It was proposed on

March 31, 2020

and approved by

Dr. Douglas Landsittel, Department of Biomedical Informatics

Dr. Ashok Panigrahy, Department of Biomedical Informatics

Dr. Gregory Cooper, Department of Biomedical Informatics

Dr. Rafael Ceschin, Department of Pediatric Radiology, Children's Hospital of Pittsburgh

of UPMC

Dissertation Director: Dr. Douglas Landsittel, Department of Biomedical Informatics

CORRECTION, VALIDATION, AND CHARACTERIZATION OF MOTION IN RESTING-STATE FUNCTIONAL MAGNETIC RESONANCE IMAGES OF PEDIATRIC PATIENTS

Jenna Marie Schabdach, PhD

University of Pittsburgh, 2020

Approximately 1.35 million children are diagnosed with a congenital heart defect (CHD) annually. As the process of diagnosing and treating CHD has improved, the expected lifespan of CHD patients has increased: at least 12 to 34 million adults worldwide have CHD. A larger population living with CHD means that clinicians are learning more about conditions which CHD patients are at increased risk of getting. Some of these conditions affect the patient's neurodevelopment and neurocognitive status. Diagnosis of the neurocognitive conditions is performed using surveys, but examining the structure and function of the brain could offer more objective diagnoses.

One tool useful for examining a patient's brain is magnetic resonance imaging (MRI). Resting state functional MRI (rs-fMRI) in particular can be used to reveal information about the neuronal networks in the patient's brain. Unfortunately, rs-fMRIs are highly susceptible to motion. Clinical and behavioral techniques can help patients move less during a rs-fMRI scan, though they do not guarantee motion-free images. Various sensors can be used to monitor and correct for motion during the scan, but these sensors are useless when it comes to recovering previously acquired rs-fMRIs corrupted by motion.

We devised a novel approach to volume registration, which is the first step in motion correction. We compare it to traditional volume registration in the context of a complete motion correction pipeline. The registration techniques and pipeline were applied to neurological rs-fMRIs of fetal, neonatal, preadolescent, and adult patients with CHD as well as

several phantom images. We identified different motion patterns specific to different demographic groups, and discovered relationships between certain motion patterns and clinical outcomes associated with CHD and different neurodevelopmental conditions.

TABLE OF CONTENTS

1.0 INTRODUCTION	1
1.1 Resting-state Functional Magnetic Resonance Images	1
1.2 Motion Effects, Prevention, and Correction	3
1.3 Data	4
1.4 Experiments	5
1.5 Summary	6
2.0 RS-FMRIS AND PATIENT MOTION	8
2.1 Structure of an rs-fMRI	8
2.2 Confounds in rs-fMRIs	9
2.3 Effects of Patient Motion	11
2.3.1 The Positional Effects of Motion	12
2.3.2 The Spin History Effects of Motion	12
2.3.3 The Susceptibility Effects of Motion	13
2.4 Measuring Motion	14
2.4.1 Measuring Motion: Patient Position	14
2.4.2 Measuring Motion: Spurious Signal Correlations	15
2.4.3 Acceptable Motion Quantities	16
2.5 Motion Prevention	17
2.5.1 Pre-Scan: Education	17
2.5.2 During Scan: Sedation	19
2.5.3 During Scan: Feed and Sleep Protocols	21
2.6 Prospective Motion Correction	22

2.6.1	Optical Motion Correction	22
2.6.2	Non-Visual External Sensors	25
2.6.3	Image Signal Motion Monitoring	26
2.6.4	General Limitations of Prospective Motion Correction	27
2.7	Retrospective Motion Correction	27
2.7.1	Volume Registration	27
2.7.2	Denoising	30
2.7.3	Filtering	32
2.7.4	Spin History Distortion Correction	33
2.8	Summary	33
3.0	METHODS: MOTION CORRECTION	35
3.1	Directed Acyclic Graph Based Volume Registration	35
3.2	Independent Component Analysis	38
3.3	Motion Correction Pipeline and Implementation	42
3.4	Evaluating Registered and Motion Corrected Sequences Against Gold Stan- dard Usability Thresholds	42
4.0	METHODS: EVALUATING MOTION PATTERNS	44
4.1	Measuring Motion Patterns	44
4.1.1	Dice Coefficient	44
4.1.2	Correlation Ratio Matrix	46
4.1.3	Mutual Information	48
4.1.4	Implementation: Tools and Libraries	50
4.2	Patient Classification Using Motion Patterns	50
4.2.1	K-means Clustering	52
4.2.2	Spectral Clustering	53
4.2.3	Agglomerative Clustering	56
4.2.4	Visualizing Clustering Results	58
4.3	Predicting Patient Outcomes Using Motion Patterns	60
4.3.1	Regression	62
4.3.2	Support Vector Machine	63

4.3.3	LSTM Recurrent Neural Network	64
4.3.4	Application of Supervised Machine Learning	67
4.4	Describing Motion Patterns	69
5.0	DATA	70
5.1	Simulated Sequences	70
5.1.1	Background	71
5.1.2	SPECTr: Simulated Phantom Emulating Cranial Transformations	72
5.1.3	Materials	72
5.1.4	Simulation Pipeline	73
5.1.4.1	Baseline Sequence	73
5.1.4.2	Brain Signal	75
5.1.4.3	Scanner Noise	76
5.1.4.4	Patient Movement	78
5.1.5	Implementation	80
5.1.6	Simulated Sequences Experiments	80
5.2	Clinical Cohorts	81
5.2.1	CHD Background	81
5.2.2	Study Cohorts	86
5.2.2.1	Fetal Subject Population and Images	86
5.2.2.2	Neonatal Subject Population and Images	91
5.2.2.3	Preadolescent Subject Population and Images	94
5.3	Summary	97
6.0	RESULTS	99
6.1	Simulated Data	100
6.1.1	Volume Registration: Power Thresholds	100
6.1.2	Volume Registration: Sequence Duration Motion	101
6.1.3	Volume Registration: Recovered Signal	102
6.2	Preadolescent Cohort	103
6.2.1	Volume Registration: Power Thresholds	103
6.2.2	Volume Registration: Sequence Duration Motion	105

6.3	Neonatal Cohort	105
6.3.1	Volume Registration: Power Thresholds	105
6.3.2	Volume Registration: Sequence Duration Motion	105
6.4	Fetal Cohort	105
6.4.1	Brain	105
6.4.1.1	Volume Registration: Power Thresholds	106
6.4.1.0	Volume Registration: Sequence Duration Motion	106
6.4.2	Placenta	106
6.4.2.1	Volume Registration: Power Thresholds	106
6.4.0.0	Volume Registration: Sequence Duration Motion	106
6.5	Characterizing Motion	106
6.5.1	Age Groups	106
6.5.2	CHD and Control	125
7.0	DISCUSSION	127
7.1	Cohort-Level Analysis	127
7.1.1	Simulated Cohort	128
7.1.2	Preadolescent Cohort	128
7.1.3	Neonatal Cohort	128
7.1.4	Fetal Cohort	128
7.2	Lifespan Analysis	128
7.3	Relation to Existing Work	129
8.0	CONCLUSIONS	130
8.1	Limitations	130
8.2	Future Work	130
8.2.1	Adult Subject Population and Images	130
APPENDIX A. VOLUME REGISTRATION PARAMETERS		131
APPENDIX B. COMPREHENSIVE SELECTION OF RESULTS TABLES		
AND FIGURES		135
B.1	Simulated Data	135
B.1.1	Volume Registration: Power Thresholds	135

B.1.2	Volume Registration: Sequence Duration Motion	138
B.1.3	Volume Registration: Recovered Signal	142
B.2	Preadolescent Cohort	144
B.2.1	Volume Registration: Power Thresholds	144
B.2.2	Volume Registration: Sequence Duration Motion	149
B.3	Neonatal Cohort	153
B.3.1	Volume Registration: Power Thresholds	153
B.3.2	Volume Registration: Sequence Duration Motion	157
B.4	Fetal Cohort	160
B.4.1	Brain	160
B.4.1.1	Volume Registration: Power Thresholds	160
B.4.1.2	Volume Registration: Sequence Duration Motion	165
B.4.2	Placenta	169
B.4.2.1	Volume Registration: Power Thresholds	169
B.4.2.2	Volume Registration: Sequence Duration Motion	173
B.5	Characterizing Motion	177
B.5.1	Age Groups	177
B.5.2	CHD and Control	179
BIBLIOGRAPHY		181

LIST OF TABLES

1	An example of a truth table for a binary classifier predicting the presence or absence of a condition.	68
2	The number of CHD and healthy control preadolescent subjects scanned on each scanner type at each site.	96
3	The number and percentage of image volumes across all sequences in the simulated cohort which meet the usability thresholds of FD <0.2 mm and DVARS <2.5%.	108
4	The average true and false rates for both positive and negative voxels when comparing the IC component with the largest correlation to the DMN ROI over each simulated image.	110
5	The p-values determining whether the true and false rates for both positive and negative voxels differ between the traditionally registered and DAG-registered simulated sequences as calculated using the two-sided t-test.	110
6	The number of preadolescent subjects whose sequences of types S_1 and S_2 had different MI distributions.	112
7	The number of preadolescent subjects whose sequences of types S_1 and S_2 had different Dice distributions.	113
8	The number and percentage of image volumes across all sequences in the neonatal cohort which meet the usability thresholds of FD <0.2 mm and DVARS <2.5%.	115
9	The number of neonatal subjects whose sequences of types S_1 and S_2 had different MI distributions.	116

10	The number of neonatal subjects whose sequences of types S_1 and S_2 had different Dice distributions.	117
11	The number and percentage of image volumes across all sequences in the fetal brain image data set which meet the usability thresholds of $FD < 0.2$ mm and $DVARS < 2.5\%$	119
12	The number of subjects whose sequences of types S_1 and S_2 had different MI distributions.	120
13	The number and percentage of image volumes across all sequences in the fetal placenta image data set which meet the usability thresholds of $FD < 0.2$ mm and $DVARS < 2.5\%$	122
14	Results from the t-tests comparing the counts for the numbers of images meeting the FD , $DVARS$, and FD and $DVARS$ thresholds for sequence type S_1 and sequence type S_2	136
15	The number of subjects whose sequences of types S_1 and S_2 had different FD distributions.	136
16	The number of subjects whose sequences of types S_1 and S_2 had different $DVARS$ distributions.	137
17	Results of t-tests comparing the descriptive statistics of the correlation ratio matrices for the simulated data.	139
18	Results of t-tests comparing the descriptive statistics of the Dice matrices for the simulated data.	140
19	Results of t-tests comparing the descriptive statistics of the MI matrices for the simulated data.	141
20	The average true and false rates for both positive and negative voxels when comparing the IC component with the largest correlation to the DMN ROI over each simulated image.	142
21	The p-values determining whether the true and false rates for both positive and negative voxels differ between the traditionally registered and DAG-registered simulated sequences as calculated using the two-sided t-test.	143

22	The number and percentage of image volumes across all sequences in the preadolescent cohort which meet the usability thresholds of FD <0.2 mm and DVARS $<2.5\%$	146
23	Results from the t-tests comparing the counts for the numbers of images meeting the FD, DVARS, and FD and DVARS thresholds for sequence type S_1 and sequence type S_2	146
24	The number of subjects whose sequences of types S_1 and S_2 had different FD distributions.	147
25	The number of subjects whose sequences of types S_1 and S_2 had different DVARS distributions.	147
26	Results of t-tests comparing the descriptive statistics of the Dice matrices for the preadolescent data.	150
27	Results of t-tests comparing the descriptive statistics of the MI matrices for the preadolescent data.	151
28	The number of preadolescent subjects whose sequences of types S_1 and S_2 had different MI distributions.	152
29	The number of preadolescent subjects whose sequences of types S_1 and S_2 had different Dice distributions.	152
30	The number and percentage of image volumes across all sequences in the neonatal cohort which meet the usability thresholds of FD <0.2 mm and DVARS $<2.5\%$	155
31	Results from the t-tests comparing the counts for the numbers of images meeting the FD, DVARS, and FD and DVARS thresholds for sequence type S_1 and sequence type S_2	155
32	The number of subjects whose sequences of types S_1 and S_2 had different FD distributions.	156
33	The number of subjects whose sequences of types S_1 and S_2 had different DVARS distributions.	156
34	Results of t-tests comparing the descriptive statistics of the Dice matrices for the neonatal cohort.	158

35	Results of t-tests comparing the descriptive statistics of the MI matrices for the neonatal data.	159
36	The number of neonatal subjects whose sequences of types S_1 and S_2 had different MI distributions.	160
37	The number of neonatal subjects whose sequences of types S_1 and S_2 had different Dice distributions.	161
38	The number and percentage of image volumes across all sequences in the fetal brain image data set which meet the usability thresholds of $FD < 0.2$ mm and $DVARS < 2.5\%$	163
39	Results from the t-tests comparing the counts for the numbers of images meeting the FD , $DVARS$, and FD and $DVARS$ thresholds for fetal brain sequence type S_1 and sequence type S_2	163
40	The number of subjects whose sequences of types S_1 and S_2 had different FD distributions according to the Kolmogorov-Smirnov test.	164
41	The number of subjects whose sequences of types S_1 and S_2 had different $DVARS$ distributions according to the Kolmogorov-Smirnov test.	164
42	Results of t-tests comparing the descriptive statistics of the Dice matrices for the fetal brain data.	166
43	Results of t-tests comparing the descriptive statistics of the MI matrices for the fetal brain data.	167
44	The number of subjects whose sequences of types S_1 and S_2 had different MI distributions.	168
45	The number of subjects whose sequences of types S_1 and S_2 had different Dice distributions.	168
46	The number and percentage of image volumes across all sequences in the fetal placenta image data set which meet the usability thresholds of $FD < 0.2$ mm and $DVARS < 2.5\%$	171
47	Results from the t-tests comparing the counts for the numbers of images meeting the FD , $DVARS$, and FD and $DVARS$ thresholds for fetal placenta sequence type S_1 and sequence type S_2	171

48	The number of placental images whose sequences of types S_1 and S_2 had different FD distributions according to the Kolmogorov-Smirnov test.	172
49	The number of placental images whose sequences of types S_1 and S_2 had different DVARs distributions according to the Kolmogorov-Smirnov test. . . .	172
50	Results of t-tests comparing the descriptive statistics of the Dice matrices for the fetal placenta data.	174
51	Results of t-tests comparing the descriptive statistics of the MI matrices for the fetal placenta data.	175
52	The number of subjects whose placenta sequences of types S_1 and S_2 had different MI distributions.	176
53	The number of subjects whose placenta sequences of types S_1 and S_2 had different Dice distributions.	176

LIST OF FIGURES

1	A rs-fMRI can be thought of (a) as a sequence of image volumes or (b) as a single volume where each voxel contains a temporal signal rather than a single numeric value.	9
2	The patient’s brain activity effectively passes through several filters before an MRI scanner produces a visually interpretable image sequence. (The rounded rectangles represent the signal at different stages of recording while the rhombuses represent the filters.)	10
3	The traditional approach to volume registration in an rs-fMRI sequence consists of registering all volumes in the sequence to a single reference volume. .	29
4	A rs-fMRI can be viewed as a directed acyclic graph where each volume is a node and the edges connect from each volume i to the following volume $i + 1$	36
5	The traditional approach to volume registration in an rs-fMRI sequence consists of registering all volumes in the sequence to a single reference volume. .	37
6	An example of k -means clustering performed on the Iris data set. The results of the algorithm are highly dependent on the number of clusters specified. . .	51
7	(a) Two different distributions, a 2D Gaussian density and a thin horizontal rectangle are difficult to separate (b) due to their overlap and the penalties built into the cost function of the spectral clustering algorithm. From (Nadler and Galun, 2007).	55
8	An example of agglomerative clustering on the Iris data set plotted using seaborn’s clustermap function.	57

9	Visualization of MNIST data in 3D via TensorFlow Projector as generated using PCA, t-SNE, and UMAP dimensionality reduction techniques.	61
10	An overview of the SPECTr simulation pipeline. Using atlas data, a simulated phantom containing brain signal, scanner noise, and patient motion is generated.	74
11	An example of the magnitude and phase of an image in k-space.	77
12	Table of prevalences of congenital heart defects as compiled by (Mozaffarian et al., 2016).	82
13	Estimated CHD burden in World Health Organization (WHO) regions using incidence rates of approximately 12/1000 and 4/1000 in children and adults, respectively (Webb et al., 2015).	84
14	Distribution of subject races for all three cohorts.	87
15	Distribution of subject ethnicities for all three cohorts.	87
16	Distribution of subject genders for all three cohorts.	88
17	The distribution of post-conceptual ages at the time of the scan of all fetal subjects.	89
18	The outer ring represents the group the subject was assigned to based on the fetal examination while the inner ring represents the group the subject was assigned to after birth.	90
19	The distribution of post-conceptual ages at birth of all neonatal subjects.	92
20	The distribution of post-conceptual ages at the time of the scan of all neonatal subjects.	92
21	The breakdown of subject groups contained in the Control and CHD neonatal cohorts.	93
22	The distribution of preadolescent subject ages at the time of the scan.	94
23	The distribution of CHD and healthy subjects between the 12 sites enrolled in the preadolescent study.	95
24	The means and standard deviations of the FD and DVARS metrics for all simulated images both before and after registration.	107

25	Boxplots of the values of all CR matrices for the original sequences, the traditionally registered sequences, and the DAG-registered sequences for the simulated data.	108
26	Boxplots of the values of all Dice matrices for the original sequences, the traditionally registered sequences, and the DAG-registered sequences for the simulated data.	109
27	Boxplots of the values of all MI matrices for the original sequences, the traditionally registered sequences, and the DAG-registered sequences for the simulated data.	109
28	Examples of the three similarity matrices. Lighter colors represent more desirable values.	111
29	Boxplots of the values of all Dice matrices for the original sequences, the traditionally registered sequences, and the DAG-registered sequences for the preadolescent cohort.	111
30	Boxplots of the values of all MI matrices for the original sequences, the traditionally registered sequences, and the DAG-registered sequences for the preadolescent cohort.	112
31	The means and standard deviations of the FD and DVARS metrics for all neonatal images both before and after registration.	114
32	Boxplots of the values of all Dice matrices for the original sequences, the traditionally registered sequences, and the DAG-registered sequences for the neonatal cohort.	115
33	Boxplots of the values of all MI matrices for the original sequences, the traditionally registered sequences, and the DAG-registered sequences for the neonatal cohort.	116
34	The means and standard deviations of the FD and DVARS metrics for all fetal brain images both before and after registration.	118
35	Boxplots of the values of all Dice matrices for the original sequences, the traditionally registered sequences, and the DAG-registered sequences for the fetal-brain images.	119

36	Boxplots of the values of all MI matrices for the original sequences, the traditionally registered sequences, and the DAG-registered sequences for the fetal brain images.	120
37	The means and standard deviations of the FD and DVARs metrics for all placenta images both before and after registration.	121
38	Boxplots of the values of all Dice matrices for the original sequences, the traditionally registered sequences, and the DAG-registered sequences for the placenta images.	122
39	Boxplots of the values of all MI matrices for the original sequences, the traditionally registered sequences, and the DAG-registered sequences for the placenta images.	123
40	The preadolescent, neonatal, and fetal images clustered by each metric using agglomerative clustering and labeled by age group.	124
41	The preadolescent, neonatal, and fetal images clustered by each metric using agglomerative clustering and labeled by CHD/Control status.	126
42	Boxplots of the values of all CR matrices for the original sequences, the traditionally registered sequences, and the DAG-registered sequences for the simulated data.	138
43	Boxplots of the values of all Dice matrices for the original sequences, the traditionally registered sequences, and the DAG-registered sequences for the simulated data.	140
44	Boxplots of the values of all MI matrices for the original sequences, the traditionally registered sequences, and the DAG-registered sequences for the simulated data.	141
45	The means and standard deviations of the FD and DVARs metrics for all preadolescent images both before and after registration.	145
46	Examples of the three similarity matrices. Lighter colors represent more desirable values.	148

47	Boxplots of the values of all Dice matrices for the original sequences, the traditionally registered sequences, and the DAG-registered sequences for the preadolescent cohort.	149
48	Boxplots of the values of all MI matrices for the original sequences, the traditionally registered sequences, and the DAG-registered sequences for the preadolescent cohort.	151
49	The means and standard deviations of the FD and DVARs metrics for all neonatal images both before and after registration.	154
50	Boxplots of the values of all Dice matrices for the original sequences, the traditionally registered sequences, and the DAG-registered sequences for the neonatal cohort.	157
51	Boxplots of the values of all MI matrices for the original sequences, the traditionally registered sequences, and the DAG-registered sequences for the neonatal cohort.	159
52	The means and standard deviations of the FD and DVARs metrics for all fetal brain images both before and after registration.	162
53	Boxplots of the values of all Dice matrices for the original sequences, the traditionally registered sequences, and the DAG-registered sequences for the fetal-brain images.	165
54	Boxplots of the values of all MI matrices for the original sequences, the traditionally registered sequences, and the DAG-registered sequences for the fetal brain images.	167
55	The means and standard deviations of the FD and DVARs metrics for all placenta images both before and after registration.	170
56	Boxplots of the values of all Dice matrices for the original sequences, the traditionally registered sequences, and the DAG-registered sequences for the placenta images.	173
57	Boxplots of the values of all MI matrices for the original sequences, the traditionally registered sequences, and the DAG-registered sequences for the placenta images.	175

58	The preadolescent, neonatal, and fetal images clustered by each metric using agglomerative clustering and labeled by age group.	178
59	The preadolescent, neonatal, and fetal images clustered by each metric using agglomerative clustering and labeled by CHD/Control status.	180

1.0 INTRODUCTION

Patient motion is a critical cause of data loss in medical imaging. Many approaches have been developed to prevent and reduce the impact of motion before, during, and after image acquisition. The effectiveness of these techniques vary between patient populations. If the effects of a patient’s movements cannot be removed from an image, that image is considered to have been corrupted by motion and is deemed unusable.

Though patient motion is a problem across the entire medical imaging domain, we focus specifically on resting state functional magnetic resonance imaging (rs-fMRI). rs-fMRIs measure the blood oxygen level dependent signal in an organ or organ system. Areas of an organ with greater activity require more oxygen than less active areas. When used to examine the brain, the signals recorded by the rs-fMRI are used as an effective approximation of the amount of activity occurring in different areas of the brain. The term “resting state” means that the patient is not performing any particular task, so any activity that occurs is from underlying networks connecting different areas of the brain.

1.1 RESTING-STATE FUNCTIONAL MAGNETIC RESONANCE IMAGES

When an area of the brain is active, it uses more oxygen than the surrounding regions. Functional MRIs (fMRI) are sensitive to signals emitted by deoxygenated hemoglobin. The blood oxygen level dependent (BOLD) signal recorded by the fMRI reveal regions of the brain which are active at the same time. These combinations of regions are called neuronal networks.

Many neuronal networks exist, but most of them are considered to be task related. In

2001, Raichle et al. suggested the existence of a neuronal network which operated when a person is at rest (Raichle et al., 2001). Their theory was confirmed by Greicius et al. in 2003 (Greicius et al., 2003). Because the patient is not performing a specific task when they are in a resting state, the resting-state networks have the potential to reveal valuable information about a patient’s neurodevelopmental status.

To gather enough data to fully evaluate these networks, a series of image volumes must be acquired over a period of several minutes. A fMRI taken of a patient in a resting, task-free state, is called a resting-state fMRI (rs-fMRI). rs-fMRIs are sequences of image volumes acquired over a period of a few minutes. The image volumes themselves have relatively low spatial resolution when compared to structural MRIs, but their temporal resolution is significantly higher as a new volume is acquired every two to three seconds.

The BOLD signals in rs-fMRI image sequences are analyzed using a process called functional connectivity analysis. Functional connectivity analysis identifies patterns and networks of brain activity. Some functional connectivity analysis studies have led to the discoveries of links between specific disruptions in these naturally occurring networks and neurodevelopmental diseases such as autism and attention deficit hyperactivity disorder (Assaf et al., 2010) (Zang et al., 2007). With further refinements of both acquisition techniques and characterization of these functional networks, clinicians may be able to use rs-fMRI to evaluate the neurodevelopmental status of CHD patients and to identify patients who may benefit from certain therapies or neuroprotective interventions.

To gather high quality data on such a short timescale, the rs-fMRI suffers from two major limitations: rs-fMR images have low physical resolution and are highly susceptible to motion. The first limitation can be addressed by obtaining an MR image with high physical resolution and registering the rs-fMRI to this structural image, but the second limitation is a significant problem.

1.2 MOTION EFFECTS, PREVENTION, AND CORRECTION

There are three effects of motion on an rs-fMRI scan: the positional effect, the spin history effect, and the susceptibility effect. The impact of motion on the position of the patient means that a given voxel will not record electromagnetic signal from the same location in the brain for the duration of the scan. When the patient moves, the molecules which were in the area activated by the MRI scanner also move. Molecules which were not activated are now in the area where signal is being recorded, which results in a decrease in signal. At the next activation, an molecules which were moved out of the previous area of activation may be further activated, which can result in a increase in signal. These spin history effects impact the image sequence for several frames, but dissipate. The susceptibility effects impact the signal recorded by the scanner for the duration of the scan. The difference in the susceptibility of different tissues is most prominent at the tissue interfaces. When the patient moves, the tissue interfaces move and contribute or detract from the signal at new locations.

In general, the best way to prevent the effects of motion is to prevent motion itself. Various clinical, behavioral, and technical protocols have been developed in an attempt to prevent patient motion from impacting the rs-fMR image as it is acquired. Sedation can be used to immobilize a patient during a scan, but requires additional personal to perform safely and involves a greater time commitment from the patient. Sedation is also not recommended for use in young children and fetal patients. Behavioral and educational techniques can be employed to prepare a patient for stressors he may experience during a medical imaging scan, but these approaches do not prevent the patient from moving out of boredom, discomfort, or distress. Several groups have developed techniques to compensate for motion as an image is acquired, but these techniques often require additional scanner-compatible equipment and can only be utilized during the scan. Sedation or intra-scan motion monitoring approaches are difficult to integrate with MR scanners due to the constraints of MR safety requirements.

Additional processing is needed to remove motion from an image after the scan is acquired. Many methods have been developed to mitigate the effects of motion after the rs-fMRI is acquired. While different post-acquisition motion correction pipelines utilize different processing techniques, they begin with global volume registration. Global volume

registration is the process used to align all volumes in a rs-fMRI sequence into the same physical space. Traditionally, all volumes in the sequence are registered directly to one volume. This approach can be effective in images where the subject remains relatively still throughout the duration of the scan, but is not as successful in images containing high quantities of patient movement.

We have developed an alternative volume registration framework which takes into account the spatiotemporal relationships between sequential volumes in the rs-fMRI sequence and uses these relationships during the registration process. Herein, we evaluate it further in the context of a complete motion correction pipeline across healthy and disease populations at various stages of life. In addition to reducing the effects of patient motion on image quality, we are also interested in the patient motion itself. We believe there are relationships between different motion patterns, patient age, and clinical outcomes, and we have explored these relationships throughout our experiments.

1.3 DATA

The disease population we used for our study is a population with a variety of congenital heart defects. Congenital heart defects (CHDs) have many presentations, and all cause problems in a patient’s heart structure and the structure of the surrounding vessels. It has been found that the development of cardiac problems *in utero* is often linked to delays in patient neurodevelopment. Research in the area of CHD and neurodevelopment has often focused on younger populations. However, treatment of CHDs has evolved over the past fifty years with the result that many CHD patients live to adulthood: every year, approximately 1.35 million children are born with a congenital heart defect and it is currently estimated that about 12 to 34 million adults are living with CHD ([van der Linde et al., 2011](#)). Researchers have recognized the burden of neurocognitive disorders on the aging CHD population and are now starting to investigate the relationships between CHD and neurocognitive outcomes.

The process for objectively identifying neurocognitive disorders is still under development. Psychologists have developed and validated surveys to estimate a patient’s neurocog-

nitive status. These surveys vary with the child's. Initially, a parent fills out the survey on behalf of his infant or toddler child. When the child has reached certain developmental milestones, the parent and child might both fill out different portions of a different survey. At some point, the child can fill out his own survey. Psychologists may meet with the patient and his parents to determine a diagnosis. These survey based methods are highly subjective, and objective methods based on rs-fMRIs are being explored.

Eventually, clinicians will be able to develop a lifespan approach to managing CHD and neurocognitive disorders. As a community, we are still in the data-gathering stage of this research. We cannot afford to lose rs-fMRI scans of healthy or CHD patients in any stage of life because of motion. For these reasons, a cohort of healthy and CHD patient images are an ideal data set for our motion correction work.

We were able to access data from three clinical cohorts. The first cohort is a set of healthy and CHD neonatal subjects scanned at our primary study site. The second cohort is a set of healthy and CHD preadolescent subjects enrolled in a multicenter study. Some subjects were scanned at our primary study site while others were scanned at one of the 11 other participating sites. The third cohort is a set of healthy and CHD fetal subjects scanned at our primary site.

Many rs-fMRI studies struggle to obtain enough low-motion scans to come to statistically significant conclusions. We develop a tool to address this challenge by simulating rs-fMRIs using existing average brain and functional region of interest templates. The simulated sequences contain brain signal, scanner noise, and motion. We then use this tool to simulate additional images with which to test the registration frameworks and to determine the effects of volume registration on brain signal.

1.4 EXPERIMENTS

Both the traditional and novel registration techniques are applied to the clinical and simulated images. We compare the original and registered images with respect to the amount of motion removed from each sequence. We use two metrics to measure the effects of motion

and three metrics to measure the similarity of the images.

The metrics used to measure motion are the change in patient position (framewise displacement, FD) and the change in overall signal (derivative of the variance of the root mean square of the signal, DVARS) between one time point and the next. These metrics are only applied between every pair of chronological image volumes in a sequence. They are then compared to two thresholds commonly recognized in the field of motion in rs-fMRIs to determine the usability of an image sequence.

The three similarity metrics are the correlation ratio, the mutual information, and the Dice coefficient. The similarity metrics are used to compare every volume in a sequence to every other volume in the same sequence, which produces a two-dimensional matrix for each metric. Changes in the patterns of the matrices for the same metrics for the same images are used to determine the overall impact of registration on the similarities between volumes in an image sequence.

While correcting motion within an rs-fMRI is important both for clinical use and research applications, we are also interested in the motion itself. Through discussion with radiologists and researchers who work with rs-fMRIs, we have developed the following hypothesis: **Neonatal patients on average exhibit less motion than preadolescent patients, who exhibit less motion than fetal patients.** We evaluate this hypothesis using unsupervised machine learning techniques to identify clusters of similar patients. The unsupervised machine learning techniques will also be applied to age group level cohorts to identify patients with common patterns of motion in each cohort.

1.5 SUMMARY

The remainder of this document is laid out as follows. We elaborate on resting-state functional magnetic resonance images (rs-fMRIs) and their use for investigating functional brain networks in Chapter 2. In Chapter 3, we perform a breadth-wise review of the effects of motion, methods to prevent motion, and methods to mitigate the effects of motion. Chapter 4 transitions into methods for analyzing MRIs, machine learning techniques, and our approach

to statistical analysis.

Chapter 5 discusses congenital heart disease, its relationship with neurological conditions, and methods for evaluating neurological conditions. It also contains information about the scans and demographics information for each clinical cohort as well as details about the simulation.

Chapter 6 contains the results of our experiments and statistical analyses for the registration experiments and the machine learning experiments. Chapter 7 contains a discussion of these results, and Chapter 8 contains a metadiscussion of this study as a whole.

2.0 RS-FMRIS AND PATIENT MOTION

This chapter discusses rs-fMRIs and how they are affected by patient motion. Specific topics include the structure of rs-fMRIs, sources of motion, quantifying motion, and a review of current methods for preventing and managing motion in rs-fMRIs.

2.1 STRUCTURE OF AN RS-FMRI

rs-fMRIs are discrete representations of continuous data. A new image volume of the patient’s brain is acquired every two to three seconds. The image volume is composed of a three dimensional version of a pixel called a voxel (volume element). Just as the “distance” between each image volume encompasses a certain amount of time, each voxel encompasses a small volume of physical space. The transformations between the continuous physical and temporal dimensions and the discrete physical and temporal dimensions are the spatial and temporal resolutions. The concept of a 4D rs-fMR image is illustrated in two different ways in Figure 1. The first representation is an ordered list of 3D image volumes where each voxel contains a single numeric value. The second representation is a single 3D image volume where the value of each voxel is a temporal signal.

An rs-fMRI is considered to have relatively low spatial resolution but high temporal resolution. The physical size of a single voxel seems small at about 4 mm^3 , but this resolution is not granular enough to capture details about activity within small structures of the brain. The activity information recorded during a rs-fMRI must be combined with the detailed anatomic information from a structural MRI to know precisely which areas of the brain are active at each point in time. A structural MRI volume takes much longer to acquire

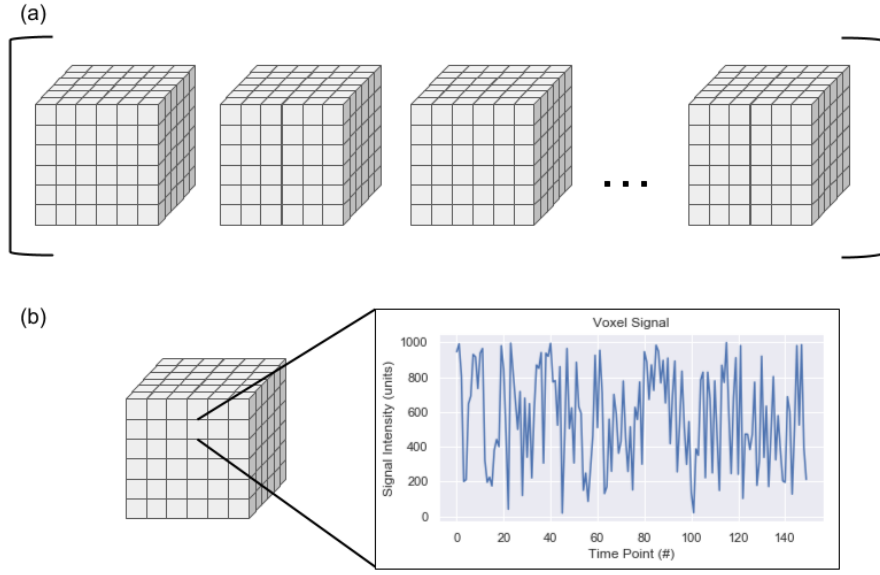


Figure 1: A rs-fMRI can be thought of (a) as a sequence of image volumes or (b) as a single volume where each voxel contains a temporal signal rather than a single numeric value.

than a rs-fMRI volume, which can be obtained every two to three seconds. Unfortunately, the patient’s position and neural activity can change faster than the image volume can be acquired. As a result, a temporal resolution of two to three seconds is not fast enough to actively compensate for sources of noise which confound the BOLD signal.

2.2 CONFOUNDS IN RS-FMRIS

The BOLD signal present inside a patient’s brain is not recorded with complete accuracy by an MRI scanner. Even if the same patient exhibited the exact same BOLD signal during two different scans, the recorded image sequences would vary slightly. There are a number of confounds that impact the image sequence viewed by a radiologist, and we give an overview of them in Figure 2.

The first filter in Figure 2 is the patient’s physiology. A rs-fMRI is not sensitive enough to

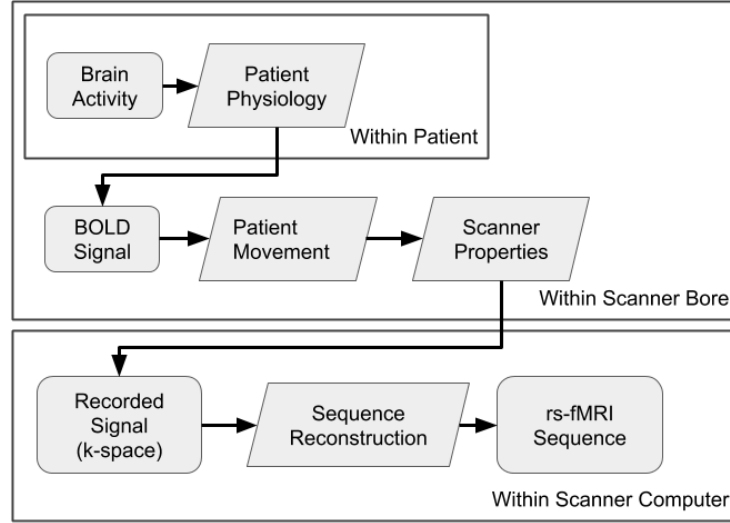


Figure 2: The patient’s brain activity effectively passes through several filters before an MRI scanner produces a visually interpretable image sequence. (The rounded rectangles represent the signal at different stages of recording while the rhombuses represent the filters.)

detect brain activity on a neuronal level. Instead, it measures the changes in the amounts of deoxygenated hemoglobin in the brain. The deoxygenated hemoglobin quantities are highly correlated with brain activity because active areas of the brain use more oxygen than inactive areas, but this BOLD signal is still only an approximation of brain activity.

The second filter in Figure 2 is changes to the signal that occur due to patient motion. During every medical imaging scan, the patient will naturally perform small, automatic movements due to regular bodily functions. Minuscule movements caused by cardiac activity may disrupt scans with high spatial resolution or with high sensitivity to the movement of blood molecules. Larger movements caused by respiration result in motion artifacts in images of the thoracic and abdominal cavities.

Other motions occur on a larger and more conscious scale. It is important to note that different populations may exhibit more of certain macro-motions than others. The patient may fidget or shift his gaze when he becomes bored in the scanner. If the patient falls asleep during a scan, there may be slight movement as the body relaxes and retenses if

the patient wakes. Certain MRI protocols are known to produce loud sounds: during one of these protocols, the patient may become surprised and react by jumping. Additionally, claustrophobic patients or patients who feel secure around specific people that are not allowed in the scanner room may become agitated.

Both the small-scale, automatic motions and the large-scale, reflexive motions corrupt the BOLD signal. These effects of patient motion will be discussed in depth in the next section.

The third filter in Figure 2 is the unique properties of the scanner. The acquired image sequence will vary slightly even in machines made by the same company because each scanner has a unique primary magnetic field, B_0 . The B_0 inhomogeneities can be measured using a primary field map. These field maps can be used to correct signals displaced by the B_0 field, though they cannot be used to recover signals corrupted by the field.

The final filter is also related to the properties of the MRI scanner. The image sequence produced by a scanner is dependent on the scanner vendor. Different vendors use different proprietary algorithms to convert the signal recorded by the scanner in k-space into a visually interpretable image sequence. Between the B_0 inhomogeneities and the scanner vendor differences, the differences in the scanners used to acquire the sequences must be resolved before images from different scanners can be compared.

2.3 EFFECTS OF PATIENT MOTION

Due to their low spatial and high temporal resolutions, rs-fMRIs are highly susceptible to all types of motion outlined in the previous section. In general, motion affects an acquired image sequence in three ways. The first and most obvious effect is the position of the patient changes throughout the sequence. The second effect is due to the way changes in the patient's position affect the signal recorded by the scanner. The third effect is due to the magnetic fields in patient tissue and changes in their orientation within B_0 . These three effects will hereafter be referred to as the positional effect, the spin history effect, and the susceptibility effect of motion.

2.3.1 The Positional Effects of Motion

The technique used for analyzing neuronal network activity rs-fMRIs, called functional connectivity analysis, assumes that the contents of one voxel at every time point during the sequence all contain signal from a single point in the brain. This assumption is vital in the process of inferring networks of neuronal activity.

While rs-fMRIs have a spatial resolution on the order of millimeters, neuronal activity occurs on the spatial resolution of microns. As a result, each voxel in a rs-fMRI volume contains information from a number of neurons. The smallest movement of the patient can alter the voxel to which a cluster of neurons contributes. These seemingly insignificant changes can alter the position of the patient enough to cause the voxels to record signals from different brain regions or even tissue types. This change in voxel location within the brain violates the assumption of voxels recording from the same location within the brain for the duration of the sequence.

2.3.2 The Spin History Effects of Motion

In addition to changing the recorded position of the patient, motion impacts the established spin gradients, which introduces artifacts into the image sequence.

During an ideal MRI scan, the patient is sitting in the scanner and all molecules are aligned with the primary magnetic field B_0 in a relaxed state. Then, a radiofrequency (RF) pulse is applied to the field. The purpose of the pulse is to excite the molecules in a certain volume of physical space to orient the molecules to align to a secondary field in a different plane. When the pulse ends, the molecules precess back to their orientation in B_0 . As they do, their small magnetic fields induce electric currents on the RF coil. The currents are received by the scanner as signals in frequency space. The volume of the space intended to be excited is known, and the signal produced by the induced electric current is used in conjunction to reconstruct the image in voxel space.

However, when the patient moves, the volume of space which was thought to be excited is not actually excited: some other volume of space, which may or may not overlap with the intended volume of space, is excited instead. Because the MRI scanner has no way to know

this assumption is not true, it does not know that not all of the molecules in its intended area are relaxed and correctly aligned to the B_0 field at the end of the RF pulse. The scanner proceeds with the next RF pulse, which excites a new set of “relaxed molecules”, some of which are still excited from the previous pulse. As a result, the signals produced in the second RF pulse are different than they should be. For example, signals that are smaller than they should be result in dark shadows within motion affected volumes of the sequence.

The previous few paragraphs in this section describe how motion disrupts the magnetic spin gradients present in the patient during an rs-fMRI scan. The spin gradients need time to recover to the correct magnetic field orientation, and up to eight to ten seconds may pass before the recovery is complete (Power et al., 2014). While the spin gradients are reorienting, the recorded BOLD signal will vary more than expected between temporally neighboring volumes. These variations are more difficult to quantify than the positional effects of motion.

The nature of the B_0 field in a MRI scanner can be recorded using a field map. Acquiring a field map while the patient is in the scanner records information about how the patient interact with the B_0 field. These field maps of the patient in the scanner can be used to perform distortion correction on the acquired sequence. A study of the effects of distortion correction on rs-fMRIs of 40 healthy subjects suggested that distortion correction using field maps can increase the functional connectivity in rs-fMRIs (Togo et al., 2017).

2.3.3 The Susceptibility Effects of Motion

The susceptibility of a material describes how the material will behave when placed in a magnetic field. Most materials are either paramagnetic or diamagnetic. Paramagnetic materials are attracted to and align with magnetic fields while diamagnetic are repelled from and become anti-aligned with magnetic fields. Additionally, paramagnetic materials contribute to the magnetic field where they interact with it while diamagnetic materials detract from it.

Both types of materials cause distortions in the magnetic field. These distortions are more prominent in stronger magnetic fields and at the interface of two different material

types. In MRI scanners, the differences in susceptibility between soft tissue and bone or between soft tissue and air can produce artifacts in the acquired sequence. These artifacts are amplified when the patient moves. When the patient moves, the interfaces between tissues and air distort the B_0 field. The distortions in the B_0 field change the electromagnetic signal recorded by the scanner and lead to spurious correlations during the analysis of the rs-fMRI sequence.

Susceptibility artifacts can be reduced using susceptibility maps. Susceptibility maps are short acquisitions which use multiple echo periods to detect small changes in the location of susceptibility interfaces in a MRI sequence. They are not part of most rs-fMRI acquisition protocols.

2.4 MEASURING MOTION

Even though we described three effects of motion on rs-fMRIs in the previous section, these effects impact the sequence in two areas: the position of the patient and spurious signal correlations throughout the sequence.

2.4.1 Measuring Motion: Patient Position

The effect of motion on patient position is measured in terms of the difference in the positions of the contents of temporally neighboring image volumes. The difference in position is determined using metrics calculated by performing rigid volume registration on the two volumes. In rigid volume registration, one volume is chosen as the reference volume and the other is considered the moving volume. The reference volume remains stationary while the moving volume is translated and rotated in three-dimensional space on top of it. The registration is considered complete when the position of the patient in the moving volume matches the position in the reference volume.

The moving volume can undergo linear or nonlinear transformations. Linear transformations include translation, rotation, and affine transformations along all three spatial dimen-

sions as well as a scaling transformation. These transformations move the image volume as a whole: all voxels in the moving image remain in the same location relative to their neighbors. On the other hand, nonlinear transformations have the ability to warp the contents of the moving volume so that it better matches the contents of the reference volume. Nonlinear transformations are more complex than linear transformation. They involve additional image processing steps such as smoothing and voxel interpolation.

Even in cases when nonlinear transformations are used, the registration process begins with the translation and rotation transformations. The three translation and three rotation parameters used to achieve the best alignment are used to calculate the positional change between the image volumes. The positional change between temporally neighboring volumes is called the framewise displacement (FD).

Several researchers have proposed slightly different methods for calculating the FD. Power et al., Jenkinson et al., and Dosenbach et al. each propose a slightly different method for calculating the FD (Power et al., 2012) (Jenkinson et al., 2002) (Dosenbach et al., 2017). All three FD calculations produce correlated metrics: the FD metric proposed by Power et al. produces measurements approximately twice as large as the metric proposed by Jenkinson et al., and Dosenbach et al. reported a high correlation between their FD and Powers FD (Yan et al., 2013b) (Dosenbach et al., 2017).

In the remainder of this document, the abbreviation FD refers to Power et al.’s version of the FD metric, which is calculated as:

$$FD(J_i) = |\Delta d_{ix}| + |\Delta d_{iy}| + |\Delta d_{iz}| + |\Delta \alpha_i| + |\Delta \beta_i| + |\Delta \gamma_i| \quad (2.1)$$

where J_i is the image volume i , $|\Delta d_{i*}|$ are the magnitude of change in position along the x , y , and z axes between volumes i and $i - 1$, and $|\Delta \alpha_i|$, $|\Delta \beta_i|$, and $|\Delta \gamma_i|$ are the magnitude of change in pitch, roll, and yaw between volumes i and $i - 1$, respectively.

2.4.2 Measuring Motion: Spurious Signal Correlations

Both the spin history and susceptibility effects of motion contribute to alterations in the signal recorded and reconstructed by the MRI scanner. Without B_0 field maps and suscep-

tibility maps, it is difficult to separate the impact of each of these factors on the recorded signal. We assume at this point that both the spin history and the susceptibility effects contribute equally to changes in the recorded signal intensity.

One popular metric to measure changes in the recorded signal due to patient motion was developed by Smyser et al. in 2010. Their metric is called DVARS, which measures the temporal derivative of the root mean squared variance over the voxels between two volumes (Smyser et al., 2010). Power et al. explain the steps to calculate DVARS in a separate study (Power et al., 2012). The DVARS value is calculated in two steps. The first step uses backward differences to approximate the derivative of the BOLD signal change between volumes J_i and J_{i-1} at every point \vec{x} contained in both image volumes:

$$\frac{\partial}{\partial t} J_i(\vec{x}) \approx J_i(\vec{x}) - J_{i-1}(\vec{x}). \quad (2.2)$$

The second step calculates the root mean square of the approximated derivatives for all N points \vec{x} :

$$DVARS(J_i) = \sqrt{\frac{1}{N} \sum_{\vec{x} \in J_i, J_{i-1}} \left(\frac{\partial}{\partial t} J_i(\vec{x}) \right)^2}. \quad (2.3)$$

DVARs measures the change in BOLD signal intensity, which is highly related to motion-induced spin gradient changes.

2.4.3 Acceptable Motion Quantities

Even though the effects of motion on the patient position and the recorded signal can be measured, we still need gold standard criteria to determine whether an image containing motion can be used. Patients move slightly due to breathing and cardiac function, and the BOLD signal naturally fluctuates over time. Some motion is expected; however, we need to know how much motion can be present in the image before it is considered to be corrupted by it. Power et al. established thresholds for FD and DVARS to determine the usability of a pair of images:

- FD less than or equal to 0.2 mm from previous volume, and

- DVARS less than or equal to 25 units on a normalized scale of [0, 1000] signal units (Power et al., 2014)

Image volumes that meet these criteria are considered to be low-motion.

The time span of low-motion data is highly debated. van Dijk et al. established that approximately five minutes of low-motion data is sufficient for use in functional connectivity analysis (van Dijk et al., 2012). However, a recent study by Laumann et al. suggests that at least 10 minutes of low-motion data is essential for obtaining high-quality results (Laumann et al., 2015). From a practical standpoint, it is difficult to obtain even five minutes of low motion data from certain patient populations, so radiology technicians and neuroimaging study designers are often content with the five minute time standard.

2.5 MOTION PREVENTION

During an MRI scan, thick foam pads of various sizes and shapes are used to isolate and immobilize the area of interest on the patient. While these pads impede most motion, especially in compliant patients, additional techniques and protocols are often used to prevent patients from moving during the image acquisition process. Not all of these techniques are suitable for all patient populations, and some techniques have been designed specifically for certain populations.

2.5.1 Pre-Scan: Education

Educational material can be used to help the patient understand what to expect during an MRI scan as well as to teach the patient different behavioral coping strategies. The education materials can be used either before or upon arrival at the imaging facility. Most of the formal literature focuses on informative, distraction, and behavioral techniques to use during pediatric MRI scans, though many of the following approaches could be adapted for use with adults.

In a review of the available literature, Alexander found several commonly used tech-

niques to educate pediatric patients before and comfort or distract pediatric patients during radiology procedures ([Alexander, 2012](#)). Tools such as educational coloring books and short videos can expose patients to the types of equipment they can expect to see using a familiar, engaging medium. Pediatric patients can learn coping strategies to employ during the scan such as breathing techniques, imagery, and positive statements. Alexander notes that allowing a pediatric patient to choose a behavioral coping strategy gives the patient a sense of control and may encourage the patient to cooperate during the MRI acquisition.

Mock scanners and MRI simulators can also help the patient feel more comfortable during the scan. Barnea-Goraly et al. showed that both a commercial MRI simulator and a low-tech mock scanner desensitized pediatric patients between four and ten years of age to the MRI scanner with the results that 92.3% of the acquired images could be used in high-resolution anatomical studies ([Barnea-Goraly et al., 2014](#)).

Several groups have investigated the role of auditory and visual distraction during an MRI acquisition. Headphones with music and stories or MR compatible video goggles can distract patients from the tedium of the scan ([Alexander, 2012](#)) ([Barnea-Goraly et al., 2014](#)) ([Harned and Strain, 2001](#)). Khan et al. found that a relatively simple moving light show can be helpful in distracting younger patients ([Khan et al., 2007](#)). Garcia-Palacios et al. performed a case study comparing the efficacy of music and immersive virtual reality tools as distractions during a mock scan ([Garcia-Palacios et al., 2007](#)). They suggest that immersive virtual reality may help decrease patient anxiety during a scan more effectively than music alone. As virtual reality technology improves, it may join headphones and MR compatible video goggles as an available distraction method.

Another helpful source of distraction for pediatric patients could be the patient's parent or parents. Having a parent involved with the scanning process may calm the patient and encourage him to cooperate; however, parental distress can further upset an anxious patient and complicate the scanning process ([Alexander, 2012](#)).

These techniques for educating the patient and helping the patient cope with the anxiety that can accompany an MRI scan all depend on the ability of the patient to understand instructions and communicate with the scan team. Due to the gap in communication abilities, these techniques are not useful for young patients such as neonates, infants, toddlers, and

possibly elementary school aged children. Other patient populations, such as those with developmental delays and neurobehavioral disorders, may also have difficulty adhering to these protocols. Even in patients with developed and intact communication skills, the techniques outlined here do not actively prevent the patient from moving during the scan: they only help the patient feel more comfortable with the MRI environment.

2.5.2 During Scan: Sedation

Sedation can be used to help a patient tolerate an MRI scan. Murphy and Brunberg retrospectively analyzed seven weeks of data from the MR department and found that 14.2% of their adult patients required some form of sedation ([Murphy and Brunberg, 1997](#)). In a study about claustrophobia and MR acquisitions, Dewey et al. report that out of 55,734 patients who underwent MRI scans, a total of 1004 patients experienced claustrophobia and 610 of these patients required intravenous sedation before their scans ([Dewey et al., 2007](#)). Even though sedation allowed the patients mentioned in this paragraph to undergo an MRI scan, the authors of both studies note that sedation can result in adverse events and advise the reader to avoid patient sedation if possible.

Sedation can be used with pediatric patients, though the risks are more significant than with adult patients. Studies have shown that sedation for pediatric imaging can lead to hypoxemia and inappropriate sedation levels during image acquisition ([Malviya et al., 2000](#)). Pediatric patients can also expect “motor imbalance and gastrointestinal effects,” as well as agitation and restlessness for a period of hours after waking from sedation.

A report from the American Academy of Pediatrics and the American Academy of Pediatric Dentistry outlines the minimum set of criteria needed for a pediatric patient to be sedated for a procedure ([Coté and Wilson, 2016](#)):

- The patient must be a suitable candidate for sedation based on their medical history and medical needs.
- The patient’s health status must be evaluated and verified by the sedation team prior to the procedure.
- Informed consent must be obtained prior to the procedure.

- Instructions for what to expect and how to transport the patient home safely must be provided to the patient’s responsible adult.
- At least one responsible adult must be with the patient at the medical facility, though the report recommends that two adults are present for patients who travel to and from the facility using car seats. This practice ensures that one adult can monitor the patient after the procedure while the other adult drives.
- The patient’s food and drink intake prior to the procedure should be taken into account to minimize the risk of pulmonary aspiration.
- The clinician administering the sedation must have immediate access to emergency facilities, personnel, and equipment, and should monitor the patient for adverse events including respiratory events, seizures, vomiting, and allergic reactions.
- There must be a clear protocol outlined for immediately accessing these emergency services.
- Emergency equipment and drugs appropriate for the patient’s size and age must be immediately available in case the patient needs to be resuscitated.
- The information about the procedure must be correctly documented.
- The facility should have a dedicated recovery area, and the status of the patient should be recorded when he is discharged. The patient should not be discharged if his level of consciousness and oxygen saturation do not meet recognized guidelines.
- The patient may be held at the facility for prolonged monitoring after the procedure.

This report clearly states that the levels of monitoring suggested above should serve as minimum levels of involvement: clinicians should increase patient monitoring as needed for complex cases. Rutman has a similar and detailed perspective on patient monitoring during and after sedation, adding that two independent medical personnel should be present during the scan and one should be present until the patient is discharged ([Rutman, 2009](#)). Rutman also notes that all sedation and monitoring equipment must be MR compatible, which is a simple but important safety constraint. This constraint makes sedation less advisable if the appropriate equipment is not available.

Sedation in neonatal and infant populations is not recommended. The U. S. Food and Drug Administration (FDA) issued a warning in late 2016 about repeated use of sedation or

general anesthesia for patients under three years of age or for pregnant women during their third trimester ([United States Food and Drug Administration, 2016](#)). The warning states that while a single, relatively short exposure to sedative and anesthetic drugs is unlikely to impact the patient, the effects of prolonged exposure to these drugs are still being studied. Studies of sedative and anesthetic drugs in multiple animal models have shown that these drugs can lead to loss of nerve cells in the brain when the animals undergo prolonged, repeated exposure to them during period of brain development. More data is needed to determine if this effect translates to humans.

2.5.3 During Scan: Feed and Sleep Protocols

Neither sedation nor educational and behavioral techniques are appropriate to use with neonatal patients, but rs-fMRIs in neonates and infants are invaluable in studying early brain development and neurological diseases ([Smyser and Neil, 2015](#)). A set of protocols have been developed specifically for scanning neonates without sedation. These protocols are referred to as “feed and sleep” or “feed and bundle” protocols.

Windram et al. describe a protocol in which the infant is deprived of food for four hours prior to the scan ([Windram et al., 2011](#)). At the scanning facility, the patient is fed by his mother, swaddled, and placed in a vacuum-bag immobilizer for the duration of the scan.

Rather than deprive the patient of food prior to the scan, Gale et al.’s protocol recommends timing the scan so that the patient is fed after arrival on site and less than 45 minutes before the scan ([Gale et al., 2013](#)). The patient’s ears are protected from the noise of the MR scanner by a layer of dental putty followed by headphones, and held in place by a hat. The patient is the swaddled and placed in the scanner once he is asleep. Additional foam padding is used to cushion the patient’s head and provides extra noise protection.

Mathur et al. describe a protocol similar to the previous two: the patient’s feeding schedule is adjusted so that he feeds 30-45 minutes before the scan time, and he is swaddled, given ear protection, and placed in a vacuum-bag immobilizer ([Mathur et al., 2008](#)).

When performed correctly, these protocols are generally successful and the neonatal patient will sleep for the duration of the MRI scan. However, the patient may shift slightly

while asleep or may wake up and move mid-scan.

2.6 PROSPECTIVE MOTION CORRECTION

Since motion cannot be completely eliminated from rs-fMRI scans, different approaches have developed for correcting for the effects of motion after the scan. These approaches can be divided into two groups: those which monitor the patient’s motion during the scan and those which work solely on the acquired sequences.

2.6.1 Optical Motion Correction

Several groups have developed methods for actively accounting for changes in the patient’s position during an MRI scan. Optical-based methods record the patient’s position using a combination of markers placed on the patient and one or more MR compatible optical cameras placed the scanner bore. The changes in the patient position from one time point to the next are used to update the MR parameters in real-time. Real-time updates of the MR parameters result in decreased spatial and spin-history effects of motion in the acquired sequences.

The first report of successful prospective motion correction using optical cameras and markers was by Zaitsev et al. in 2006 ([Zaitsev et al., 2006](#)). Their dual camera system was located outside of the MRI scanner and focused on the patient inside the system. Four reflective markers were attached to a modified mouthpiece originally designed for patient immobilization. Changes in the translation and rotation of the patient were recorded and processed during the exam. The processed changes were sent in real-time to the MRI scanner which used them to update the gradient orientations, RF frequencies, and RF phases at every time point during the acquisition process.

Aksoy et al. simplify this approach by using a single in-bore optical camera and replacing the 3D markers with a small 2D chessboard grid ([Aksoy et al., 2008](#)). Properties intrinsic to the camera as well as information about the camera’s placement within the MRI scanner were

recorded prior as part of a calibration process. During the scan, patient movements recorded using the optical camera were used to calculate the relationship between the patient’s position at the current time point in the physical space and the patient’s position at the initial time point in the MR space. The transformation needed to translate between these two positions was calculated on a laptop and passed to the MRI scanner to correct for motion in real-time. The camera used to record the position of the chessboard is mounted on the head coil. If the patient moves his head significantly, the camera will only be able to record the position of part of the chessboard marker. This limitation makes it difficult for the computer vision processing to identify the independent features on the standard chessboard.

Forman et al. modified the chessboard marker to improve its use for high-motion patients ([Forman et al., 2011](#)). To differentiate between the different blocks in the chessboard, they added a unique, machine readable symbol to each black block in the chessboard. The symbols were chosen to be unique even in the event of rotation so that the identification of each block would be robust to rotation movements. The chessboard marker was embedded with MR-detectable agar so that the position of the marker could be detected in the MRI scan as well as by the in-bore camera. At each point during the scan, the image recorded by the in-bore camera was sent to a computer independent from the MRI controller. The independent computer detected the blocks of the chessboard and identified their spatial locations using the symbols contained within them. Their positions were checked by confirming the locations of the symbols with respect to each other. The confirmed locations of the corners of the black boxes were used to estimate the position of the patient, which was then sent to the MRI controller so that the magnetic gradients and RF hardware could be updated for the time point. The authors note that the latency of the system is a significant limitation to their system, but overall they experienced an increase in the accuracy of the estimates of the patient’s position.

Several companies have developed commercial products for prospective motion correction in neurological images. KintetiCor’s system uses a high resolution camera and a physical marker to detect motion ([KintetiCor Biometric Intelligence, 2019](#)). The camera’s resolution allows it to detect respiratory and cardiac motion through changes in skin displacement on the patient’s forehead. The physical marker consists of pair of rectangles containing several

concentric circles which are connected via a bridge across the nose. Any patient movement is reflected in the movement of the markers, which is also tracked through the camera. Both the camera system and the marker are MR compatible. Another company, TracInnovations, uses a stereo camera system to track all patient motion ([TracInnovations, 2019](#)). At the start of the scan, the stereo camera obtains a point cloud of the patient’s position at that time. The points in the point cloud are averaged together to create a primary marker. Small facial motions, cardiac motion, and respiratory motion, are monitored using the point cloud. Larger head motions are monitored using both the point cloud and the primary marker. These two systems both allow prospective motion correction to be turned on or off: if the prospective motion correction is off, the system will still acquire the motion parameters so that the motion can be corrected retrospectively.

The methods and technologies discussed above have a few limitations due to the optical camera setups. For precise real-time motion correction, the camera or cameras must be carefully placed so that the position of the marker on the patient can be recorded. They must have a clear line of sight, which means they will be in the same room as the MRI scanner, if not within the scanner bore. The cameras and markers must be MR compatible, and the positions of the cameras and markers in physical space relative to the visual markers on the patient must be known. These positions are vital for the calculations used to measure the motions. Even if the motion measurements are accurate, the changes in position that are recorded and used to adapt the scan parameters will only be true for rigid body motion of the body part to which the markers are attached: any distortion of soft tissue will not be accurately accounted for during the motion correction unless the camera system was specifically built for and trained to do so.

Systems using markers attached to patient suffer from these limitations, but also from limitations due to the markers themselves. If the marker is not attached correctly to the patient, the marker can slip and move independently from the patient. The whole purpose of the markers are that they provide a known set of visual features that can be used to determine how a patient moved because they moved with the subject.

2.6.2 Non-Visual External Sensors

Cameras are not the only type of external sensor that can be used to measure motion during a rs-fMRI scan.

There is a class of sensors which can take advantage of electrophysics properties of an MRI scanner. These sensors include wired nuclear magnetic resonance field probes, wireless inductivity coupled markers, and off-resonance markers. The fact that these sensors directly interact with the magnetic field of the MR scanner means that protocols using these sensors must be modified to account for them. As a result of the protocol modification, the scan time might need to be extended.

As mentioned earlier in this chapter, respiration and cardiac activity are sources of patient motion. The most straightforward way to reduce the effect of respiratory motion is to instruct the patient to hold their breath at specific intervals during the scan. One alternative to breath holding uses the periodic nature of respiration. Since respiration is relatively periodic, it can be monitored and accounted for within a scan protocol via gating. A comparative study of breath holding and respiratory gating in MRIs of the coronary arteries suggests that images acquired using respiratory gating had 76% better quality than the images acquired using breath holding ([Hofman et al., 1995](#)).

In cases where only respiration is taken into account, gating prevents an image from being acquired unless the patient is in the specified state. In the case of respiration, the specified state is either complete inhalation or exhalation. The state of a patient's respiration can be tracked using respiration bellows. After acquiring the MRI sequence, volumes in the sequence can be grouped depending on when they were recorded in the breathing cycle. By only using volumes recorded during the same stage of the breathing cycle, the effects of respiratory motion can be mitigated. This approach to gating will increase the amount of scanner time needed.

When both cardiac and respiratory motion are considered, the patient's respiration is monitored through a bellows or pressure belt and their cardiac activity is monitored on a delay during the scan through a pulse oximeter on the patient's finger ([Hu et al., 1995](#)). The cardiac and respiratory data are synchronized with the acquired image after the scan.

The synchronized signals are then used to remove changes in the image associated with physiological motion, which “substantially reduces image-to-image fluctuations” (?).

For macro-scale motions, electromagnetically sensitive trackers can be placed on the patient and used to monitor changes in position during the scan. Afacan et al. used a tracker produced by Robin Medical Inc. (Baltimore, MD) to measure the position and orientation of subjects relative to the center of the scanner bore (Afacan et al., 2016). The tracker consisted of two sensors which were attached to the patient’s forehead. The sensors recorded their x , y , and z coordinates as well as two vectors indicating their orientations at every magnetic activation. These measurements were processed and displayed for a technician in real time during each scan.

Ultimately, using external sensors to monitor the patient for inherent physiological motion can improve the quality of the obtained MR images. However, the addition of extra sensors complicate the process and set up of a rs-fMRI scan.

2.6.3 Image Signal Motion Monitoring

Dosenbach et al. have developed a tool to evaluate motion in rs-fMRI sequences as they are acquired (Dosenbach et al., 2017). It registers each volume to the initial volume of the rs-fMRI sequence immediately after the new volume is recorded. The parameters produced by this registration are used to calculate the framewise displacement between pairs of volumes, which is then compared to a set of displacement thresholds associated with the scan quality. The number of volumes that meet each threshold is used to determine how many more volumes are needed to obtain five minutes of low-motion volumes. This method for assessing the quality of a scan in real time is useful for ensuring images are acquired with a sufficient number of low-motion volumes. It can also aid the technologists in determining whether to prematurely terminate a scan, which may be desirable if the amount of time needed to obtain enough low-motion volumes is greater than the amount of time remaining for the patient in the scanner.

2.6.4 General Limitations of Prospective Motion Correction

All types of prospective motion correction introduce a delay into the scanning process. The delay is due to the additional processing of some metrics to determine the patient’s position, the transmission of these metrics to the MR scanner, and the adjustments the scanner makes to its next set of measurements. These alterations to the image acquisition during prospective motion correction actively change the image as it is acquired. Maclaren et al. note that while prospective motion correction reduces inhomogeneities in the B_0 field, the B_0 field will still change when the patient moves and may change while the motion correction is occurring (Maclaren et al., 2013).

In order to view a scan not impacted by prospective motion correction, the patient often must undergo a second scan. It may be wise to build the second image acquisition into the same scan period as the prospectively motion corrected scan: unsuccessful prospective motion correction has the potential to drastically corrupt the acquired scan (Zaitsev et al., 2017).

Finally, though prospective motion correction has great power for managing motion during a scan, it cannot be used to recover motion-corrupted data in existing data sets.

2.7 RETROSPECTIVE MOTION CORRECTION

Many groups have put significant effort into developing techniques for motion correction after the scan is acquired. Here, we discuss several commonly used techniques: volume registration, denoising, and filtering.

2.7.1 Volume Registration

The rs-fMR image is stored in computer memory as a set of 3D matrices. The values in corresponding cells of each matrix are considered to be aligned in this digital space (voxel space). The voxel space is defined by the imaging protocol and relates to the physical space through the spatial resolution of the image. Even though the spatial and voxel spaces

for the image align, the contents of the image volumes may be misaligned due to patient movement. Because we cannot assume that an image is completely motion-free, we cannot directly compare the contents of each image volume in the rs-fMRI sequence. However, we can use image registration to align the contents of the image volumes to reduce the impact of motion on patient position.

Image registration is the process of morphing the contents of one image so that they overlap optimally with another image. The morphing operations include translation, rotation, scaling, skewing, and nonlinear adjustments. The linear and affine operations in this list should be used to perform rigid body registrations for organs such as the brain. Nonlinear operations can be used to fine-tune the alignment of more pliable organs such as the liver. All morphing operations are applied to one image repeatedly until it’s contents optimally match those of the static reference image as determined by a chosen similarity metric.

One of the earliest examples of image registration was described by Friston et al. in 1995 (Friston et al., 1995). They performed image registration on positron emission tomography (PET) scans and MRI scans of a human brain. During the registration process, one scan was designated as the “reference” image, which remained stationary, and the other scan was designated as the “object” image, which was transformed to match the reference image. Constraining the alignment process to transforming a single image into the coordinates of the other image rather than transforming both images into an independent coordinate frame simplifies the registration process.

When performing image registration on a sequence of image volumes, one volume must be chosen as the reference volume for the entire sequence. All other volumes in the sequence are registered to this volume. An example of this process can be seen in Figure 3. In subsequent work, Friston et al. used the first volume in the rs-fMRI sequence as the universal reference image (Friston et al., 1996). Common choices for the reference volume include the volume with the least positional difference to all other volumes in the sequence, a volume produced by averaging all volumes in the sequence, or the first volume in the sequence (Friston et al., 1996) (Liao et al., 2005). In our implementation, we chose to use the first volume in the sequence as the reference volume.

One drawback to this traditional approach to volume registration is that it only minimizes

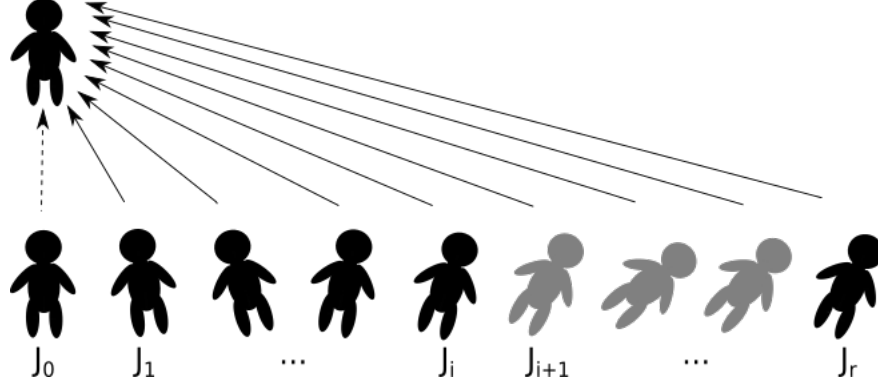


Figure 3: The traditional approach to volume registration in an rs-fMRI sequence consists of registering all volumes in the sequence to a single reference volume.

the differences between all the image volumes in the sequence and the reference volume. The key word here is minimizes: minimizing differences between image volumes does not mean that there are no differences between the image volumes. Image registration is an optimization problem, and its goal is to find the overlap between a pair of volumes with as few differences as possible either within a defined time period or until the optimization cost does not change above a certain tolerance for a certain amount of time. These practical constraints on optimization problems mean that there may still be differences between other pairs of image volumes in the sequence that do not include the reference volume.

Variations on Friston et al.'s framework have been developed over the last two decades. Liao et al. suggested that a rs-fMRI sequence could be viewed as a hidden Markov model, and reflected this idea in their suggested registration framework (Liao et al., 2016). They still use the first volume in the image sequence as the reference volume. Their framework uses the transformation of the previous volume to the reference volume to initialize the transformation for the current volume and the reference volume.

It has been demonstrated that image registration across the entire image sequence reduces the effects of motion on the image sequence, though they do note that motion also effects the image due to changes in the spin history of the image. These effects are not correctable by global volume registration alone and will be discussed later in this chapter.

2.7.2 Denoising

Denoising techniques can be applied to a rs-fMRI after global volume registration is completed. They consist of regressions of various confound variables.

It is relatively common for researchers to use rigid realignment parameters calculated during volume registration as signals to remove vari regression. The realignment parameters are the translations along and the rotations about the x , y , and z axes (Power et al., 2012). These six parameters and their first order derivatives are suggested as regression parameters by several researchers (Power et al., 2012) (Satterthwaite et al., 2012) (van Dijk et al., 2012).

While the realignment parameters and their derivative for the current image volumes helps reduce the effects of motion on an image sequence, these parameters are not sufficient on their own. As the effects of motion on rs-fMRIs have been studied, it has been established that motion at one point in the sequence can affect the next several volumes. Researchers have decided to address this effect by incorporating the rigid realignment parameters from surrounding timepoints into the regression parameters for any given current image volume (Power et al., 2014) (Satterthwaite et al., 2013) (Yan et al., 2013b).

Patriat et al. performed a robust comparison of different regression parameters on their MotSim motion data set (Patriat et al., 2017). They included rigid realignment parameters, but also used parameters obtained by performing principle component analysis (PCA) on the image sequences. PCA generates a set of linear, uncorrelated components that reflect the main features of a patient’s motion. The list of parameter combinations included

- 12mot: The six rigid realignment parameters and their first derivatives,
- 12for: The first 12 principal components of the whole brain before realignment,
- 12back: The first 12 principal components of the whole brain after realignment,
- 12both: The first 12 principal components of the whole brain both before and after realignment,
- 24mot: the six rigid realignment parameters of the current volume, the six rigid realignment parameters of the previous volume, and the square of these rigid realignment parameters,
- 24both: the first 24 principle components of the whole brain before and after realignment.

They found that the features extracted from the image sequence using PCA explained more variance in the image sequence (measured using R^2) than the rigid realignment parameters. They showed that increasing the number of regressors increased the amount of variance explained, but with diminishing returns. While their work is promising, their experiment was performed on a simulated data set using healthy subject data and required an accurate estimate of the subject’s head motion.

In addition to the positional effects of motion, the spin history and susceptibility effects of motion must be considered. Signals associated with these effects are called nuisance signals. One common nuisance signal is the global signal of the image sequence. Global signal regression (GSR) corrects for variance between temporal signals within a voxel and for the mean BOLD signal across all voxels (Power et al., 2014) (Satterthwaite et al., 2013) (Yan et al., 2013a) (Yan et al., 2013b). GSR has been shown to reduce spuriously increased long-distance correlations in functional connectivity studies, but may inadvertently weaken shorter-distance connections (Jo et al., 2013) (Power et al., 2014) (Satterthwaite et al., 2012). Other nuisance signals that can be removed via regression are signals white matter and cerebral spinal fluid (CSF) (Power et al., 2014) (Satterthwaite et al., 2013). The impact of removing these signals from the image sequence has been shown to be limited: in some cases, removing white matter and CSF signals does not reduce the effects of motion on the BOLD signal (Yan et al., 2013b) (Jo et al., 2010).

A third set of signals that may be removed via regression are components identified using techniques such as principal component analysis (PCA) or independent component analysis (ICA) (Pruim et al., 2015) (Salimi-Khorshidi et al., 2014) (Behzadi et al., 2007). Though both PCA and ICA decompose a set of data into a list of signals, the properties of the lists are different. PCA produces a list of orthogonal signals that best represent the features of a data set ordered from most representative to least representative. The list of components produced by ICA are assumed to be independent (not just uncorrelated) and combine additively to produce the original signal. Regression of each of these sets of signals has been shown to reduce the effects of motion in the sequence but neither removes them entirely (Power et al., 2015) (Parkes et al., 2017).

2.7.3 Filtering

Not all patients move in the same ways or at the same rate. In some cases, a patient will perform a large and sudden movement and then settle into a position close to their original position. The volumes containing the motion can be removed from the rs-fMRI sequence to create smaller, motion-free sequences. Several studies have found that subsequences of data of the same patient can be concatenated to produce a longer sequence without impacting the functional connectivity analysis. The process of detecting and removing motion-corrupted volumes has been formalized into several filtering techniques. Three popular filtering techniques are scrubbing, spike regression, and despiking.

Scrubbing begins by examining the image sequence for “high-motion” image volumes (Power et al., 2012). Here, “high-motion” is defined as image volumes which have 0.5 mm FD and 0.5% DVARS difference from their preceeding volume. Volumes containing at least this quantity of motion as well as the preceeding volume and two subsequent volumes are removed from the sequence, resulting in a set of discontinuous subsequences. The discontinuous subsequences can be combined without negatively impacting the functional connectivity analysis of the BOLD signal (Fair et al., 2007) (van Dijk et al., 2010). As long as the reconnected subsequences compose a sequence at least 125 frames (approximately 5 minutes) in length, the scrubbed sequence can be used for analysis (Power et al., 2012). Many techniques for temporally filtering high-motion rs-fMRIs have been developed, though all of them result in the loss of image volumes (Barnes et al., 2011) (Fransson et al., 2007) (Jones et al., 2010) (Kennedy and Courchesne, 2008) (Smyser et al., 2010) (Smyser et al., 2011).

Spike regression also identifies volumes containing large quantities of motion, though it treats them differently than scrubbing does. (Satterthwaite et al., 2013). It identifies spikes in the image sequence and replaces frames effected by the spikes with interpolated volumes.

A spike is defined as a frame in the sequence where the FD or the FD and the DVARS between it and its previous frame surpass a given set of thresholds. The value of the thresholds greatly impacts the cleaned image sequence. A low threshold will identify more spikes and produce a cleaner image sequence but remove more data, while a high threshold will

retain more data but contain more motion artifacts. The thresholds used by Satterthwaite et al. on their adolescent data set are .25 mm FD and 1.4% units DVARs.

After identifying the spikes in an image sequence, they are modeled as signals to remove through regression. The simplest model of a spike is as a motion event at a single time point. However, it has been established that patient motion may effect several frames in the image sequence. Satterthwaite et al. examined six combinations of frames around the frame in which the spike was based during their analysis of spike regression. They found that removing spikes identified using just the FD threshold and modeled as only effecting a single frame resulted in the fewest different neural connections in the highest and lowest motion images as well as the lowest correlation between functional connectivity and patient motion (Satterthwaite et al., 2013).

Despiking is different from these techniques. It treats the image sequence as a single image volume where each voxel contains an intensity signal. Each intensity signal is examined for sudden changes, or spikes. The value of each detected spike is replaced with an interpolated value calculated using the preceeding and subsequent points in the voxel's signal (Jo et al., 2013) (Patel et al., 2014). Despiking does not remove volumes, but could accidentally remove valuable signals if they appear as outliers in the image voxel signals.

2.7.4 Spin History Distortion Correction

A number of post-acquisition methods have been developed specifically to correct for distortions due to the impact of motion on the magnetic field. The usability of these dynamic distortion correction methods has been studied in a few specific cases, but their generalizability has yet to be confirmed in a broader range of fMRI studies (Zaitsev et al., 2017).

2.8 SUMMARY

Resting-state fMRIs are four dimensional images which record BOLD signal in active areas of the brain. The BOLD signal can be used to evaluate the functional connectivity of

different underlying networks in a patient's brain. Since rs-fMRIs are highly sensitive to motion, clinicians and psychologists have devised techniques to inform patients about what they can expect during an MRI scan as well as different coping mechanisms to help them remain calm during the scan. These techniques do not prevent the patient from moving, but approaches that do are not always appropriate to use during a rs-fMRI scan. Techniques and algorithms to prospectively and retrospectively remove motion from rs-fMRIs have also been developed, though they are not always successful in removing the effects of motion. Ultimately, the amount of motion present in the rs-fMRI sequence dictates whether or not the sequence can be used in clinical or research applications.

In the next chapter, we will discuss rs-fMRIs in the context of our chosen population of CHD patients.

3.0 METHODS: MOTION CORRECTION

In the previous chapter, we discuss several techniques used to retrospectively correct motion. Motion correction pipelines may use denoising and filtering, but all pipelines begin with volume registration. In this chapter, we discuss a different approach to volume registration, how it compares to traditional volume registration, and how volume registration fits into a motion correction pipeline.

3.1 DIRECTED ACYCLIC GRAPH BASED VOLUME REGISTRATION

As discussed previously, the major drawback to Friston et al.’s approach to volume registration is that it only minimized the positional differences between the reference volume and the rest of the sequence. This drawback demonstrates an inability for the traditional approach to account for relationships in the patient’s position throughout the scan. Intuitively, we know that the patient’s position at any volume in the scan is more similar to his position in the immediately previous or subsequent volume than to another randomly chosen volume in the image.

In our proposed framework, we wish to account for these spatiotemporal relationships between temporally neighboring volumes in the sequence. To accomplish this goal, we start by viewing the rs-fMRI sequence as a directed acyclic graph (DAG). A DAG consists of a set of nodes and edges. Each edge has a direction associated with it and connects a pair of nodes. Since a DAG contains no cycles, there is no possible path back to a node once it has been traversed.

In the case of an rs-fMRI, each volume can be considered a node. The relationship

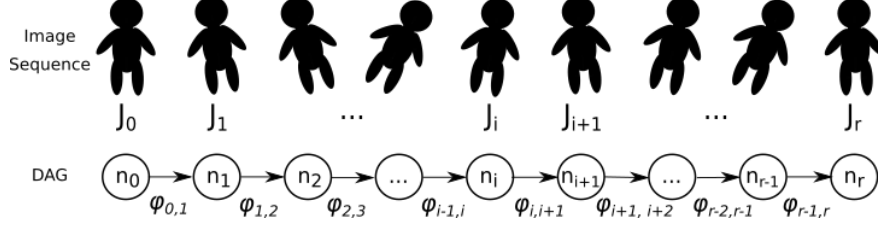


Figure 4: A rs-fMRI can be viewed as a directed acyclic graph where each volume is a node and the edges connect from each volume i to the following volume $i + 1$.

between each pair of temporally neighboring volumes is represented as a directed edge connecting the node for the first volume to the node for the next volume. The acyclic nature of the DAG means that once a patient was in a specific position, he will never return to that exact same position with the exact same neurons firing. The position of the subject and his brain activity as measured by the BOLD signal may be similar in subsequent image volumes, but it will never be precisely the same. The perspectives of an rs-fMRI sequence as a set of images and of the sequence as a DAG can be seen in Figure 4.

The cost of transitioning from one node to the next in our DAG has a parallel representation to the combination of the positional transformation needed to align volume i to volume $i + 1$ and the signal change between the volumes. This representation can be written as

$$J_{i+1} = \phi_{i,i+1} J_i + \delta s_{i,i+1} + \epsilon \quad (3.1)$$

where J_i and J_{i+1} are volumes i and $i + 1$, $\phi_{i,i+1}$ is a matrix of transformation parameters that must be applied to J_i to achieve the patients position in J_{i+1} , $\delta s_{i,i+1}$ is the natural change in BOLD signal, and ϵ is the change in BOLD signal due to motion. Currently, there is no way to estimate the natural change in BOLD signal and the change in BOLD signal due to motion without incorporating additional information about the MRI scanner and the patient that is not included in a rs-fMRI. We simplify our representation of the relationship

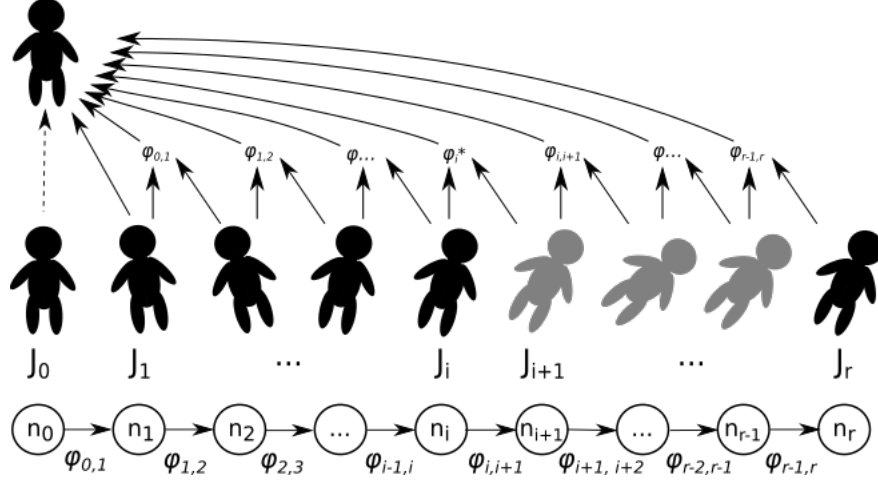


Figure 5: The traditional approach to volume registration in an rs-fMRI sequence consists of registering all volumes in the sequence to a single reference volume.

between two volumes to

$$J_{i+1} = \phi_{i,i+1} J_i + \epsilon^* \quad (3.2)$$

where ϵ^* is the change in the BOLD signal that cannot be accounted for after aligning the patients position in the two volumes. Here, we use the notation ϵ^* to represent the generic error change in BOLD signal across any pair of volumes.

After aligning two volumes i and $i + 1$, we will then align volumes $i + 1$ and $i + 2$:

$$\begin{aligned} J_{i+2} &= \phi_{i+1,i+2} J_{i+1} + \epsilon^* \\ &= \phi_{i+1,i+2} (\phi_{i,i+1} J_i + \epsilon^*) + \epsilon^* \\ &= \phi_{i+1,i+2} \phi_{i,i+1} J_i + \epsilon^{*'} \end{aligned} \quad (3.3)$$

Traditional volume registration assumes that

$$\phi_{i,i+2} = \phi_{i+1,i+2} \phi_{i,i+1} \quad (3.4)$$

and calculates $\phi_{i,i+2}$ directly. We argue that this assumption is not true in all cases. Rather than directly calculate $\phi_{0,i}$ and use it to align volume i to the reference volume as the traditional method does, we calculate each component ϕ that is a factor of $\phi_{0,i}$. Each component $\phi_{i,i+1}$ is combined with the preceding $\phi_{0,i}$ s to recursively align volume $i+1$ to the reference volume without making the large and often inaccurate transformations required by directly calculating $\phi_{0,i+1}$. This process is outlined in Figure 5.

3.2 INDEPENDENT COMPONENT ANALYSIS

The purpose of image registration is purely to ensure the position of the patient throughout the entire rs-fMRI is consistent. After registration, the image still contains BOLD source signals and noise signals caused by factors other than brain activity. The challenge of separating these combined signals is called blind source separation (BSS).

We chose to focus on an independent component analysis (ICA) approach for solving the BSS problem. The specific technique we use has been described by Beckmann and Smith as probabilistic ICA. This section aims to provide an overview of the probabilistic ICA technique. For further details, please refer to the technical reports by the FMRIB group ([Beckmann and Smith, 2004](#)) ([Woolrich et al., 2004](#)) ([Beckmann et al., 2003](#)) ([Smith et al., 2004](#)).

Probabilistic ICA is a linear regression model which performs mixing in the original data space and assumes the true BOLD signal has been confounded by Gaussian noise. These constraints mean that BSS can be solved in three steps:

1. Estimate a joint subspace consisting of source and noise signals and a noise subspace orthogonal to the joint subspace,
2. Estimate the independent sources in the joint subspace, and
3. Assess the statistical significance of the independent sources.

Probabilistic ICA treats the voxel intensity values in every frame of the image sequence as a matrix of V voxels across n time points. For each voxel $v_i \in V$, the observed signal in

that voxel can be modeled as

$$\vec{x}_i = A\vec{s}_i + \mu + \vec{\eta}_i \quad (3.5)$$

This equation allows three different types of signals to contribute to the observed voxel values \vec{x}_i for a given voxel across all n timepoints in the sequence. The first type of signal is a vector of non-Gaussian source signals \vec{s}_i across all n timepoints. The source signals are modulated by mixing matrix A whose shape is the number of time points n by the number of source signals q . The second type of signal is an offset denoted by μ . The offset constrains the observed signals to be centered around the mean of all observed signals. The third type of signal $\vec{\eta}_i$ is a vector of noise throughout the duration of the sequence. To summarize, probabilistic ICA explicitly assumes that the observed signal in a given voxel can be divided into non-Gaussian source signals, isotropic Gaussian noise signals, and some offset. This assumption makes it easier to separate a source signal from a noise signal: a noise signal will have a Gaussian distribution while a source signal will not. **The goal of probabilistic ICA is to identify the source signals, \vec{s} .**

With this combination of signals in mind, we can write the covariance matrix of the observed data x as

$$R_x = \langle x_i x_i^T \rangle = AA^T + \sigma^2 I \quad (3.6)$$

where A is the mixing matrix, σ^2 is the standard deviation of the noise, and I is $n \times n$ identity matrix. The covariance matrix of the observed data R_x can be calculated, but A and σ^2 are both unknown. The noisy observed data is transformed with respect to the noise sources using a process called whitening. The whitening with respect to noise enforces the assumption of noise following an isotropic Gaussian distribution with a mean of zero and a standard deviation of σ^2 .

The mixing matrix A can be estimated using maximum likelihood estimation. Beckmann and Smith use singular value decomposition of the observed data $X = U(N\Lambda)^{\frac{1}{2}}V$ to model the estimator of A :

$$\hat{A}_{ML} = U_q(\Lambda_q - \sigma^2 I_q)^{\frac{1}{2}} Q^T \quad (3.7)$$

where U_q contains the eigenvectors associated with the q largest eigenvalues, Λ_q contains the q largest eigenvalues, and Q is a qxq orthogonal rotation matrix in the whitened observation space such that $QQ^T = I$. The eigenvectors and eigenvalues can be calculated from X , but σ and Q remain unknown. As noted earlier, the matrix Q is an orthogonal rotation matrix which, when applied to the whitened data \tilde{x} , has the same effect of applying an unmixing matrix to the observed data:

$$W\vec{x} = Q\tilde{x} = \hat{s} \quad (3.8)$$

Both matrix-vector multiplications serve to estimate individual source signals \hat{s} . The estimated source signals are identified by projecting the whited data \tilde{x} onto each row r of the unmixing matrix Q a total of q times:

$$\hat{s}_r = Q_{r,:}\tilde{x} \quad (3.9)$$

where the $Q_{r,:}$ represents row r of matrix Q . (*Note: A key assumption in this step is that the rows of the unmixing matrix are mutually orthogonal so that they cover the entire space of signal sources. Additional steps described by Beckmann and Smith can be taken to incorporate prior information about the voxels into this step (Beckmann and Smith, 2004).*)

At this point, the standard deviation of the noise σ^2 and the source signals are unknown. We can solve the following system of equations jointly to resolve these two unknown quantities:

$$\hat{s}_{ML} = (\hat{A}^T \hat{A})^{-1} \hat{A}^T x = \hat{W}x = Q\tilde{x} \quad (3.10)$$

$$\hat{\sigma}_{ML}^2 = \frac{1}{n-q} \sum_{l=q+1}^p \lambda_l. \quad (3.11)$$

Solving these equations is an iterative process. First, the mixing matrix and source signals are estimated. These estimations are used to calculate the corresponding estimator of the standard deviation of the noise. Then, the residual noise $\hat{\eta}_i$ at each voxel v_i is calculated:

$$\hat{\eta}_i = (I - \hat{W}^T \hat{W})x_i. \quad (3.12)$$

Recalling from Equation 3.5 how probabilistic ICA views a signal, Equation 3.12 becomes:

$$\hat{\eta}_i = (I - \hat{W}^T \hat{W})A + (I - \hat{W}^T \hat{W})\eta \quad (3.13)$$

When the correct number of sources has been identified, the estimated mixing matrix will fully span the source signal space. Then, the residual noise will only be related to the true noise:

$$\hat{\eta}_i = 0 + (I - \hat{W}^T \hat{W})\eta \quad (3.14)$$

Upon reaching this stage in the probabilistic ICA technique, the source signals have been approximated. The source signals are called spatial independent component maps. Normalizing the values in these maps by the variance of the noise produces Z -statistic maps. Z -statistic maps can be analyzed to identify voxels with statistically significant activations. These activations are attributed to BOLD signal.

One of the major limitations of ICA is that it is highly data driven. It assumes the dataset contains a sufficiently large number of images, each with a sufficiently large number of voxels. Even assuming an ideal data set, the true value of the mixing matrix is dependent on the observed data (Beckmann and Smith, 2004). Fluctuations in the data can lead to deviations of the residual noise in certain voxels from the true noise. These deviations can produce *type-I* and *type-II* errors when examining the Z -statistic maps to identify statistically significantly activated voxels.

Additionally, the developers of probabilistic ICA note that not all noise follows the isotropic Gaussian assumption. Noise based in the patient's physiology is likely to be structured in a way that is non-Gaussian. The non-Gaussian noise signals can still be separated from the BOLD source signals, but only if these noise signals are not highly correlated with the source signals.

3.3 MOTION CORRECTION PIPELINE AND IMPLEMENTATION

Both the traditional and novel volume registration techniques were applied independently to each image from the subject cohorts described in Chapter 5. After registration, three versions of each image existed: the original BOLD sequence, the sequence modified using traditional volume registration, and the sequence modified using the novel registration method.

The registration algorithms applied to rigid tissue types used affine registration with two degrees of granularity. When applied to soft tissue types (ie, placenta), three nonlinear transformations with increasing granularities were performed after the affine registrations. The exact parameters used for each volume registration can be seen in Appendix AA. The registration frameworks were implemented in Python using the nipy (Neuroimaging in Python Pipelines and Interfaces) library (Gorgolewski et al., 2011). Volume registration used the ANTs (Advanced Normalization Tools) tools as a backend (Avants et al., 2014).

After performing volume registration to ensure the patient is in the same physical space throughout the image sequence, the image sequence may still contain artifacts due to motion. Our registered sequences underwent motion correction via a well-established motion correction pipeline. We chose to use the independent component analysis (ICA) pipeline outlined by Beckmann and Smith (Beckmann and Smith, 2004). The motion corrected sequences produced by FMRIB’s MELODIC tool were saved alongside the original and registered sequences.

3.4 EVALUATING REGISTERED AND MOTION CORRECTED SEQUENCES AGAINST GOLD STANDARD USABILITY THRESHOLDS

The main goal of motion correction is to reduce the effects of motion on the image so that it is usable. The gold standards for rs-fMRI usability as established by Power et al. are that the FD and DVARS metrics must change less than 0.2 mm and 2.5% normalized voxel units between at least 50% of the neighboring volumes. The FD and DVARS metrics

between each pair of subsequent image volumes were calculated for the original, registered, and motion corrected sequences. The metrics for each sequence were then compared to the gold standard image usability thresholds. This comparison answers the key question of how each registration framework impacts an established motion correction pipeline.

Additionally, a smaller comparison of the registered sequences was conducted. This comparison evaluates the immediate impact of the registration algorithm on the image sequence. It is highly unlikely that an entire image sequence would meet the Power et al. usability thresholds after only the initial step of a motion correction pipeline, but it is valuable to examine the impact of a volume registration algorithm at each stage of the pipeline.

Implementation. We calculated the FD and DVARS metrics defined by Power et al. using the FSLMotionOutliers tool ([Power et al., 2012](#)).

4.0 METHODS: EVALUATING MOTION PATTERNS

In the previous chapter, we describe the methods we use to mitigate the positional effects of motion in rs-fMRI sequences. We briefly discuss how the motion corrected sequences were evaluated with respect to gold standard usability criteria. Here, we expand on our analysis of the motion extracted from the sequences.

4.1 MEASURING MOTION PATTERNS

While the Power et al. usability thresholds for the FD and DVARs metrics quantify the volume-to-volume motion well, they do not quantify the overall motion contained in the image sequence. The FD and DVARs metrics as well as other imaging metrics can be used to compare every volume in an image sequence to every other volume in the image sequence to better quantify whole-sequence motion. As the FD and DVARs metrics have been discussed previously, we will focus in this section on three other image metrics: the Dice coefficient, the correlation ratio, and the mutual information. These five metrics were applied to each whole sequence to measure patient motion and image signal consistency throughout the entire scan.

4.1.1 Dice Coefficient

The Dice coefficient was proposed by Lee R. Dice in 1945 (Dice, 1945). Dice examined several existing metrics for measuring association, and finding them lacking, proposed his own “coincidence index”. His coincidence index measures the association between a number

of samples a where condition A is true and a number of samples b where condition B is true:

$$Index = \frac{2h}{a + b} \quad (4.1)$$

In this equation, h represents the number of samples where both conditions A and B are true. His index can take on any value between 1.0 and 0.0 such that a value of 1.0 means that conditions A and B are true for all samples. Similarly, a value of 0.0 means that conditions A and B are never both true for any sample. While this index is a count of samples that meant both conditions and not a true probability, Dice suggests that the chi-squared test can be used to determine if the combinations of conditions in the samples from a set of data is meaningful or due to random chance.

Many medical imaging researchers have adapted the Dice coefficient to measure the overlap between pairs of images. Zijdenbos et al. trained an artificial neural network to semiautomatically segment brain MRIs and compared the generated segmentations to manual segmentations using the Dice coefficient (Zijdenbos et al., 1994). Zou et al. used the Dice similarity coefficient in their analysis of the reproducibility of manually segmented MRIs and the accuracy of automatic segmentations of the same images for prostate and brain tumor datasets (Zou et al., 2004). Liao et al. used it to measure the accuracy of a volume registration framework for aligning manual segmentations of multiple organs in fetal images (Liao et al., 2016). Bharatha et al. performed a study on pre- and intra-operative images of the prostate. They segmented the images, generated deformable finite element models of the segmentations, and used the Dice coefficient to compare the registered segmentations and finite element models (Bharatha et al., 2001).

It should be noted that the Dice coefficient as used in these contexts is a measure of similarity of items from two categories where each item belongs to exactly one class. The two classes of interest in the case of rs-fMRIs are “brain” or “not brain”. Medical images do not naturally have binary values. All studies mentioned in the previous paragraph require a domain expert to manually segment each image that will be analyzed using the Dice coefficient. The manually segmented images are considered the gold standard to which automatic segmentations or registered images can be compared.

The images in our dataset have been manually curated to remove the skull and other

anatomical features outside of it, but the images still contain a continuous range of voxel intensity values. The Dice coefficient cannot be directly applied to these image sequences, even though each voxel only belongs to one of two classes. The volumes first must undergo thresholding to create binary images to clearly separate brain and background for computational purposes. We use Otsu thresholding to accomplish this task.

Otsu thresholding divides the contents of an image into two binary classes based on the histogram of voxel intensity values. It assumes that the classes are represented in the histogram by separable peaks. It separates the peaks by finding the separation threshold with the best separation between classes. In its original form, Otsu thresholding exhaustively searches the space of all possible thresholds and calculates the within-class variance and between-class variance for the pair of classes separated by the current threshold option. The ideal threshold is the one which produces the minimal within-class variance and the maximal between-class variance. The ideal threshold is then used to convert the original image into a binary image volume where background voxels have a value of zero and voxels in the brain have a value of one. The binarized image volume can be compared to other binarized image volumes using the Dice coefficient.

In cases where a good Otsu thresholded binary image cannot be obtained, other similarity metrics such as mutual information and cross correlation should be used instead.

4.1.2 Correlation Ratio Matrix

The correlation ratio is an asymmetrical, spatially informed measure of the overlap between images. It is different from other similarity metrics in that a lower correlation ratio indicates a better alignment between two images rather than a worse alignment.

The earliest symbolic representation of the correlation ratio is

$$\eta = \frac{\Sigma}{\sigma_y} = \frac{\sqrt{\frac{\sum (n_x(\bar{y}_x - \bar{y})^2)}{N}}}{\sigma_y} \quad (4.2)$$

where n_x is the number of samples in any one set x , \bar{y}_x is the average of the samples in x , \bar{y} is the average of all samples in all sets, σ_y is the standard deviation of all samples in all sets, and N is the total number of samples across all sets (Rugg, 1917). The meaning of

this equation was simplified by Ayres, who describes it as “the ratio between two standard deviations” (Ayres, 1920). In Equation 4.2, the numerator is the standard deviation of a single set of samples with respect to all sets of samples, and the denominator is the standard deviation of all sets of samples. The process of calculating the individual components of this equation are outlined in (Rugg, 1917).

The correlation ratio was proposed for use in medical imaging applications in 1998 and compared to other similarity metrics. Roche et al. provide an example of aligning two black images, one with a uniform gray stripe and the other with a horizontal gray gradient, such that the overlap between the two images is maximally similar (Roche et al., 1998a), (Roche et al., 1998b). They show that the mutual information metric has a maximum value at every translation of an integer number of pixels while the correlation ratio had a maximum value at one single alignment. They apply the correlation ratio to MR images as well as computed tomography and positron emission tomography images. Their experiments suggest that in the context of multimodal registration, the correlation ratio balances accuracy and robustness.

In the context of medical imaging, the correlation ratio measures the functional dependence between a pair of images X and Y . The correlation ratio of Y given X is

$$\eta(Y|X) = \frac{Var[E(Y|X)]}{Var(Y)} \quad (4.3)$$

This equation is comparing the energy of Y in X to the total energy of Y . If X and Y overlap in area Ω , the number of pixels in that area is $N = Card(\Omega)$. Since X is known, it can be divided into sets of pixels Ω_i where each set is comprised of locations in Ω where the pixels X have the same value i .

Because the correlation ratio is a strong metric for measuring the similarity between two images, we suggest using it to quantify the similarity between all volumes in an image sequence. We choose to refer to this metric as the correlation ratio matrix. For a sequence of length l , the correlation ratio matrix M is a square, asymmetrical matrix of size $l * l$. Each

cell in M is calculated as

$$M_{i,j} = \eta(J_i, J_j) = \frac{\text{Var}[E(J_i|J_j)]}{\text{Var}(J_i)} = \frac{\sqrt{\frac{\sum |J_i|(\bar{J}_i - \bar{J}_i \cap \bar{J}_j)^2}{|J_i \cap J_j|}}}{\sigma_{J_i \cap J_j}} \quad (4.4)$$

where J_i and J_j are volumes $i \in l$ and $j \in l$ in the sequence, respectively. The sequence $J_i \cap J_j$ is the volume of space where images J_i and J_j intersect. The equation measures two different properties of the volume spaces J_i , J_j , and $J_i \cap J_j$: the number of voxels and the average of the voxel values in the space. The symbol $|\cdot|$ indicates the number of voxels the specified space, and the symbol $\bar{\cdot}$ indicates the average of the voxel values in the specified space.

Since the matrix M is quite large, using statistics describing M rather than M itself can simplify analyses. On the other hand, the whole matrix M can be more comprehensively analyzed using statistical tests such as the t -test.

4.1.3 Mutual Information

The earliest description of mutual information was written in the context of mathematical theories behind networked communication (Shannon, 1948). Mutual information is a measure of the amount of information shared between two signals X and Y . Specifically, mutual information measures how the joint distribution of the two signals compares to the marginal distribution of each signal (Li, 1990). It is a more general measure of dependence than correlation, which is limited to measuring linear dependence via a comparison of the marginal distributions. In terms of information theory, mutual information is represented as

$$MI(X, Y) = H(X) + H(Y) - H(XY) \quad (4.5)$$

where $H(X)$ is the entropy of signal X

$$H(X) = - \sum_{x \in X} p_x \log(p_x) \quad (4.6)$$

where p_x is the marginal distribution of the signal X . Substituting y for x in this equation produces $H(Y)$, the marginal entropy of the signal Y . Similarly, $H(XY)$ is the joint entropy

of signals X and Y given the known signals X and Y

$$H(XY) = - \sum_{x \in X, y \in Y} p_{xy} \log(p_{xy}). \quad (4.7)$$

It is worth noting that since the two signals of interest are registered images, x and y refer to voxel locations in the same image space. Substituting Equations 4.6 and 4.7 in Equation 4.5 produces the following

$$\begin{aligned} MI(X, Y) &= - \sum_{x \in X} p_x \log(p_x) - \sum_{y \in Y} p_y \log(p_y) + \sum_{x \in X, y \in Y} p_{xy} \log(p_{xy}) \\ &= \sum_{x \in X, y \in Y} p_{xy} \log p_{xy} - \left(\sum_{x \in X} p_x \log(p_x) + \sum_{y \in Y} p_y \log(p_y) \right) \end{aligned} \quad (4.8)$$

In the case where signals X and Y are independent, Equation 4.8 can be simplified to

$$\begin{aligned} MI(X, Y) &= \sum_{x \in X, y \in Y} p_{xy} \log(p_{xy}) - \left(\sum_{x \in X} \sum_{y \in Y} p_{xy} \log(p_x p_y) \right) \\ &= \sum_{x \in X, y \in Y} p_{xy} \log \left(\frac{p_{xy}}{p_x p_y} \right) \end{aligned} \quad (4.9)$$

Mutual information can be used to determine how the distribution of amplitudes in one signal relates to the distribution of another signal. It is commonly used in the medical imaging domain to objectively compare images of the same tissue taken using different modalities. For example, a computed tomography (CT) scan of a patient's abdomen contains different information about each tissue types' material properties than an MRI of the same organs. Some tissue types may appear similar in one of these modalities but drastically different in the other. Combining the information about a tissue's material properties gained from both imaging modalities provides more information than could be gained from either modality independently. (In other words, the resulting information is greater than the sum of its parts.)

Even though the rs-fMRIs in our study are all obtained using the same imaging modality, the spin history effects of patient motion can impact the recorded signal such that small changes in recorded BOLD signal are difficult to distinguish from noise due to motion. We

choose to use mutual information to quantify to BOLD signal information across the entire image sequence.

4.1.4 Implementation: Tools and Libraries

To calculate metrics, we used several existing tools and libraries. When no existing tool could be found, functions were implemented manually in Python3.

For the Dice coefficient calculation, we first had to create a binary version of each image volume. To binarize the image volumes, we used Simple ITK’s Otsu thresholding function. The binary images were then passes to a manually implemented function to calculate the Dice coefficient.

The correlation ratio between each possible pair of volumes in the sequence was calculated using bash and FLIRT (FMRIBs Linear Image Registration Tool) ([Jenkinson and Smith, 2001](#)) ([Jenkinson et al., 2002](#)). We then used the average and standard deviation of the correlation ratio distribution of each image to compare the images.

The mutual information calculation was implemented in two steps. The first step was to create a function that computes the joint histogram of the voxel value distributions between the two image volumes. This histogram was fed to a second function that converts the histogram counts to probabilities and calculates the mutual information value.

4.2 PATIENT CLASSIFICATION USING MOTION PATTERNS

We suggest that the ways that patients move are specific to certain age groups. For example, fetal patients live suspended in amniotic fluid and as such are subject to different physical constraints than patients in other age groups. Neonatal patients are often scanned using a “feed and bundle” protocol, which often results in them sleeping through the scan. However, neonatal patients sometimes wake up during the scan, and the way a baby woken up from a nap moves is different from how a fidgety preadolescent moves.

There is also a chance that patients within the same age group move differently possibly

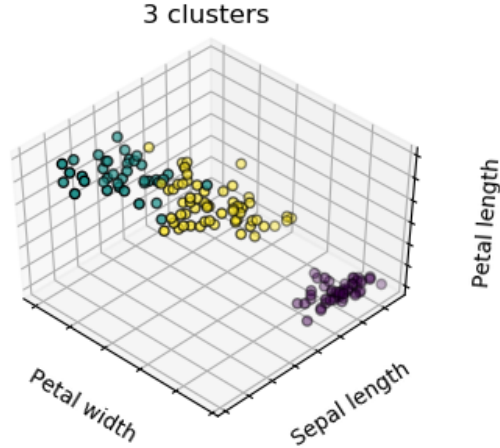


Figure 6: An example of k -means clustering performed on the Iris data set. The results of the algorithm are highly dependent on the number of clusters specified.

due to their cognitive state. Preadolescents who have ADHD likely become bored and fidgety in the MR scanner at different rates than their non-ADHD counterparts. Adults suffering from dementia may have more difficulty remaining still for the duration of a scan than adults from similar demographics with no dementia.

These patterns are essentially signals specific to different categories of patients. Machine learning techniques are useful for identifying patterns in signals from different sources. In addition to the motion metrics identified in the previous section, we will also use demographic and clinical data as features for our machine learning models.

The goal of applying machine learning to identify population level motion patterns lends itself well to unsupervised machine learning techniques. Unsupervised learning techniques group samples from a population based on the patterns in their features. They do not use information about any known groups in the population to inform their classification processes. In this section, we discuss several different unsupervised machine learning techniques used to measure degrees of association within subgroups of a data set.

4.2.1 K-means Clustering

K-means clustering divides a group of data samples with n features into k groups based on each sample's distance from the average value of the group ([Hartigan and Wong, 1979](#)), ([MacQueen, 1967](#)). In k-means clustering, the features of a set of data are viewed as the locations of each data sample in n -dimensional space. In this space, k cluster centroids are initially distributed. The distribution pattern can place the centroids either randomly between data samples or using randomly selected data points.

After the locations of the cluster centroids are initialized, the distance between each sample and each centroid is calculated. Each sample is assigned to the cluster represented by the centroid closest to it. Once the clusters are defined, the location of the centroid of each cluster is recalculated. The new centroid location is the mean of the locations of all samples in its cluster. The distance between each sample and each cluster centroid is recalculated, samples are reassigned to their closest cluster centroid, and the centroid of each cluster is recalculated. This process continues until a stopping criteria is fulfilled. With most unsupervised machine learning methods, the stopping criteria is that the classifications of the model do not change for a certain number of iterations. However, a maximum number of iterations is imposed on the learning process to prevent a model from running indefinitely. As a result, it is possible for a model to “time out” before reaching a stable state.

There are many variations of k-means clustering. For example, k-medians follows the same steps as k-means, but uses the median of the known data points in a cluster as the new centroid for that cluster ([Juan and Vidal, 1998](#)). Another variation called k-medoids uses the data point closest to the center of the cluster as the new cluster centroid rather than a descriptive statistic of the cluster ([Kaufman and Rousseeuw, 1987](#)).

One of the major limitations of k-means clustering is that the number of clusters must be given to the model. It is difficult to know how many clusters are needed to adequately represent subgroups within a data set. If too many clusters are used, the groups identified by the algorithm will be more granular than they should be; however, using too few clusters will produce large groups which mask distinct subgroups. An example of k-means clustering as applied to the Iris data set can be seen in Figure 6 ([Varoquaux, 2019](#)). The results of the

clustering are dependent on the number of clusters specified as well as the points used to initialize the algorithm.

4.2.2 Spectral Clustering

While spectral clustering is related to k-means clustering, it approaches the problem of identifying associations in a group of data from a different perspective. Spectral clustering treats each data point in a sample as a node in a graph. The connections between data points are characterized by the adjacency matrix and the degree matrix of the graph. These two matrices are used to calculate the Laplacian matrix of the graph, whose properties are used to identify clusters. All three matrices are $n \times n$ matrices, where n is the number of data points in the sample.

Herein, we discuss spectral clustering when the data can be represented using a simple graph. As such, certain mathematical shortcuts can be employed to simplify certain computations. A more general mathematical approach has been discussed by Ng, Jordan, and Weiss (Ng et al., 2002).

The adjacency matrix specifies the strength of the connection between the nodes represented by the rows and columns of the matrix. For data that does not begin in graph form, algorithms such as k-nearest neighbors can be used to generate the adjacency matrix. In the adjacency matrix, each entry i, j contains the weight of the connection between node i and node j . If the edges are unweighted, the value of the entry is either 0 or 1. If the graph is undirected, the value of entry i, j is the same as the value of entry j, i . All entries where $i = j$ should be 0, unless node i has a self-loop.

The degree matrix is a diagonal matrix which represents the number of edges connected to each node. If the graph is directed, the directionality of the degree matrix must be specified: a directed connection from node a to node b contributes to the count for node a if the degree matrix counts the number of edges that begin at each node (outdegree), but contributes to the count for node b if the degree matrix counts the number of terminating edges at each node (indegree). In the case of an undirected graph, the connections include all edges that begin or terminate at a node. To summarize, in an directed graph, each edge

contributes to only one node count while in an undirected graph each edge contributes to both nodes.

The adjacency matrix and the degree matrix are used together to construct the Laplacian matrix of the graph. This calculation of the normal Laplacian for a simple graph (undirected and containing no loops) is straightforward: the adjacency matrix is subtracted from the degree matrix. The resulting matrix has the following properties:

- The diagonals are the number of connections per node less the number of self-connections
- All off-diagonal values are the negative of the weight connecting node i to node j .

It is important to note that if the graph in question contains loops or is directional, other methods must be used to calculate the Laplacian matrix.

The Laplacian matrix can be used to explore many properties of a graph. In particular, the eigenvalues of the Laplacian matrix are informative about the number of connected components in the graph. Connected components are areas of the network that are connected to each other but not anything outside that component. Each connected component is not its own cluster, though: the connected components could be large and contain smaller sets of connected nodes that are good options for clusters.

To determine the number of clusters in the graph, the eigenvalues of the Laplacian matrix are sorted in increasing order. The number of zero-valued eigenvalues is the number of connected components in the graph. Eigenvalues close to zero suggest weak edges preventing some connected component from being two separate components. Manually examining these eigenvalues before performing spectral clustering can be informative about the number of clusters to create: the number of values below the first large gap between the eigenvalues are the number of clusters, k . The eigenvectors associated with these k eigenvalues are used as a lower-dimensional representation of the data in the graph. Performing k -means clustering on this data produces the labels for the clusters within the data that are not linearly separable otherwise.

The limitations of spectral clustering are strongly related to the process of remapping the data to a lower dimensional space. When reducing the number of features used to represent a data set, information about that data set is inherently lost. The missing information

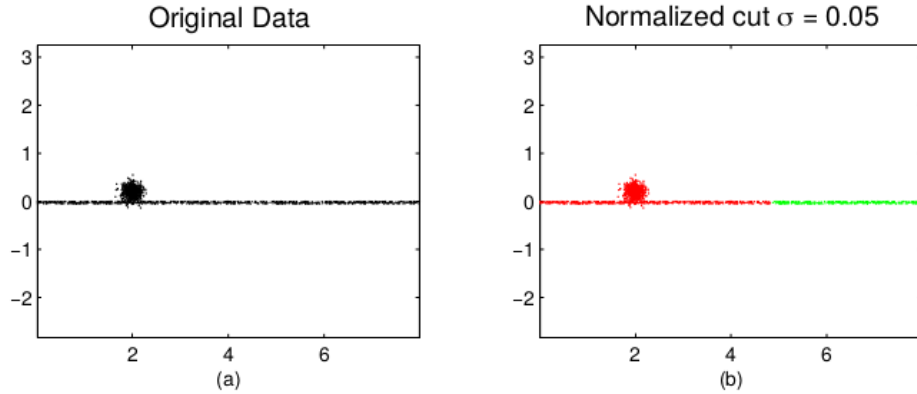


Figure 7: (a) Two different distributions, a 2D Gaussian density and a thin horizontal rectangle are difficult to separate (b) due to their overlap and the penalties built into the cost function of the spectral clustering algorithm. From (Nadler and Galun, 2007).

can make separating classes in the lower dimensional data significantly more difficult, if not impossible. Consider the following two cases: a case where two classes overlap and a case where three classes are unevenly represented in the data.

In cases where two seemingly obvious clusters overlap, the clustering algorithm may be unable to accurately identify them due to the mathematical penalties imposed on separating points in the feature space. An example of this problem as described by Nadler and Galun can be seen in Figure 7 (Nadler and Galun, 2007). The two distinct groups are the small 2D Gaussian density and the horizontal rectangle. The spectral clustering algorithm (in this case, the normalized cut algorithm) is unable to separate the groups because the degree of overlap between the Gaussian density and the rectangle is greater than the height of the rectangle. It is more cost-effective for the algorithm to make a vertical cut to divide the rectangle in two than to cut the Gaussian density away from the rectangle.

Uneven distributions of data classes can severely impact spectral clustering results. Consider the case where a data set contains one highly populated class with a wide variation in its data's features and two less populated classes with less variation in their data's features. The scale of the large, highly populated class can overshadow the smaller classes: if the three

most important eigenvectors are more related to the large class than the smaller classes, the algorithm will not be able to differentiate between the two smaller classes.

4.2.3 Agglomerative Clustering

Agglomerative clustering is a specific type of hierarchical clustering which builds a tree of similarities between data samples from the “bottom up” ([Ward, 1963](#)). The data samples in agglomerative clustering are also viewed as distinct points in n -dimensional space, but the number of groups to identify is not specified.

First, the distance from every data sample to every other data sample is calculated. The two data points that are closest together in terms of some similarity metric are combined into a single cluster. In the relationship tree representing the similarities between all data samples, a node is created and the joined data points are connected to that node. That node or cluster is treated as an intermediate data sample. The distance from the new “data sample” to every other data sample is calculated and the two closest data samples are again combined into another intermediate sample. A node representing the new cluster is added to the relationship tree and the data sample or samples merged into the cluster are connected to the node. The process of combining data points into clusters based on similarity to other data points terminates when all data points and clusters have been combined.

The results of agglomerative clustering can be interpreted by traversing the relationship tree. The relationship tree recorded the history of which nodes were merged into which clusters at each stage. Due to the nature of agglomerative clustering, these stages can be viewed as distinct levels in the tree. Beginning at the final node (the root) of the tree, the granularity of the clusters can be explored. At the top level, there is only one cluster, but at the second to last level of the tree there will be two clusters, at the third level there will be three clusters, and so on. How each cluster grew can reveal information about the relationships between the data samples within that cluster.

Agglomerative clustering also lends itself well to visualization via heatmap. The heatmap allows the researcher to see the distribution of feature values across the dataset and across visually prominent clusters. The Python library **seaborn** has a function called **clustermap**

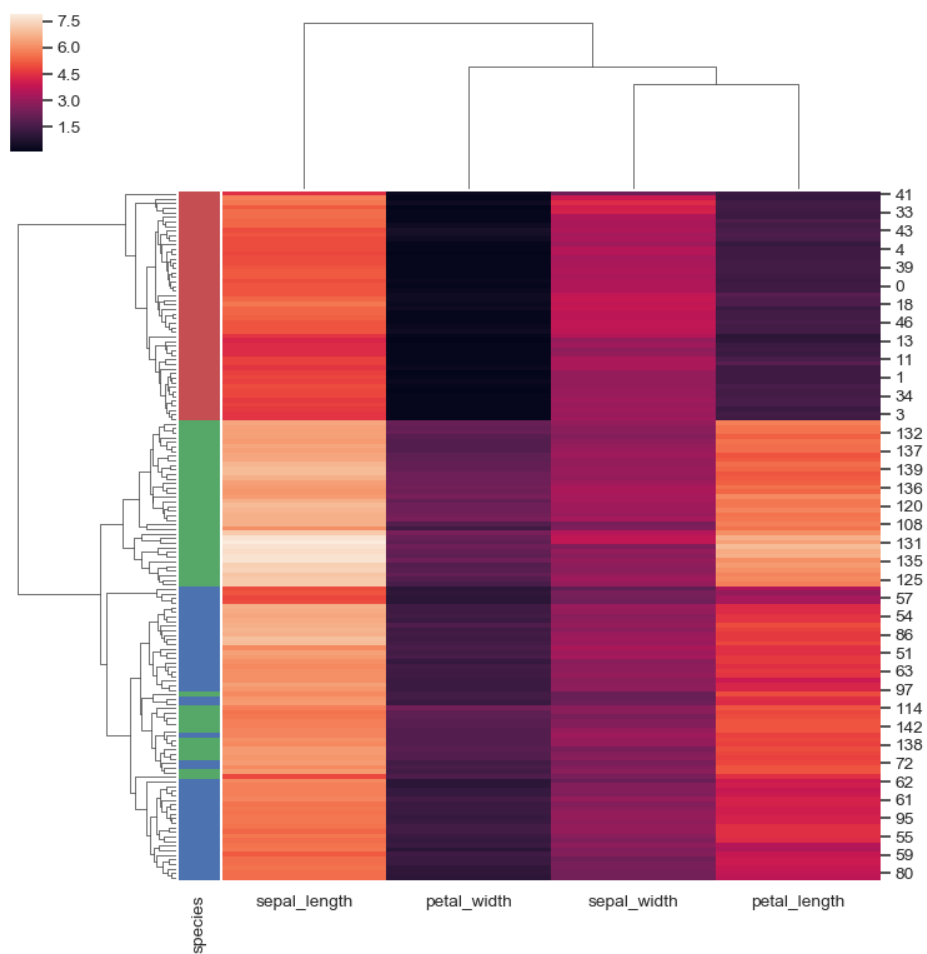


Figure 8: An example of agglomerative clustering on the Iris data set plotted using **seaborn**'s **clustermap** function.

which both performs agglomerative clustering and shows the resulting trees in a structured heatmap. An example of agglomerative clustering from the **seaborn** documentation where the clustering was applied to the Iris data set can be seen in Figure 8 ([Waskom, 2018](#)). Each column represents a feature and each row represents a single sample. The colorbar in the top left of the figure shows that lighter colors in each cell represent higher values. The dendrogram along the top of the heatmap shows the distance between each feature. The dendrogram along the left of the heatmap shows the distance between each data sample and the data sample most similar to it. The column immediately to the right of this dendrogram shows the known class (species) for each data sample. The class labels in conjunction with the dendrogram of the data samples show the distinct groups present in the data which were identified using agglomerative clustering.

4.2.4 Visualizing Clustering Results

The results of unsupervised clustering algorithms can be visualized to illustrate how the computer chose each group of samples. Depending on the number of features n for each data sample, a dimensionality reduction method may be needed to transform the location of the data sample in n -dimensional feature space to a more easily visualized 2-dimensional or 3-dimensional space. The three dimensionality reduction methods we consider are principle component analysis (PCA), T-distributed stochastic neighbor embedding (t-SNE), and uniform manifold approximation and projection (UMAP).

PCA. Principle component analysis is a multivariate statistical technique that can be used to transform a set of variables with some degree of intercorrelation into a set of new, independent, orthogonal variables ([Abdi and Williams, 2010](#)). These variables are called principle components of the data set. The principle components are ordered with respect to the amount of variance in the data set that can be projected onto each component. In general, PCA fits an p -dimensional ellipsoid to a data set with n features such that $p < n$. Each axis of the ellipsoid represents a single principle component. The first two or three principle components can be used to plot the results of a clustering algorithm in 2D or 3D space.

It is important to note that prior to the application of PCA, the data must be normalized. Normalizing the data allows different features to be compared on the same scale.

t-SNE. T-distributed stochastic neighbor embedding (t-SNE) was developed by Maaten and Hilton to perform nonlinear dimensionality reduction for visualizing high-dimensional data in a 2D or 3D space ([van der Maaten and Hinton, 2008](#)). The algorithm first constructs a distribution of the high-dimensional data to measure the pairwise similarity of all data points. It also constructs a second distribution to measure the pairwise similarity of the data points in the lower dimensional space. Then, it performs gradient descent to minimize the difference between the two distributions as measured by the Kullback-Leibler divergence. At each iteration of the gradient descent, the distribution of points in the lower dimensional space is modified. The algorithm converges when the distribution of pairwise similarities between data points in the lower dimensional space most closely matches the corresponding distribution in the original high-dimensional space.

t-SNE is a computationally expensive technique with a complexity of $O(N^2)$ where N is the number of data points. For this reason, it is recommended that data with more than 50 features undergo another form of dimensionality reduction before t-SNE is applied to a data set. Even when this recommendation is not followed, the lower dimensional data produced using t-SNE lacks the interpretability of PCA data: the resulting dimensions have no interpretable meaning.

UMAP. Uniform manifold approximation and projection (UMAP) was proposed as an alternative to t-SNE ([McInnes et al., 2018](#)). Rather than build a pairwise similarity distribution, UMAP uses topological representations of the data. For each point x_i , the distances between x_i and its k nearest neighbors are measured and normalized by the distance between x_i and the k th neighbor. These collections of distances around each point are local manifolds. The local manifolds are combined into the same global manifold using fuzzy simplicial sets. After the global of the data is known, it is used to determine where data points must lie in a lower dimensional space so that they both adhere to the known manifold topology and retain the distance metrics from their k nearest neighbors. The topology of the lower dimensional manifold is adjusted iteratively to minimize the cross-entropy between the higher dimensional representation and the lower dimension representation. In practice,

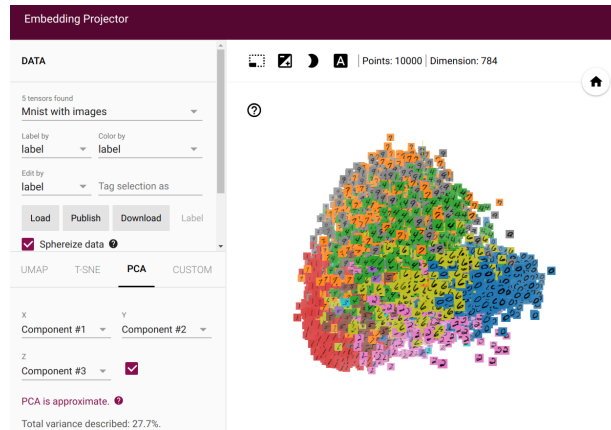
UMAP treats each data point as a node in a weighted graph. It first determines each point's k nearest neighbors and calculates the distances between them, and then computes a version of that topology in a lower dimensional space.

UMAP was developed under the belief that local structure is more important than global structure. It learns structures in a data set, even when the local structures can only be attributed to noise. It is not suitable for use in small, noisy data sets or in large data sets with only global (not local) structure. Figures produced using UMAP-reduced data should be interpreted with care: they could contain spurious structures from the data sample and not the target population. Additionally, UMAP is similar to t-SNE in that the dimensions produced by UMAP were generated nonlinearly and contain no true meaning.

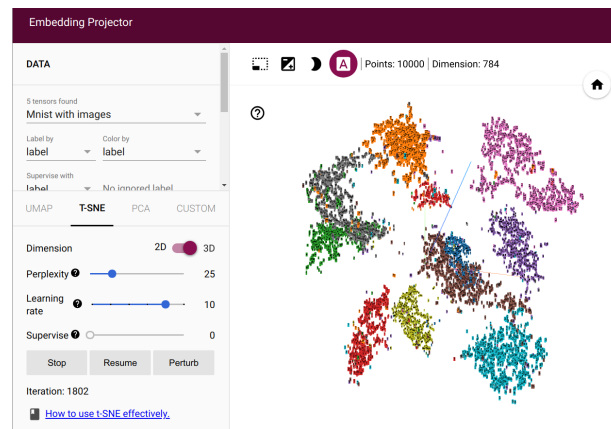
We performed a preliminary comparison of PCA, t-SNE, and UMAP for visualizing high dimensional data using TensorFlow's Projector tool ([TFP](#),). This tool is a web interface for visualizing high dimensional data from either built-in data sets or data sets uploaded by the user. It supports all three of the dimensionality reduction methods discussed previously in this section as well as a customizable projection of the entire data set to two or three feature vectors. The PCA, t-SNE, and UMAP visualizations of the popular MNIST handwriting data set can be seen in Figure 9.

4.3 PREDICTING PATIENT OUTCOMES USING MOTION PATTERNS

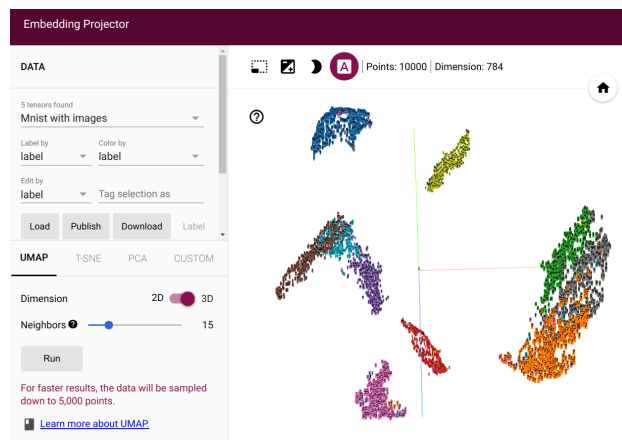
In addition to examining the patterns of patient motion using unsupervised machine learning techniques, these patterns will also be used with supervised machine learning techniques to determine the relationship between motion types and clinical outcomes. In this section, we first present several supervised machine learning methods and then discuss more generally the limitations of supervised machine learning and the metrics we will use to evaluate our models.



(a) PCA



(b) t-SNE



(c) UMAP

Figure 9: Visualization of MNIST data in 3D via TensorFlow Projector as generated using PCA, t-SNE, and UMAP dimensionality reduction techniques.

4.3.1 Regression

The first supervised machine learning method we discuss is regression. In general, regression maps a set of features to a set of outcomes. Each feature is weighted based on its contribution to the outcome. Features which are more relevant to the outcome have larger weights, while less important features have smaller weights.

The simplest version of regression is linear regression. Linear regression is used when the outcome being predicted has continuous values: a common example would be using the size of a house to predict its cost. The cost, y , would be modeled as

$$y = w_0 + w * x \quad (4.10)$$

where w is the weight assigned to the feature x , which is the size of the house, and w_0 is the weight for the bias in the model. As more features are added to the model, this equation generalizes to

$$y = w_0 + \sum_{i \in N} w_i * x_i \quad (4.11)$$

where w_i is the weight for feature i , x_i in the set of N features.

Alternatively, if the goal was to predict whether a house was owned or rented, linear regression would be a poor model choice. The goal of this problem is to identify a nominal class, not a value in a continuous interval. This type of problem is better suited for logistic regression.

Logistic regression takes the equation for linear regression and passes it through the logistic function to map it to a range of $[0, 1]$. The logistic function is

$$f(\pi) = \frac{1}{1 + e^\pi} \quad (4.12)$$

which means that a logistic regression models takes the form

$$y = \frac{1}{1 + e^{(w_0 + \sum_{i \in N} w_i * x_i)}} \quad (4.13)$$

This form of a logistic regression model is for binary, nominal outcomes, though multinomial logistic regression can model three or more outcomes and ordinal logistic regression can

model ordered, discrete outcomes. For the purposes of this document, when we say logistic regression, we mean the form which models binary, nominal outcomes.

The greatest strength and weakness of regression models is that they model linear relationships well. Linear models are fairly interpretable: the weights assigned to each feature in the linear model shows the importance the model believes that feature is. Interpretability is an important aspect of machine learning because people are more likely to trust a model if they can understand how it reached its conclusions. Unfortunately, it does not matter how interpretable the model is if the model is ill-suited for the data set. In particular, regression may have difficulty fitting data with nonlinear relationships.

4.3.2 Support Vector Machine

The mathematical framework for support vector machines (SVMs) was developed in 1963. In its original form, it could only be used to classify linearly separable data. SVMs treat data samples with n features as points in n -dimensional space. The SVM is composed of a collection of binary hyperplane classifiers. Binary hyperplane classifiers label data as belonging to a class or not belonging to that class depending on which side of the hyperplane the data is located. For a single binary hyperplane, the ideal location and alignment of the hyperplane is calculated using the following equation

$$\vec{w} \cdot \vec{x} + b = 0 \tag{4.14}$$

where \vec{w} is the vector of weights assigned to the features in \vec{x} and the variable b is a bias factor. This equation defines the hyperplane itself, but there are many hyperplanes that could satisfy this equation. The optimal hyperplane is determined using the support vectors.

The support vectors are the data points closest to the hyperplane. They define the location and orientation of the hyperplane. The space between the points on opposite sides of the hyperplane is called the margin, d . The optimal hyperplane is defined as the hyperplane whose \vec{w} and b result in the largest d .

The largest d occurs when the weights for the data samples are minimized. The weights indicate how important a data sample is in defining the hyperplane. Data samples which

do not increase the size of d (are not support vectors) should not contribute to the model. These samples should be assigned weights of 0.

When the ideal \vec{w} and b parameters have been determined, data on one side of the hyperplane is labeled as belonging to one class while the data on the other side of the hyperplane does not belong to that class. In a two class scenario, data that does not belong to one class clearly must belong to the other class. As more classes are added to a data set, the number of hyperplanes must also increase. Instead of optimizing a single hyperplane, the entire collection of hyperplanes must be optimized together.

In some cases, data with n dimensions may not be separable in n -dimensional space. In 1992, it was proposed that the original data could be mapped to a higher dimensional space where it would be linearly separable. The SVM could be built in that space and would still function as a linear classifier, even though it would appear to be a nonlinear classifier in the original space. Different kernel functions have been developed.

After a SVM model has been trained, the kernel used to map the data from n -dimensional space to the higher dimensional space is used to map new data to that space. The new data is assigned labels depending on where it lies in the higher dimensional space.

SVMs are versatile supervised learning techniques that perform well in classifying both linearly and nonlinearly separable data. By their very nature, they find the globally optimal solution. However, finding the optimal parameters for a SVM model can be a computationally expensive and complex process depending on the characteristics of the data samples.

4.3.3 LSTM Recurrent Neural Network

One of the most popular supervised learning algorithms is the artificial neural network. A basic artificial neural network is composed of connected layers of units modeled after neurons in a biological brain. Every artificial neural network has at least two layers: an input layer and an output layer. The number of neurons in the input layer is the same as the number of features in the data being fed to the network. The input layer is connected to the output layer by weighted edges. For a network with n features in the input layer and one neuron in

the output layer, the value predicted by the network for data point \vec{x} is given as

$$f(\vec{x}) = \vec{w} \cdot \vec{x} + b \quad (4.15)$$

where \vec{w} is the weight assigned to the edge connecting each input neuron to the output neuron, \vec{x} is the values of the input vector, and b is an offset factor.

Layers can be added between the input layer and the output layer to model more complex relationships. These layers are called hidden layers because they are not seen at the data input or model output. The value of each neuron in each layer can be calculated using the values of the neurons in the previous layer, which means that for two layers, Equation 4.15 expands to

$$f(\vec{x}) = \vec{w}_2(\vec{w}_1 \cdot \vec{x} + b_1) + b_2 \quad (4.16)$$

More generally, Equation 4.15 can be written as

$$f_n(\vec{x}) = \vec{w}_n f_{n-1}(\vec{x}) + b_n \quad (4.17)$$

where the dot product of the weights of the current layer w_n and the output $f_{n-1}(\vec{x})$ of the previous hidden layer $n - 1$ are offset by some bias factor b_n to produce the output $f_n(\vec{x})$ of the current layer. For the first layer of the network, the output is calculated using Equation 4.15.

To model nonlinear relationships in data, this equation must be generalized further to allow for activation functions. Activation functions are intended to represent the action potential firing in a biological neuron. A biological neuron is either activated or not activated, but the activation function of a neuron in an artificial neural network is not limited to binary states. For example, the output of a rectified linear unit (ReLU) is in the range $[0, \infty)$, a sigmoid function's output is in the range $(0, 1)$, and a hyperbolic tangent produces a value in the range $(-1, 1)$. Different activation functions are used for different application depending on the desired behavior of the model.

We represent the activation function generically as $g_n(\cdot)$ and rewrite Equation 4.17 as

$$f_n(\vec{x}) = g_n(\vec{w}_n f_{n-1}(\vec{x}) + b_n) \quad (4.18)$$

Until this point, we have been describing feed-forward neural networks. All of the connections flow in a single direction from the input nodes to the output nodes. Networks built using a feed-forward paradigm are often used for pattern recognition or other cases where a given input is associated with a known output. However, neural networks can also have connections that skip layers, link back to previous layers, or connect to other neurons in the same layer. This type of network is called a recurrent neural network.

One particularly interesting type of recurrent neural network is a long short-term memory (LSTM) network. LSTM networks have more complex unit structure than basic neural networks. LSTM units are composed of a memory component and three types of gates: an input gate, an output gate, and a forget gate. The memory component tracks the current value of the unit. The input gate dictates how much data being passed to the cell impacts the memory component, the forget gate dictates how long a value is stored in the memory component, and the output gate dictates the impact of the value in the memory component is used to produce the output activation of the unit. Due to the nature of the LSTM units, networks made of LSTM units have an advantage over feed-forward networks when working with time-series data.

One of the major drawbacks of both regression and SVMs is that the data used to train these models must be in feature vector form. Neural networks have the ability to work with more complex input data. They have been used for tasks as complex as speech recognition and video processing using the audio or video itself as input. Their ability to work with data directly is a key strength of this type of technique. However, sequential data requires more memory than feature vectors. Similarly, the structure of artificial neurons needed to process and learn from these sequences is more complex and computationally expensive than regression, SVMs, or smaller and simpler neural network structures.

4.3.4 Application of Supervised Machine Learning

Generally, the outcomes of interest when applying supervised machine learning to medical data are some definition of normal and abnormal. We choose to perform two different analyses based on two definitions of normal.

The first definition of normal is that enough motion can be removed from the image that the image is usable. The abnormal label is that the image cannot be recovered based on the patient's motion patterns.

The second definition of normal is that the patient is functioning typically. We choose to identify the opposite of this label as “the patient **may** not be functioning typically” because of the heterogeneity of our data. CHD is a heterogeneous disease with many presentation types, and the neurodevelopmental disorders add another degree of granularity and complexity to a subject's clinical diagnosis. While it would be impressive to be able to build a clinical decision support tool that can diagnose a patient as having a particular form of CHD accompanied by a specific neurocognitive disorder, this goal is not the purpose of this project.

If a machine learning model reaches 100% accuracy on both training and test data sets, data scientists should immediately assume something has gone wrong either with the model itself or with the training and testing data. Current machine learning models suffer from the difficulty of balancing two sources of error: bias and variance. Bias is the degree to which the machine learning model matches the underlying model of the training data. Variance is the breadth of the distribution of the data from the population of interest covered by the training data. Models with low bias and high variance overfit the training data: they model the training data well but generalize poorly to new data. Conversely, models with high bias and low variance underfit the training data: they fit the training data poorly, possibly because they learned noise in the training data rather than the signal. Underfitted models fail to capture the important signals from the training data and perform poorly overall.

A good model neither overfits nor underfits the training data. It has low bias and low variance, and the challenge of balancing these two sources of error has been discussed elsewhere but is important to address here to set realistic expectations about the training and testing classifications of a model. Ideally, the model will classify both training and

Table 1: An example of a truth table for a binary classifier predicting the presence or absence of a condition.

		<i>Actual</i>	
		Condition True	Condition False
<i>Predicted</i>	Condition True	True Positive (TP)	False Positive (FP)
	Condition False	False Negative (FN)	True Negative (TN)

testing data well, but it is not possible with current techniques and data availability for a model to have perfect classification of every data sample.

The “wellness”/“goodness” of a binary classification model is determined using a truth table. A truth table is a $2 * 2$ table filled with the number of occurrences where data was classified correctly and incorrectly as belonging to each class. An example table can be seen in Table 1.

Various metrics can be calculated from the truth table, such as sensitivity and precision. Sensitivity measures how well the model performed at correctly identifying actually true data samples:

$$sensitivity = TPR = \frac{TP}{TP + FN} \quad (4.19)$$

Precision measures the ratio of positive predictions to actually true data:

$$specificity = PPV = \frac{TP}{TP + FP} \quad (4.20)$$

These metrics are also known as the true positive rate and the positive predictive value, respectively.

These metrics are independently informative about different aspects of the model, but during training only one metric is used to evaluate a model’s performance. Accuracy, for

example, is a measure of how many data samples were classified correctly:

$$A = \frac{TP + TN}{TP + TN + FP + FN} \quad (4.21)$$

We choose to use the balanced F1 score to evaluate the success of our supervised learning models. The balanced F1 score is calculated as:

$$\begin{aligned} F1 &= \frac{2 \cdot TPR \cdot PPV}{TPR + PPV} \\ &= \frac{2 \cdot TP}{2 \cdot TP + FP + FN} \end{aligned} \quad (4.22)$$

The balanced F1 score places equal value on a model correctly identifying actually true data compared to false data as well as identifying as much actually true data as possible. Accuracy only accounts for the number of correctly classified data samples. In cases where all classes in a data set are not evenly represented, the balanced F1 score produces a more robust model than accuracy.

4.4 DESCRIBING MOTION PATTERNS

In previous sections we describe practical knowledge about how fetal, neonatal, preadolescent, and adult patients move in different ways during MRI scans. We wish to quantify these movement patterns using the metrics described earlier in this chapter and identify appropriate terminology that can be used to describe them.

5.0 DATA

The data used to test the hypothesis and aims introduced in the previous chapter are drawn from a set of simulated rs-fMRI sequences and three clinical groups. In this chapter, we will first discuss the need for simulated sequences and the processes used to generate them for our work. Then, we will discuss the clinical images which were taken from several prospective studies of congenital heart defects in three age groups of pediatric patients. These groups were chosen because congenital heart disease (CHD) affects patients throughout their lifespans and different characteristics in motion patterns have been observed in patients of different ages with and without CHD.

5.1 SIMULATED SEQUENCES

There are two major barriers in research surrounding motion correction in rs-fMRIs: gathering data and measuring the effects of the technique.

The challenge of gathering significant amounts of data is common across the medical domain. Simulating realistic patient scans can mitigate this challenge and make rs-fMRI research more accessible.

Research on motion correction in rs-fMRIs often focuses on the amount of the positional effects of motion removed from the image. This silver standard is used because the gold standard, the amount of brain signal recovered by motion correction, is unknown in clinical images. When an rs-fMRI is simulated, the amount of brain signal in the sequence can be manually specified. The known brain signal can be used to evaluate motion correction techniques with respect to the amount of brain signal recovered by the technique.

In this section, we elaborate on a simulation we designed and implemented to address both of these barriers.

5.1.1 Background

It is difficult to obtain enough data from a large number of subjects to perform large-scale studies in the medical domain. Collaborators can band together to create a larger and more diverse data set by participating in multicenter studies, though there are some challenges associated with multicenter studies. Each site will have a different scanner, potentially with different field strengths and from different manufacturers. Even ignoring the challenges of harmonizing data obtained using scanners from different companies, each scanner has its own set of unique inhomogeneities in the primary magnetic field. Additional scans of inanimate or human phantoms may be necessary to characterize the differences between all of the scanners involved in a multicenter study.

The second barrier to motion correction in rs-fMRI research is the complexity of identifying a gold standard metric to use when evaluating motion correction techniques. The current criteria for determining the usability of an rs-fMRI sequence developed by Power et al. evaluate motion correction techniques in terms of the reduction of positional differences and signal differences between neighboring volumes. Unfortunately, this approach does not measure the amount of signal recovered or lost through motion correction. A true gold standard evaluation of motion correction would be able to evaluate the BOLD signal present in the image before and after correction. If the BOLD signal prior to patient motion was known, though, there would be no need for image processing in the first place: we would already have the data we are trying to obtain with motion correction.

We address these two barriers by creating a mechanism for generating simulated image sequences. The generated sequences contain simulated brain signal based in areas of the brain associated with resting-state connectivity, scanner noise, and patient motion. Our mechanism can create large quantities of unique image sequences. The simulated image sequences can also serve as a gold standard for evaluating volume registration and motion correction techniques: the signals and noise sources added to the sequence are known because

they are generated as part of the simulation.

5.1.2 SPECTr: Simulated Phantom Emulating Cranial Transformations

Our mechanism is called Simulated Phantom Emulating Cranial Transformations (SPECTr). A phantom is an object designed to have material properties which mimic those of a specific tissue type or organ. Phantoms, either manufactured objects or healthy humans, are used in multicenter studies to obtain images of the same object or person from multiple scanners. These images are used to harmonize the data taken from the different sites. We call our simulated sequence a phantom because the baseline image itself is known as are the signals added to it to simulate brain activity.

When developing the pipeline for SPECTr, it was important to consider the multiple facets of rs-fMRI sequences. BOLD signal must be present in areas of the brain associated with resting-state neuronal networks. The effects of motion and various impacts they have on the BOLD signal must also be present. As discussed in Chapter 2, the three effects of motion are positional, spin history, and susceptibility. The positional effects of motion are straightforward to implement. For simplicity, we model the spin history and susceptibility effects as a single source of in-scanner noise.

5.1.3 Materials

In order to simulate resting-state BOLD signal in an fMRI, two pieces of anatomical information are required. The first is structural information about the brain. The second is the location of functional networks associated with the resting-state BOLD signal.

While it is possible to use clinical images for the structural information, the goal of SPECTr is to be generalizable both for our use and for the use of other researchers. Additionally, clinical images inherently contain some degree of signal from some neuronal processes which could obfuscate the simulated BOLD signal.

In 1992, the International Consortium for Brain Mapping was formed to develop a set of standards for what is considered a healthy human brain. They used their criteria to develop an initial set of “average” brain structural scans based on scans from healthy volunteers.

This original set of average brain scans incorporates scans from 305 subjects and is referred to as the MNI305 data. As MRI technology has evolved, the spatial resolution capabilities of the MRI scanners has increased. In 2001, another set of 152 healthy volunteers was recruited to create a higher resolution data set. The scans from the new cohort were linearly registered to the MNI305 data to create the new MNI152 images.

Herein, we use the MNI152 data set as available at the website for the McConnell Brain Imaging Centre at McGill University (Fonov et al., 2009) (Fonov et al., 2011). This data set contains five images: a T1-weighted scan, a T2-weighted scan, a proton density weighted scan, and two binary masks for the head and the brain. Each of the structural scans was designed to highlight the properties of different tissues in and around the brain. Proton density scans were developed for the purpose of detecting blood-related signal. As BOLD images essentially perform the same purpose as a proton density image over a period of minutes, we choose to use the proton density weighted scan as the structural base for the simulated images.

The functional network information is more difficult to find than structural atlases. The Functional Imaging in Neuropsychiatric Disorders Lab at Stanford has developed two sets of functional atlases. The atlases are divided into regions of interest (ROIs) associated with individual networks. The first set of atlases contains 90 functional ROIs which compose 14 networks (Shirer et al., 2012). The second set of atlases contains 499 functional ROIs and has more gray matter coverage (Altmann et al., 2015). We chose to use the original ROIs associated with the dorsal and ventral default mode networks.

5.1.4 Simulation Pipeline

5.1.4.1 Baseline Sequence The process for generating a simulated sequence using the data discussed in the previous section has several steps. An overview of the pipeline can be seen in Figure 10. We cover these steps in detail in this section.

The MNI152 proton density image is a whole head image. To remove the skull, we apply the brain mask to the proton density weighted image. The resulting image contains only brain tissue.

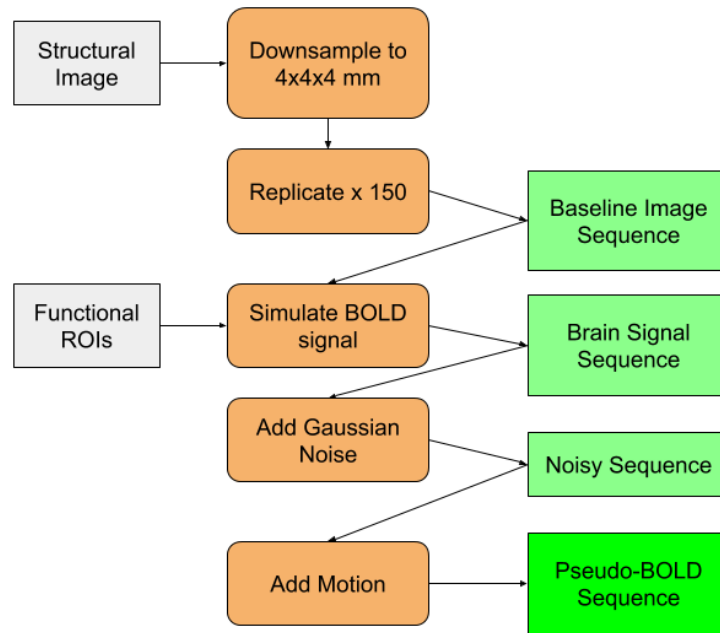


Figure 10: An overview of the SPECTr simulation pipeline. Using atlas data, a simulated phantom containing brain signal, scanner noise, and patient motion is generated.

The spatial resolution of the structural brain image is 1 mm^3 . The spatial resolution for a single volume in a rs-fMRI sequence is less granular at 4mm^3 . To achieve this resolution, the structural volume must be downsampled. After the downsampling, the size of the structural image is reduced from $181 \times 217 \times 181$ voxels to $45 \times 54 \times 45$ voxels.

Now that the structural image is the correct spatial resolution, it must be replicated to create the temporal sequence. Part of this step includes creating a new dimension in the data. The affine matrix which represents the resolution of the image has the following structure:

$$\begin{bmatrix} r_x & 0 & 0 & c_x \\ 0 & r_y & 0 & c_y \\ 0 & 0 & r_z & c_z \\ 0 & 0 & 0 & 1 \end{bmatrix} \quad (5.1)$$

where r_x, r_y , and r_z represent the spatial resolution in the x, y , and z axes, respectively and c_x, c_y , and c_z represent the location of the origin in voxels. To convert the image from a 3D volume to a 4D sequence, we add a row and a column to this matrix so that it now has the structure:

$$\begin{bmatrix} r_x & 0 & 0 & 0 & c_x \\ 0 & r_y & 0 & 0 & c_y \\ 0 & 0 & r_z & 0 & c_z \\ 0 & 0 & 0 & t & 0 \\ 0 & 0 & 0 & 0 & 1 \end{bmatrix} \quad (5.2)$$

where t is the desired temporal resolution. We choose a temporal resolution of 2 seconds for our simulated sequence. The downsampled image volume is replicated and concatenated along the new temporal dimension to create a sequence that is 150 image volumes long. This sequence is referred to as the base phantom sequence as it contains no brain signal, noise, or motion.

5.1.4.2 Brain Signal The next step in the pipeline is to add BOLD signal to the sequence. We combine the functional ROIs from the dorsal and ventral default mode networks

into a single binary functional ROI image. This image is referred to as the default mode network (DMN) mask.

For each nonzero voxel in the DMN mask, a temporal signal is generated. We chose to model the BOLD response as a cosine signal following the formula

$$s(\vec{v}, t) = a * (\cos(f_0 * (t - t_{shift})) - a_{shift}). \quad (5.3)$$

This equation is for a scaled cosine function with both temporal and amplitude shifts. The temporal and amplitude shifts, t_{shift} and a_{shift} respectively, are randomly generated for each voxel from uniform distributions. Once chosen, they are consistent across the voxel's generated temporal signal. The other parameters, a and f_0 , were specified using existing research.

In 2007, Biswal et al. performed a study evaluating methods to reduce changes in the BOLD signal not directly related to brain activity (i.e., vascularity). They identified a low-frequency spectral amplitude of 0.04 Hz as the highest frequency related to BOLD signal consistent not only through scans of individual patients but in group-wise analyses. Based on their work, we chose the fundamental frequency f_0 to be 0.04 Hz (Biswal et al., 2007).

The scaling factor a was chosen based on Power et al.'s usability criteria. As they state that any signal change between volumes above 2.5% of the maximum voxel value is unlikely to be due to brain activity, we used an amplitude of 20 units on a scaled voxel value range of $[0, 1000]$ (Power et al., 2012).

The generated BOLD signals were added to the baseline image sequence, but were also saved in a separate image sequence file for reference during analysis. The generated sequence with only BOLD signal is referred to as the brain signal sequence.

5.1.4.3 Scanner Noise The next step in the pipeline is to add scanner noise to the brain signal sequence. In a regular rs-fMRI of a patient, the noise in the sequence is the result of two factors: the spin history effects of motion and the susceptibility effects of motion. To simplify the simulation, we choose to model the resulting noise rather than the individual sources.

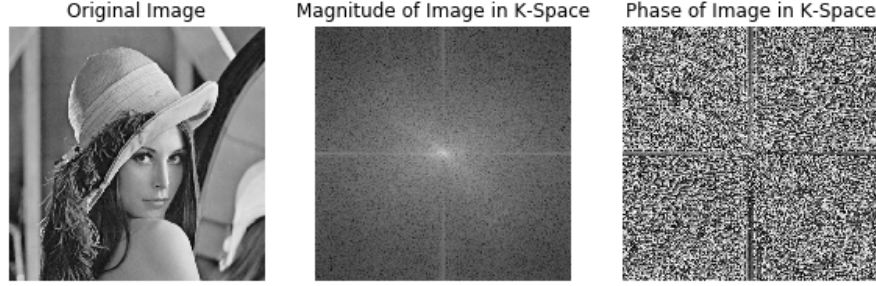


Figure 11: An example of the magnitude and phase of an image in k-space.

Signal acquired by MRI scanners is first recorded as a raw data matrix in k-space. K-space contains spatial frequency information. The coordinate system of k-space differs from the coordinate system of physical space. In k-space, the closer a point is to the center of a zero-centered data matrix, the lower its frequency or phase. The brighter a point in the raw data matrix is, the larger its magnitude. An example of the magnitude and phase of an image in k-space can be seen in Figure 11.

Generally speaking, images contain more low frequency information than high frequency information. We wish to be able to control the amount of noise added to the magnitude and phase components independently, so we choose to add noise to the sequence in k-space.

When adding scanner noise to the brain signal sequence, we add noise to each image volume independently. The image volume is transformed from physical space into k-space using the fast Fourier transform (FFT). To force the image to be zero-centered, we perform a FFT shift on the Fourier space data. A matrix the same size and shape as the image volume is created. The matrix is then filled with complex Gaussian noise, $n(\vec{l})$ where

$$|n(\vec{l})| = w_m * r_m, r_m N(0, 1) \quad (5.4)$$

and

$$\angle n(\vec{l}) = w_p * r_p, r_p N(0, 1) \quad (5.5)$$

In these two equation, \vec{l} is the location of the point in the matrix, w_* represents the weight assigned to the component, r_* represents the noise random variable independently generated from a standard normal distribution, and the subscripts m and p refer to the magnitude and phase components, respectively. The complex noise is weighted so that the magnitude of the noise has a greater contribution than the phase of the noise, that is $w_m > w_p$.

The matrix of complex noise is added to the zero-centered k-space image volume. The noisy k-space volume is unshifted and undergoes an inverse Fourier transform to change the data back to physical space. This sequence containing both brain signal and scanner noise is referred to as the noisy sequence.

5.1.4.4 Patient Movement Now that the ground truth brain orientation and BOLD signal have been established, patient motion can be added to the BOLD phantom sequence. One of the aims of this document is to establish that patients from different populations exhibit different motion patterns. As we have not yet established what those motion patterns are, we developed a generic motion model for the simulation.

During an rs-fMRI scan, a patient theoretically has the freedom to rotate his head around three different axes, translate his head along three different axes, or some combination of translations and rotations. Realistically, once a patient has settled in the scanner, it becomes difficult for his head to only undergo translation. It is more likely that he will rotate his head. For the simplicity of the simulation, we assume no head translations occur during the scan.

A rotational transformation can be represented as a matrix. Rotations about a single axis are represented as followed:

$$R_x(\alpha) = \begin{bmatrix} 1 & 0 & 0 \\ 0 & \cos\alpha & \sin\alpha \\ 0 & -\sin\alpha & \cos\alpha \end{bmatrix} \quad (5.6)$$

$$R_y(\beta) = \begin{bmatrix} \cos\beta & 0 & -\sin\beta \\ 0 & 1 & 0 \\ \sin\beta & 0 & \cos\beta \end{bmatrix} \quad (5.7)$$

$$R_z(\gamma) = \begin{bmatrix} \cos\gamma & \sin\gamma & 0 \\ -\sin\gamma & \cos\gamma & 0 \\ 0 & 0 & 1 \end{bmatrix} \quad (5.8)$$

Rotational transforms are applied to the origin of the image. However, the origin of the image is not necessary anatomically significant. Head motion naturally occurs about the base of the neck. We can approximate the location of the base of the neck by calculating the center of mass of the brain. First, the image volume is thresholded to separate the brain from the background. Then the locations of the “on” voxels are averaged to calculate the center of mass.

Motion is added to the noisy image sequence one volume at a time. No motion is applied to the first volume in the sequence, but volume is used to calculate the center of mass of the brain. For each subsequent volume, the angles of rotation about the x-, y-, and z-axes are each randomly generated from a standard normal distribution to create rotational change matrices, $R_{*,\Delta}$ (where the subscript $*$ represents x , y , or z). The new rotations $R_{*,\Delta}$ are added to the rotations from the previous step $R_{*,i-1}$ to create the rotation matrices for the current volume, $R_{*,i}$:

$$R_{*,i} = R_{*,i-1} + R_{*,\Delta} \quad (5.9)$$

The three rotational transformations are combined into one matrix via multiplication:

$$R_i = R_{x,i}(\alpha)R_{y,i}(\beta)R_{z,i}(\gamma) \quad (5.10)$$

The compound transformation R_i is then applied to the image at the center of mass calculated from the original image volume. *Note: Since the simulation is constrained by the assumption of no head translations, the center of mass will remain consistent throughout the image sequence.*

After motion has been added to every image volume in the sequence, the final sequence (labeled Pseudo-BOLD Sequence in Figure 10) is ready to be used in motion correction analyses.

5.1.5 Implementation

SPECTr is implemented in Python (version 3.7.3). The `nipy` library (version 0.4.1) was used to load images, save images, and combine the functional ROIs. The `numpy` library (version 1.17.4) was used for matrix manipulations involved in the brain signal and noise generation steps. The image processing library `skimage` (version 0.14.2) was used to calculate the center of mass. The Python wrapper `SimpleITK` (version 1.2.4) of the Insight Toolkit library for image analysis was used to perform the rotational transformations associated with patient motion.

The SPECTr source code is available on Github: <https://github.com/jmschabdach/SPECTr>.

5.1.6 Simulated Sequences Experiments

We generated 90 image sequences from the MNI152 proton density image and the default mode network functional ROIs using the process described in the previous section. The image sequences were divided into three groups with different degrees of scanner noise. All simulated images underwent both registration techniques described in Chapter 3. The registered images also underwent independent component analysis (ICA) using FSL’s MELODIC (Multivariate Exploratory Linear Optimized Decomposition into Independent Components) tool.

The registered images underwent the same type of analysis as the clinical images. The ICA technique was used to determine how much brain signal was recovered by each registration technique.

This particular experiment is be one of the first to investigate how much true BOLD signal is preserved through motion correction. One of the major drawbacks to existing motion correction pipelines is that they remove signal along with noise. In clinical data, there is no way to know the ground truth signal contained within the image; however, simulated phantom images have a *de facto* known ground truth signal. The design for this experiment can be used to evaluate how much BOLD signal is recovered by other motion correction pipelines, and how close the recovered signal is to the signal of interest.

5.2 CLINICAL COHORTS

Our clinical cohorts are composed of healthy subjects and subjects who have congenital heart disease (CHD). The phrases congenital heart defects (CHDs) and congenital heart disease (CHD) both refer to defects in the heart or the vessels around the heart. CHDs affect how blood moves into, through, and away from the heart. CHD has a worldwide prevalence of about 8 per 1000 live births, meaning about 1.35 million children are born with CHD every year. Many CHD patients are also affected by comorbidities, including neurodevelopmental disorders. Since the survivability of CHD has increased from 10% to 90%, the medical community is faced with a growing, aging population of CHD patients with a variety of neurological needs. Subjects in CHD studies provide a diverse set of data, particularly when it comes to studying motion in rs-fMRIs.

In this section, we provide a general overview of the impact of CHD on a global scale, the process for diagnosis, and additional risks associated with CHD. We then discuss the process of diagnosing neurodevelopmental comorbidities occurring with CHD and the impact of improved medical care on the CHD population. We end this section with a description of the three populations from which we obtained clinical rs-fMRI sequences.

5.2.1 CHD Background

CHD consists of a variety of defects which can affect any combination of the vessels and chambers of the heart with varying degrees of severity. The defects prevent the cardiopulmonary system as a whole from functioning correctly, but pinpointing and treating the defects effectively can be a complex process. It is important to note that each defect type has a different prevalence, a different treatment plan, and different expected outcomes. A breakdown of prevalence rates of some of the most common lesion types can be seen in Figure 12.

Different presentations of CHD are associated with a number of different genetic and environmental factors (Mozaffarian et al., 2016). Genetic conditions such as Down syndrome, Turner syndrome, 22q11 deletion syndrome, Williams syndrome, and Noonan syndrome are associated with certain CHD presentations. Maternal behaviors such as smoking and binge

Table 15-3. Estimated Prevalence of Congenital Cardiovascular Defects and Percent Distribution by Type, United States, 2002* (in Thousands)

Type	Prevalence, n			Percent of Total		
	Total	Children	Adults	Total	Children	Adults
Total	994	463	526	100	100	100
VSD†	199	93	106	20.1	20.1	20.1
ASD	187	78	109	18.8	16.8	20.6
Patent ductus arteriosus	144	58	86	14.2	12.4	16.3
Valvular pulmonic stenosis	134	58	76	13.5	12.6	14.4
Coarctation of aorta	76	31	44	7.6	6.8	8.4
Valvular aortic stenosis	54	25	28	5.4	5.5	5.2
TOF	61	32	28	6.1	7	5.4
AV septal defect	31	18	13	3.1	3.9	2.5
TGA	26	17	9	2.6	3.6	1.8
Hypoplastic right heart syndrome	22	12	10	2.2	2.5	1.9
Double-outlet right ventricle	9	9	0	0.9	1.9	0.1
Single ventricle	8	6	2	0.8	1.4	0.3
Anomalous pulmonary venous connection	9	5	3	0.9	1.2	0.6
Truncus arteriosus	9	6	2	0.7	1.3	0.5
HLHS	3	3	0	0.3	0.7	0
Other	22	12	10	2.1	2.6	1.9

Average of the low and high estimates, two thirds from low estimate.²ASD indicates atrial septal defect; AV, atrioventricular; HLHS, hypoplastic left heart syndrome; TGA, transposition of the great arteries; TOF, tetralogy of Fallot; and VSD, ventricular septal defect.

*Excludes an estimated 3 million bicuspid aortic valve prevalence (2 million in adults and 1 million in children).

†Small VSD, 117 000 (65 000 adults and 52 000 children); large VSD, 82 000 (41 000 adults and 41 000 children).

Source: Data derived from Hoffman et al.²⁴

Figure 12: Table of prevalences of congenital heart defects as compiled by (Mozaffarian et al., 2016).

drinking are known to cause heart problems in the fetus. Other maternal risk factors are obesity, folate deficiency, and living at a high altitude. Paternal exposure to phthalates, anesthesia, sympathomimetic medications, pesticides, and solvents may increase the risk of the fetus for developing CHD. While there are quite a few factors in this list, there are many CHD cases whose causes are unknown.

Once a patient is diagnosed with one of these defects or a cause of the CHD is identified, the specific nature of his case must be clearly documented. The documentation of CHD using the International Classification of Diseases, Ninth Revision, Clinical Modification (ICD-9-CM) has 25 high level codes representing various presentations of CHD, but these codes used alone are often not sufficient for describing a patient's true condition (Mozaffarian et al., 2016). Additional ICD-9-CM codes should be used to communicate the finer details of a patient's condition, if they are available.

The incidence of CHD in live births vary across countries and continents. The United States reports approximately 4-10 CHD case per 1000 live births. Europe and Asia see about

6.9 and 9.3 CHD cases per 1000 live births, though smaller studies have been conducted in many countries to measure local prevalence ([Mozaffarian et al., 2016](#)). In China, the incidence of CHD ranges from 8.98 to 11.1 per 1000 live births ([Zhao et al., 2019](#)) ([Qu et al., 2016](#)). A pair of studies from Iran report incidences of 8.6 and 12.3 per 1000 live births, though the studies note that they were performed in different geographical locations with different populations within the country ([Nikyar et al., 2011](#)) ([Rahim et al., 2008](#)). One report from Dharan reports an incidence of 5.8 per 1000 patients admitted to a tertiary care hospital over a 12 month period ([Shah et al., 2008](#)). A study of newborns at one hospital in New Delhi, India claims an incidence of 3.9 per 1000 live births, though this rate may be a poor estimate as there is a significant delay between patient birth and referral to a cardiac center in India ([Khalil et al., 1994](#)) ([Saxena, 2005](#)).

These incidence rates should be analyzed with some caution. In many cases, the reported rates were based on medical records. Medical records are not always correct; it is well known that human error can lead to a medical record lacking information or containing incorrect information. The only way for a person to have a medical record is for him or her to go to a medical center. Not everyone who has CHD is able to seek medical help, often because of their geographical locations or their income. Even if a patient is able to seek medical help, the availability of proper cardiac care varies between and within countries. However, it is generally expected that CHD incidence rates will increase as screening tools and treatments become more effective and more widespread, leading to earlier detection of defects.

Currently, the process of detecting and diagnosing CHD can begin before birth. A specialized ultrasound test called fetal echocardiography can detect heart abnormalities as early as the second trimester of the pregnancy. People who learn they are pregnant with a fetus who shows signs of CHD may choose to handle this information by opting for termination or pursuing a more detailed diagnosis. Additional tests, such as amniocentesis and follow-up ultrasounds may be used to determine treatment options before the patient is born. Generally, severe CHD cases present and are detected at earlier stages of life, but minor defects may not become apparent until the patient is older. Tests used to diagnose CHD in post-natal patients include electro- and echo-cardiograms, chest x-rays, pulse oximetry, exercise stress tests, computed tomography or MRI scans, and cardiac catheterization. Treatment of

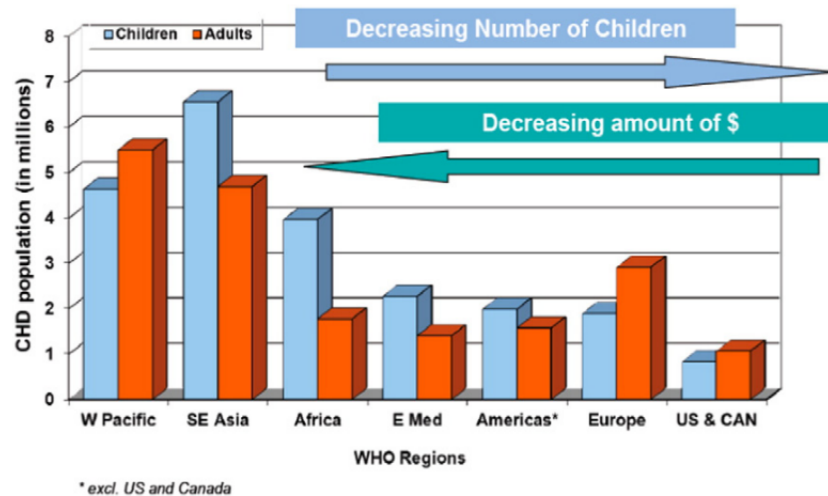


Figure 13: Estimated CHD burden in World Health Organization (WHO) regions using incidence rates of approximately 12/1000 and 4/1000 in children and adults, respectively (Webb et al., 2015).

different defects varies from monitoring and medication to surgery and cardiac implants.

The cost of diagnostic techniques and treatment plans impose different levels of financial burden on CHD patients and their families. Certain defects require complex, expensive surgical repairs while others can be treated with less expensive approaches (Mozaffarian et al., 2016). The burden of CHD across the globe was outlined by Webb et al (Webb et al., 2015). Their figure illustrating the prevalence of CHD and the availability of funds with which to treat it can be seen in Figure 13. As the overall mortality of CHD declines, the burden of CHD is expected to increase (Mozaffarian et al., 2016).

Unfortunately, the cost of treating CHD is not the only burden a patient must undergo. Patients with CHD are also at increased risk for heart failure and infections (Mozaffarian et al., 2016). Children with CHD are at 19-fold risk for stroke compared to their healthy counterparts (Fox et al., 2015). In a study of Swedish citizens born between 1970 and 1993, Giang et al compared the prevalence of cardiac conditions in patients with and without CHD (Giang et al., 2018). They found that patients who had a CHD diagnosis were at about eight

times higher risk for intracerebral hemorrhage and subarachnoid hemorrhage than their non-CHD counterparts. The CHD patients were also more likely to suffer from arrhythmia and heart failure.

However, cardiac conditions are not the only complications CHD must deal with. Many of these patients also suffer from neurocognitive disorders that co-occur with CHD. Early research in this area focuses on the neurodevelopmental status of neonatal patients pre- and post-surgical intervention. One theory was that some factor or factors in the surgical intervention caused brain injuries in the patients. This idea proved to be inaccurate when researchers began detecting neurological malformations *in utero*.

In a systematic review of available literature regarding prenatal and postnatal presurgical CHD cases and neurodevelopmental outcomes, Mebius et al. identify two theories about the causality of neurodevelopmental delays and CHD ([Mebius et al., 2017](#)). The first theory is that abnormalities in the cardiac system prevent the developing brain from receiving enough oxygen and nutrients, which disrupts prenatal brain development. The second theory is that faulty genetic pathways used during both cardiac and brain development cause both conditions to co-occur. However, 11 articles Mebius et al. found during their review that are related to bloodflow through the umbilical artery suggest a third theory. During the prenatal period, a fetus receives oxygen from the mother via the placenta. If the placenta was not functioning correctly, it could lead to the fetus receiving not enough oxygen. Lower quantities of oxygen throughout prenatal development could potentially cause problems both in brain and cardiac growth. The 11 articles have contradictory results, but some researchers are currently investigating the role of the placenta in CHD and prenatal brain development.

Survival of CHD patients to adulthood has increased from 10% to 90% over the last several decades as CHD diagnostic tools and treatments have improved. Currently, Webb et al. estimate that at least 12 to 34 million adults have CHD, and this number is expected to increase ([Webb et al., 2015](#)). The impact of the combination of CHD and neurological conditions throughout a patient's lifetime is starting to be explored. The aging of the CHD population has also sparked interest in the relationships between CHD and adult-stage neurological disorders such as dementia and Alzheimer's.

While the purpose of this study is not to focus on CHD patients, we chose to use CHD

and aging brain images in support of research being performed in the area of relationships between CHD and neurodevelopment.

5.2.2 Study Cohorts

The rs-fMRIs used in this study were gathered as part of ongoing studies of the relationship between CHD and neurodevelopment. Data from the CHD/neurodevelopment studies was obtained through studies approved by the IRB at the Children’s Hospital of Pittsburgh of UPMC and the University of Pittsburgh. All data is stored and accessed in compliance with HIPPA policies.

The subjects included in this analysis fall into three age groups: neonatal, preadolescent, and fetal. To summarize the cohorts, there were 124 brain rs-fMRIs obtained for the fetal cohort, 163 brain rs-fMRIs obtained for the neonatal cohort, and 546 brain rs-fMRIs obtained for the preadolescent cohort. The fetal cohort also contains 105 rs-fMRIs of the placenta. The race, ethnicity, and gender counts for these three cohorts can be seen in Figures 14, 15, and 16, respectively. The majority of subjects in each cohort were white and male. In the following sections, we describe each cohort in detail.

5.2.2.1 Fetal Subject Population and Images A fetal subject is scanned in vivo. He is suspended in amniotic fluid within his mother. The amniotic fluid has buoyancy that reduces the effects of gravity and allows a fetal subject significant freedom of movement. The fetus can rotate, shift, and flip in ways that can only be accomplished when floating in a body of water. The properties of the uterus constrain the physical space in which a motion could occur, but not as much as the head coil and gravity do to the other patient cohorts. A fetus is not guaranteed to be in any specific position at the start of the scan: the scan begins when the mother is ready, not when the fetus achieves a certain pose.

The fetal subjects underwent fetal echocardiography scans in a cardiac clinic to determine whether they were healthy or had a form of CHD. Images of the fetal brain and the placenta were obtained for each subject during MRI acquisitions.

The MRI scans are performed when the mother is in her third trimester. Due to the

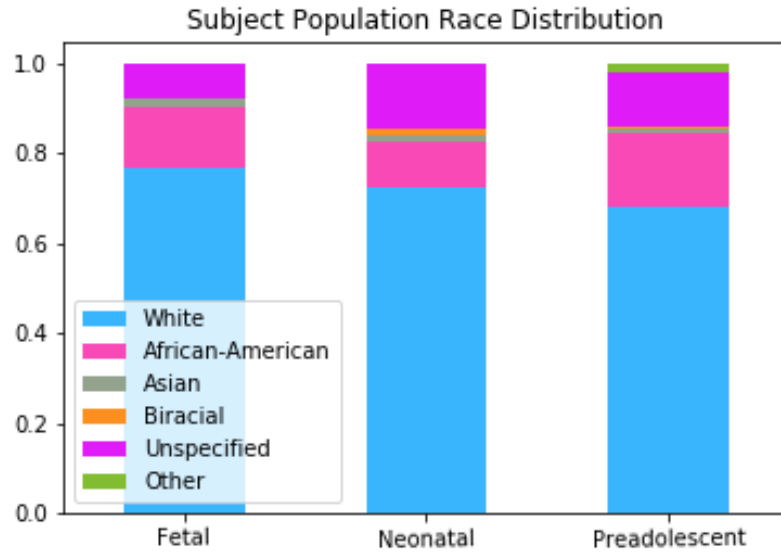


Figure 14: Distribution of subject races for all three cohorts.

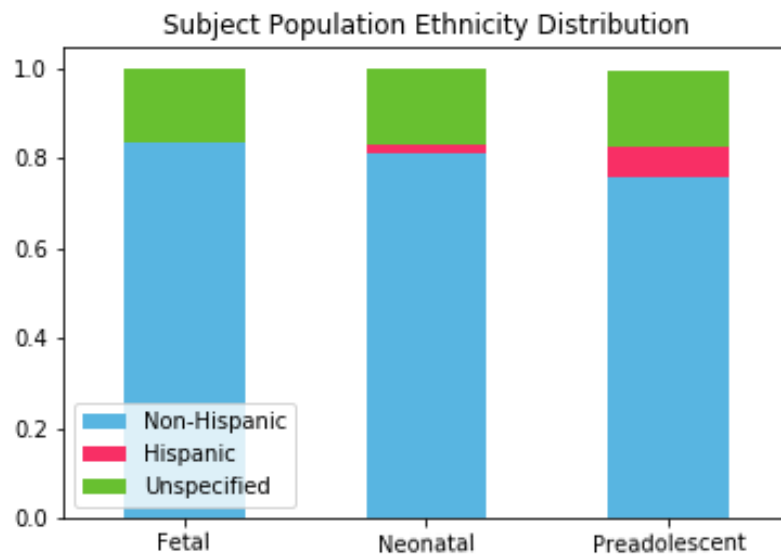


Figure 15: Distribution of subject ethnicities for all three cohorts.

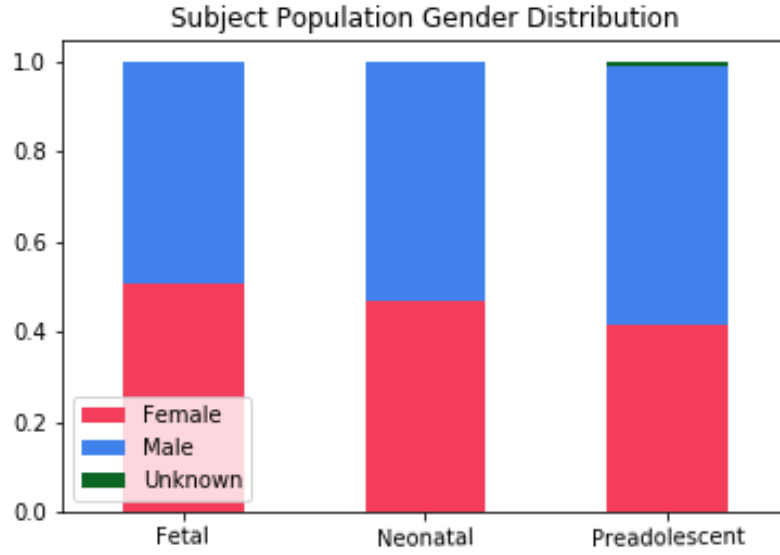


Figure 16: Distribution of subject genders for all three cohorts.

constraints of pregnancy, the mother cannot lay directly on her side or directly on her back. The MRI scans were performed with the mother going feet first into the scanner and laying on an angle on her left or right side (left or right anterior oblique). The side chosen is the mother’s preference. Her back is supported by a pillow to maintain her position during the scan. A large flexible coil is positioned on her abdomen to get coverage of the fetus and the placenta. The coil and pillow are secured with a strap. The mother is fitted with earplugs and headphones and given a button to use during the scan if she needs to get the attention of the radiology technician. No vital monitoring occurs as a part of the study.

A total of 124 fetal subjects were scanned on a 3T Skyra (Siemens AG, Erlangen, Germany). The subjects were between 23 and 39 weeks in post-conceptual age. The distribution of fetal post-conceptual age at the time of the scan can be seen in Figure 17. Axial rs-fMRI brain scans were acquired for all subjects and placental rs-fMRI scans were acquired for 105 subjects. The subjects were divided into CHD and control groups based on fetal examinations. Some subjects were moved to different groups after birth. A breakdown of these groups before and after birth can be seen in Figure 18.

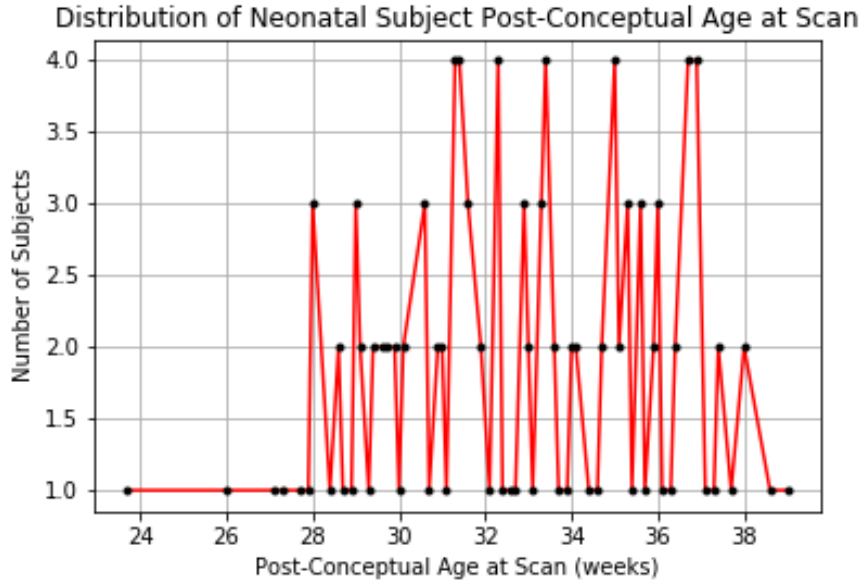


Figure 17: The distribution of post-conceptual ages at the time of the scan of all fetal subjects.

The parameters for the fetal rs-fMRI protocol were FOV = 300 mm and TE/TR = 32/2280 ms with interplane resolution of 4.7 x 4.7 mm, slice thickness of 3.0 mm and no gap between slices. The sequences were 150 volumes in length and each volume was composed of 32 slices containing 64 x 64 voxels. Each brain or placenta image underwent manual segmentation by one of a group of four researchers to remove non-brain or non-placental tissues respectively from the image.

We are interested in both the fetal brain and placental images for our work partially because of the relationship between placenta and brain development, but also because these organs have very different physical properties. The fetal brain is a rigid structure floating and moving within the amneotic fluid. It undergoes translation and rotation as a single unit due to passive and active maternal and fetal motions. The placenta, on the other hand, is anchored in place on the uterine wall. It may undergo small translations or rotations due to maternal motion, but it will respond differently to fetal motion. Fetal motions cause nonlinear deformations of the pliable placenta that can only be adequately accounted for

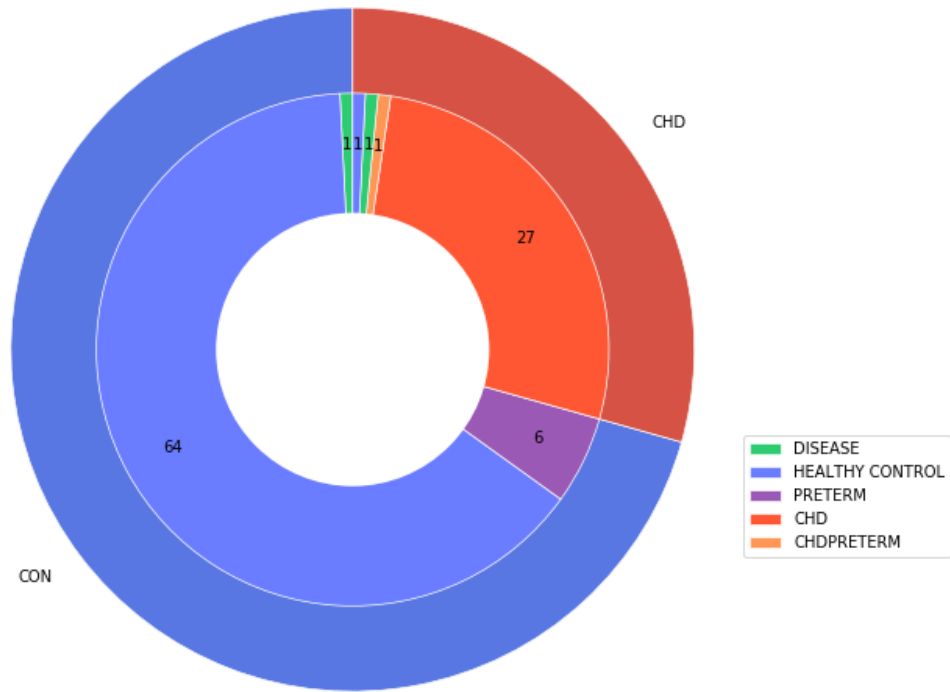


Figure 18: The outer ring represents the group the subject was assigned to based on the fetal examination while the inner ring represents the group the subject was assigned to after birth.

using nonlinear registration algorithms. Nonlinear registrations have the potential to deform brain images into physically impossible shapes, so the fetal brain and placenta were manually segmented in their respective images so that each organ could undergo independent motion correction. As the fetal subjects have both brain and placenta images, their data will be used to examine the impact of volume registration on different organ types.

5.2.2.2 Neonatal Subject Population and Images Neonatal subjects have been recruited as part of a prospective observational study. This cohort was scanned at two sites. At Site 1, the subjects were scanned using either a 3T Skyra (Siemens AG, Erlangen, Germany) or a 3T Signa (GE Healthcare, Chicago, Illinois, United States of America). At Site 2, the subjects were scanned using a 3T Achieva (Koninklijke Philips N.V., Amsterdam, Netherlands).

The subjects were unsedated during the scans and a “feed and bundle” protocol was used to prevent motion during the scans ([Windram et al., 2011](#)). The newborns were positioned in the coil to minimize head tilting. Newborns were fitted with earplugs (Quiet Earplugs; Sperian Hearing Protection, San Diego, CA) and neonatal ear muffs (MiniMuffs; Natus, San Carlos, CA). An MR-compatible vital signs monitoring system (Veris, MEDRAD, Inc. Indianola, PA) was used to monitor neonatal vital signs. All scans were performed using a multi-channel head coil. The parameters for the resting-state BOLD MR scans were FOV=240 mm and TE/TR=32/2020 ms with interplane resolution of 4x4 mm, slice thickness of 4 mm, and 4 mm space between slices. The acquired images contained 150 volumes where each volume consisted of 64x64x32 voxels³.

Scans from a total of 149 patients were included in this work. The average post-conceptual age of the patients at birth was 39.08 weeks and they were on average 42.64 weeks post-conception at the time of the scan. The distribution of post-conceptual ages of the subjects at birth and at the time of the scan can be seen in [Figure 19](#) and [Figure 20](#).

The subjects were a mix of control subjects and CHD subjects. A comprehensive breakdown description of the subgroups within these two cohorts can be seen in [Figure 21](#). In this figure, the term “Control” encompasses both healthy full-term subjects, healthy pre-term subjects, and non-CHD clinical subjects (clinical control and disease control). The CHD

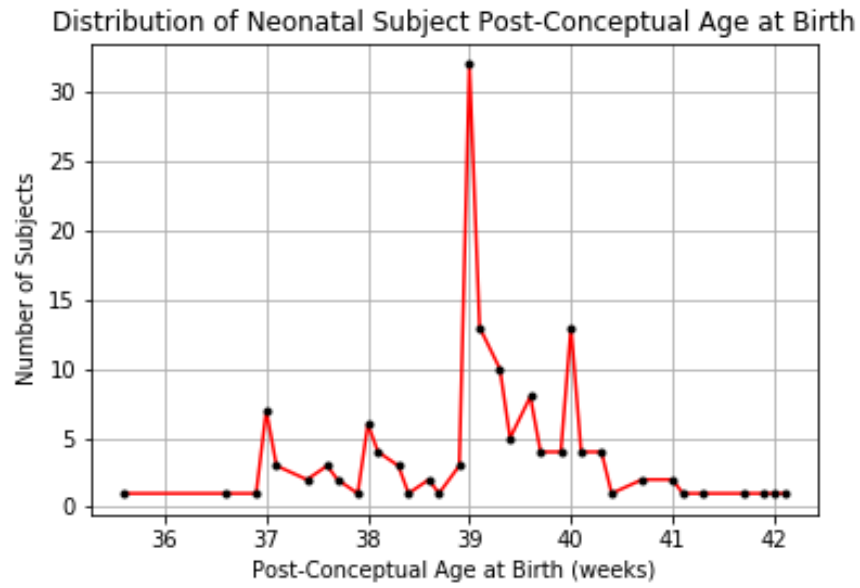


Figure 19: The distribution of post-conceptual ages at birth of all neonatal subjects.

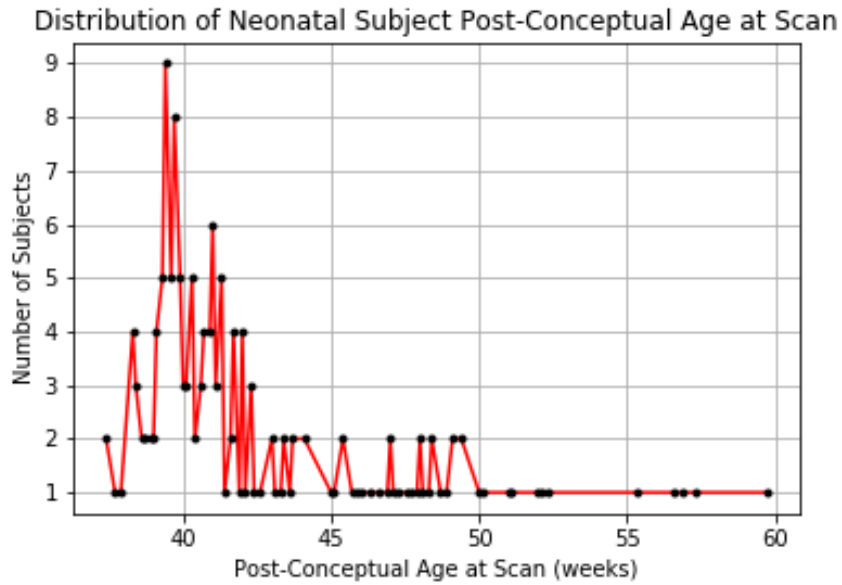


Figure 20: The distribution of post-conceptual ages at the time of the scan of all neonatal subjects.

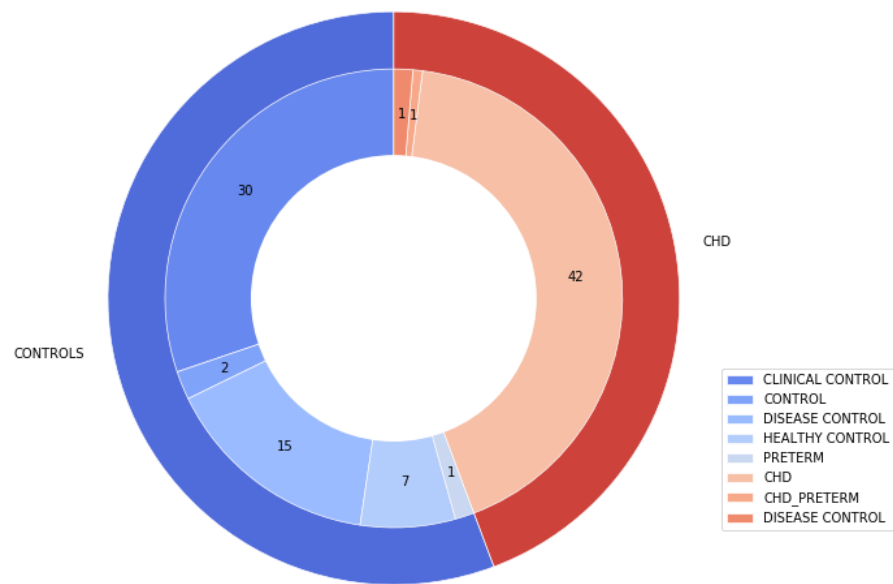


Figure 21: The breakdown of subject groups contained in the Control and CHD neonatal cohorts.

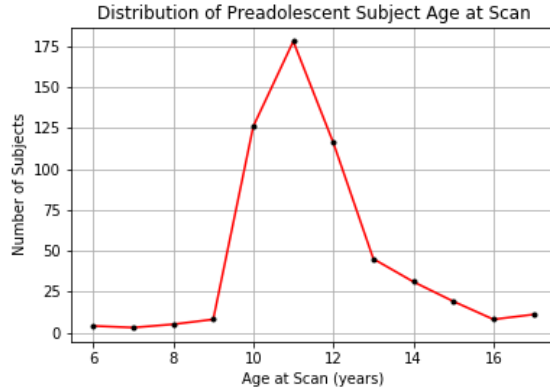


Figure 22: The distribution of preadolescent subject ages at the time of the scan.

group is composed of subjects diagnosed with CHD who were either born full-term or pre-term. Of the entire cohort, 14 subjects underwent two scanning sessions resulting in 163 rs-fMRI scans.

As the neonates were most often asleep during the scan, they exhibit less motion overall compared to our other clinical cohorts. The high-motion neonates are an obvious exception to this concept, but many of the high-motion images contained long periods where the subject was stationary. Applying both the DAG-based framework and the traditional registration framework to these images provided the opportunity to compare the performances of both registration frameworks to each other in the context of the usability gold standard thresholds.

5.2.2.3 Preadolescent Subject Population and Images As part of a multicenter study of CHD in preadolescents, rs-fMRIs have been collected from twelve sites throughout the United States. The two sites from the neonatal study in the previous section also participated in this study and retained their respective labels. The subjects enrolled in this study were patients in the age range of 6 to 17 years (average age: 11 years) who either had CHD or were healthy with no neurocognitive impairments. The histogram of patient ages at the time of each scan can be seen in Figure 23.

The majority of the subjects have CHD, though six sites also recruited healthy patients.

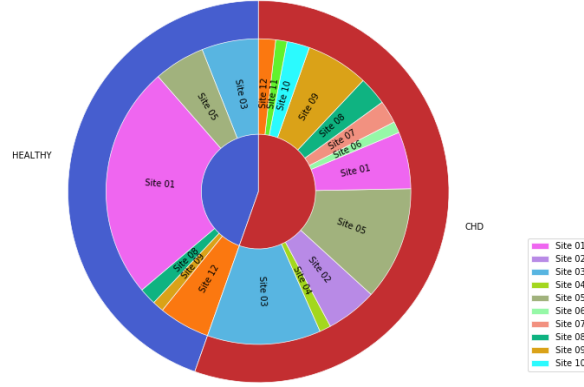


Figure 23: The distribution of CHD and healthy subjects between the 12 sites enrolled in the preadolescent study.

The distribution of CHD and healthy subjects between the 12 sites can be seen in Figure 22 and in more detail in Table 2.

The subjects underwent neurodevelopmental testing prior to the brain MRI scans. The neurodevelopment testing was scheduled to take between 4.5 and 5 hours. The subject is given breaks to reduce study fatigue. The MRI scans were scheduled to take 60 minutes assuming approximately 50 minutes of actual scan time and no repeat acquisitions.

As discussed earlier in this document, patient preparation and education before a scan can help reduce the amount of motion in the scan. The process used at Site 1 is partially dependent on the age of the preadolescent subjects. For younger subjects under the age of 8 years old, both the subject and the subject's family are asked whether they believe the subject could remain still for 45 minutes. The subject may also be shown the scanner to help determine his response. If the subject is comfortable being still for 45 minutes, the subject will undergo training with a mock scanner and scan will be scheduled. For subjects older than 8 years, the subject himself determines whether or not he will undergo a brain scan. He also determines if he would like to undergo training with the mock scanner prior to the scan. This process or similar processes may be used at the other sites in the study.

During the scan itself, the subject is provided with ear protection in the form of earplugs

Table 2: The number of CHD and healthy control preadolescent subjects scanned on each scanner type at each site.

Site	Scanner	Field Strength	CHD	HEALTHY
Site 01	Skyra	3T	22.0	128.0
Site 02	Unknown	Unknown	24.0	0.0
Site 03	Skyra	3T	83.0	44.0
Site 04	Unknown	Unknown	8.0	0.0
Site 05	Prisma	3T	23.0	12.0
Site 05	Skyra	3T	50.0	26.0
Site 06	Prisma	3T	6.0	0.0
Site 07	Trio	3T	14.0	0.0
Site 08	Prisma	3T	15.0	13.0
Site 09	Ingenia	3T	23.0	4.0
Site 10	Prisma	3T	14.0	0.0
Site 11	Skyra	3T	4.0	0.0
Site 12	Skyra	3T	11.0	32.0

and headphones. A stereotactic marker (vitamin capsule) is taped to the subject’s right temple. The patient’s head is positioned in a head coil so that his head and neck muscles are relaxed but not causing any head rotation. For comfort and lower body stabilization, his back or legs may be supported with an MR compatible pillow or foam pad. Additional pads or sponges may be used to stabilize and support the head. All subjects are positioned to that the centering crosshairs in the head coil are located at the subject’s nasion (between the eyebrows). The patient is given a squeeze ball alarm to use if he becomes distressed during the scan and is reminded to remain still during the scan.

At Site 1, the research coordinator performs verbal checks on the subjects between every or every other scanning protocol during the same acquisition period. During the rs-fMRI scan, a star is projected onto a screen outside the scanner. The screen is reflected into the subject’s line of sight via a mirror attached to the head coil. The subject is instructed to focus on the star during the rs-fMRI scan.

The parameters for the rs-fMRI scans were $FOV = 256$ mm and $TE/TR = 32/650$ ms with interplane resolution of 4.0×4.0 mm, slice thickness of 4.0 mm and no gap between slices. At the sites using Siemens scanners, the sequences were 470 volumes in length while the sites using Philips scanners had sequences with a length of 380 volumes. Each volume was composed of 36 slices containing 64×64 voxels.

The multicenter imaging study of preadolescent subjects provides a unique opportunity to evaluate the efficacy of the DAG-based framework on a large subject cohort containing variable amounts of motion.

5.3 SUMMARY

In this chapter, we discussed our two major data sets, a simulated data set and a clinical data set.

The simulated data were generated using a rs-fMRI simulation pipeline developed in-house and were used for the purpose of measuring ground truth signal recovered by motion correction techniques. An structural image from the ICBM Average Brain project and a set

of functional ROIs associated with resting state networks were used to generate the data. The data was given simulated scanner noise in the form of Gaussian noise injected into the k-space of the image. Finally, each image underwent rotation about the center of mass of the brain.

The pediatric data were obtained through prospective studies of CHD and neurodevelopment being conducted at the UPMC Children’s Hospital of Pittsburgh. CHD is a complex disease affecting millions of people globally. As the new treatments for CHD and its comorbidities have evolved, the life expectancy of patients with CHD has also increased.

Some of the comorbidities of CHD are related to a patient’s neurological development. As part of three studies of the relationship between CHD and brain development, rs-fMRI sequences of fetal, neonatal, and preadolescent brains have been gathered. A set of placental images were acquired alongside the fetal brain images. The pediatric images were used to compare the two volume registration techniques on a diverse set of clinical data. We also used these images to examine patterns of motion unique to different age groups.

In the next chapter, we examine the results of the registration methods and of the machine learning techniques applied to the motion metrics for the images.

6.0 RESULTS

This chapter is divided into two main sections. The first section focuses on the comparison of the two motion correction techniques. The second section focuses on the results of the machine learning algorithms applied to the metrics extracted from the images.

Each of the clinical images underwent volume registration using both registration methods outlined in Chapter 3. The FD and DVARs metrics were calculated for every pair of subsequent volumes i and $i + 1$ in the original sequences, the traditionally registered sequences, and the DAG-registered sequences. Then the sequences were comprehensively compared to themselves. For every volume in each sequence, the Dice metric, the mutual information, and the correlation ratio were calculated for the volume and every other volume in the sequence.

The simulated data underwent the same analyses as the clinical images, with one addition. Independent component analysis was performed on the simulated data to identify components contributing to the overall signal in the image. By correlating the components with the simulated signal for each image, the BOLD-related components were identified. The amount of BOLD signal identified for each image was compared to that image's original BOLD signal.

To keep this chapter readable, tables and figures for results that did not have significant value have been moved to Appendix B.

6.1 SIMULATED DATA

6.1.1 Volume Registration: Power Thresholds

The FD and DVARS metrics were calculated between every pair of image volumes $i - 1$ and i for the original sequences and both types of registered sequences. The mean and standard deviation of the FD and DVARS metrics for each time point for each sequence type can be seen in Figure 24. The mean of the FD metrics decreased from 2.45 mm in the original sequences to 1.07mm and 1.08 mm in the traditionally and DAG-registered sequences. The standard deviations of the FD slightly increased from 0.084 mm in the original sequences to 0.265 mm and 0.173 mm, respectively. Similarly, the mean DVARS of the original sequences decreased from 141.67 units to 107.30 units and 107.15 units in the registered images. The standard deviation of the DVARS also increased from 3.66 units in the original sequences to 4.77 units and 4.73 units in the registered sequences.

The FD and DVARS metrics for each image volume were compared to the usability criteria thresholds to determine the number of image volumes which were recovered by each registration type. The number of image volumes meeting the FD threshold, the DVARS threshold, and both thresholds were calculated. Table 3 shows the number of and percentage of image volumes which meet the specified thresholds. Across all 90 image sequences, there were 150 image volumes per sequence. The total number of image volumes for the simulated data was 13,410 image volumes. In the original images, less than 1% of the image volumes met the individual thresholds with only 0.395% of image volumes meeting both thresholds. After either registration, over 2% of the image volumes meet the FD threshold, though there was no significant change in the number of image volumes meeting the DVARS threshold.

To determine the statistical significance of the differences in the number of image volumes meeting each threshold, a series of independent 2 sample t-tests were performed. For each test, two types of sequences were chosen. The distributions of samples were the numbers of image volumes in each sequence meeting the usability threshold of interest. The null hypotheses for the t-tests were that the number of volumes meeting the threshold for each sequence type were the same and the alternative hypothesis was that this number was

different. The complete set of results can be seen in Table 14. The only statistically significant differences in usability counts were for the number of image volumes meeting the FD threshold. The numbers of registered image volumes meeting the FD threshold for both registration types were significantly different from the counts for the original image sequences at $p < 0.005$. The difference between the two registration types was not significant ($p = 0.127$).

The distributions of the FD and DVARS metrics underwent pairwise comparison via sequence type for each subject. The pairwise comparisons were performed using the Kolmogorov-Smirnov test. The Kolmogorov-Smirnov test evaluates the difference between a pair of probability distributions. The FD and DVARS distributions were significantly different between the original and traditionally registered sequences and the original and DAG-registered sequences at $p < 0.005$. Between the traditionally registered and DAG-registered sequences, 40 sequences (44.4%) had different FD distributions at $p < 0.05$ and 27 sequences (30.0%) had different FD at $p < 0.005$. The two types of registrations only had 3 sequences (3.33%) with different DVARS distributions at $p < 0.05$. This information can be found in table format in Tables 15 and 16.

Overall, the primary finding in the comparison of the registration techniques for the simulated data is the statistically significant decrease in FD by both registration types. There was also a decrease in the DVARS values for both registration types, but not a statistically significant one.

6.1.2 Volume Registration: Sequence Duration Motion

Motion across the whole sequence was measured by comparing every image volume in the sequence to every other image volume in the sequence. The three metrics used for this comparison were the correlation ratio, the Dice metric, and the mutual information metric. The calculations for a single metric on one sequence produced a two dimensional matrix of metric values.

These matrices were used to compare the quantities of motion over the course of an entire sequence. For a population level comparison, the minimum, first quartile, median, third quartile, and maximum values of each matrix were computed for each sequence. The

distribution of these values for sequences of one sequence type were compared to the distributions for a second sequence type using t-tests. The p-values that each metric comes from a different distribution can be seen in Table 17 for the correlation ratio matrices, Table 18 for the Dice matrices, and Table 19 for the MI matrices.

More generally, all matrix values for each sequence type were compared using the Kolmogorov-Smirnov test. The distributions for the correlation ratio metrics for the original, the traditionally registered, and the DAG-registered sequences differed at $p \leq 0.005$. The distributions for the Dice metrics and the mutual information metrics were also found to be from different distributions for each sequence type at $p \leq 0.005$.

Figures HMM show boxplots of the distributions of each metric over the three sequence types.

For the first analysis, the metrics matrices were compared to each other

To compare motion patterns, the metrics matrices were normalized for each subject.

The differences in the motion patterns embodied by the normalized matrices were different between the original, traditionally registered, and DAG-registered sequences for each simulated subject was significant at $p < 0.005$.

Use t-test to compare the normalized matrices for all simulated subjects across a single registration type. Plot a clustermap based on 2 coordinates and the distance (p-value) between them

6.1.3 Volume Registration: Recovered Signal

The average correlations between the best matching components and the DMN ROI were 8122.41 for the traditionally registered sequences and 8039.52 for the DAG-registered sequences. Neither the Kolmogorov-Smirnov test nor the t-test estimated a statistical significance between the correlation distributions between the best matching component and the DMN ROI for the registered sequences (KS p-value = 0.999; t-test p-value 0.807).

6.2 PREADOLESCENT COHORT

6.2.1 Volume Registration: Power Thresholds

The averages of the distributions of the FD and DVARS metrics across the whole time period of the sequences for the original, traditionally registered, and DAG-registered images were calculated. The images sequences varied in length from 150 volume to 450 volumes due to the differences in acquisition protocols at different sites. The means and standard deviations of FD and DVARS metrics for the entire set of sequence with their original lengths can be seen in Figures ?? and ?. The means and standard deviations of the FD and DVARS metrics for the first 150 volumes in each sequence can be seen in Figures ?? and ?.

To compare the FD and DVARS values for each type of motion correction, the metrics for each image were considered to be independent samples drawn from an unknown distribution. Pairwise comparisons of these distribution were performed using the Kolmogorov-Smirnov (KS) test. The two-sided KS test measures the distance between the empirical distributions of two distributions. The null hypothesis of the two-sided KS test is that the empirical distributions being compared come from the same underlying distribution. As the KS test is nonparametric, the metrics for all image volumes can be used.

By comparing the distributions for the original sequences to the distributions for the registered sequences, we aim to determine if the volume registration had a significant effect on the images themselves. The comparison of the distributions for the two types of registered images is intended to determine if there is a statistically significant difference between the FD and DVARS distributions of the registered images.

The KS statistic and p-value produced as result of the KS tests can be seen in Table ?? for the FD metrics and in Table ?? for the DVARS metrics.

The FD and DVARS values were compared to the usability thresholds defined by Power et al. to determine how many volumes were recovered by each framework (Power et al., 2014). Table ?? shows the number of volumes meeting each threshold, both in terms of the number of volumes in the cohort and the percentage of volumes in the cohort. In the original dataset, almost 42% of image volumes met both the FD and DVARS thresholds. However, only about

5% of volumes met both thresholds for each registration type. Looking at the thresholds independently, about 60% of volumes met the FD threshold before registration and only 16% of volumes met the threshold after registration. Similarly, about 48% of volumes met the DVARS threshold before registration and only about 6% of volumes met the threshold after registration. These results suggest that the registration process introduces some degree of error into the preadolescent images, at least with respect to the established usability criteria.

An example of the three similarity matrices can be seen in Figure 46. The element $e_{i,j}$ represents the value of the given metric between the image volumes represented by row i and column j . Each metric measures similarity according to slightly different definitions. In this figure, lighter values represent better metric values while darker values indicate lower similarity.

It is important to note the scales for these three metrics vary. The correlation ratio measures the distance between two items. Lower values for the correlation ratio means there is a smaller distance between the given pair of image volumes. The mutual information measures the shared information between two distributions of samples which may or may not be generated from the same underlying distribution. Higher mutual information values mean more shared information and low values mean less shared information. The Dice coefficient measures the overlap of two binary images. High Dice coefficients indicate a large amount of overlap, with a value of 1.0 indicating a perfect overlap.

The correlation ratio matrix in Figure 46 suggests that the patient remained relatively still for the first 300 volumes of the image, then moved for about 100 volumes, and remained still in a new position for the last 50 frames of the sequence. The colors representing the correlation ratios correspond to very low values, suggesting there is little patient motion overall.

The Dice coefficient matrix has a similar pattern as the mutual information matrix, but leads to a different conclusion. The Dice coefficient was calculated on an Otsu thresholded version of each image volume. As the values of the Dice coefficients are consistently high, the patient likely did not move much.

The mutual information matrix shows that the shared information throughout the entire image sequence varies. Using the information from the correlation ratio matrix and the Dice

coefficient matrix, it is possible that the variations in the mutual information matrix are due to changes in the rs-fMRI signal caused by BOLD signal changes, spin history effects of motion, and susceptibility effects of motion.

6.2.2 Volume Registration: Sequence Duration Motion

The distributions of the metrics matrices were compared to each other using the Kolmogorov-Smirnov test for each sequence type. The metrics for the Dice matrices and the mutual information matrices were determined to be from different distributions for each sequence type at $p \leq 0.005$.

6.3 NEONATAL COHORT

6.3.1 Volume Registration: Power Thresholds

Table 30 contains the number and percentages of image volumes from the whole neonatal cohort which meet the FD and DVARS thresholds. The total number of image volumes in across all sequences of a single type was 23704.

6.3.2 Volume Registration: Sequence Duration Motion

The distributions of the metrics matrices were compared to each other using the Kolmogorov-Smirnov test for each sequence type. The metrics for the Dice matrices and the mutual information matrices were determined to be from different distributions for each sequence type at $p \leq 0.005$.

6.4 FETAL COHORT

6.4.1 Brain

6.4.1.1 Volume Registration: Power Thresholds Table 38 contains the number and percentages of image volumes from the whole neonatal cohort which meet the FD and DVARS thresholds. The total number of image volumes in across all sequences of a single type was 12041.

6.4.1.2 Volume Registration: Sequence Duration Motion

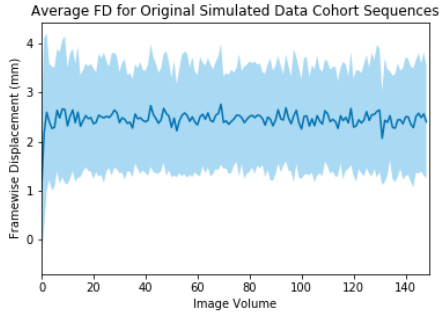
6.4.2 Placenta

6.4.2.1 Volume Registration: Power Thresholds Table 46 contains the number and percentages of image volumes from the whole neonatal cohort which meet the FD and DVARS thresholds. The total number of image volumes in across the original sequences was 10017, the traditionally registered images was 9296, and the DAG-registered images was 8896.

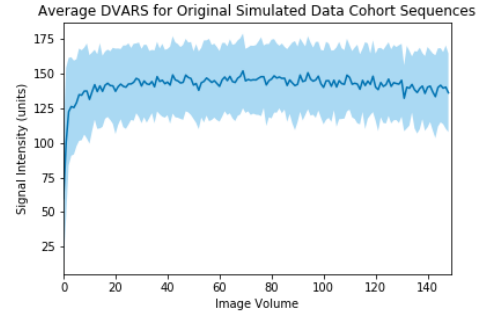
6.4.2.2 Volume Registration: Sequence Duration Motion

6.5 CHARACTERIZING MOTION

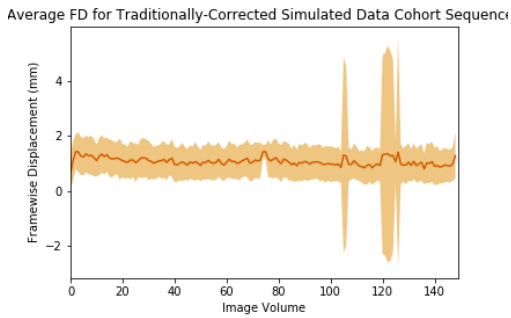
6.5.1 Age Groups



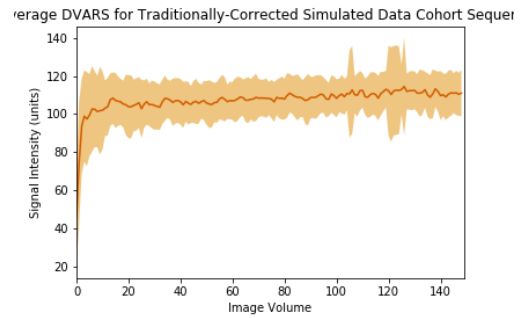
(a) FD of Original Sequences.



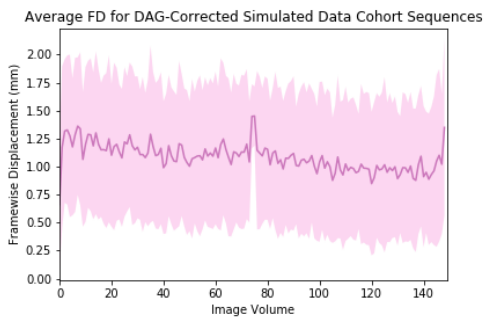
(b) DVARS of Original Sequences.



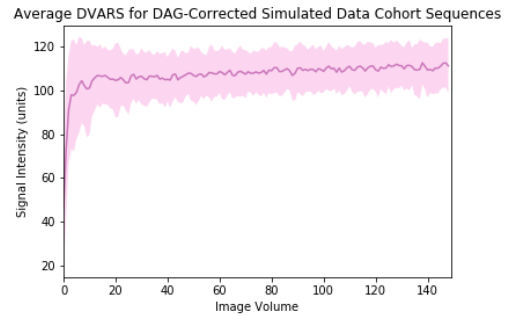
(c) FD of Traditionally Registered Sequences.



(d) DVARS of Traditionally Registered Sequences.



(e) FD of DAG-Registered Sequences.



(f) DVARS of DAG-Registered Sequences.

Figure 24: The means and standard deviations of the FD and DVARS metrics for all simulated images both before and after registration.

Table 3: The number and percentage of image volumes across all sequences in the simulated cohort which meet the usability thresholds of $FD < 0.2$ mm and $DVARS < 2.5\%$.

Threshold Met	Original Sequences	Traditionally Registered Sequences	DAG-Registered Sequences
FD (count)	98	329	279
DVARS (count)	54	53	53
Both (count)	53	46	44
FD (%)	0.731	2.453	2.081
DVARS(%)	0.403	0.395	0.395
Both (%)	0.395	0.343	0.328

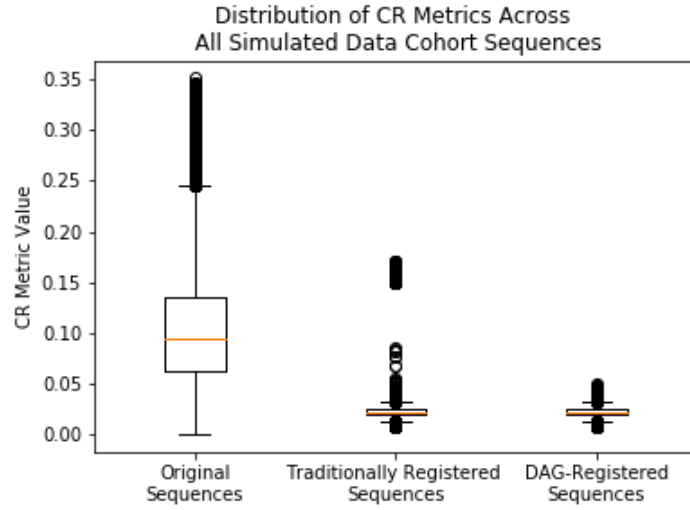


Figure 25: Boxplots of the values of all CR matrices for the original sequences, the traditionally registered sequences, and the DAG-registered sequences for the simulated data.

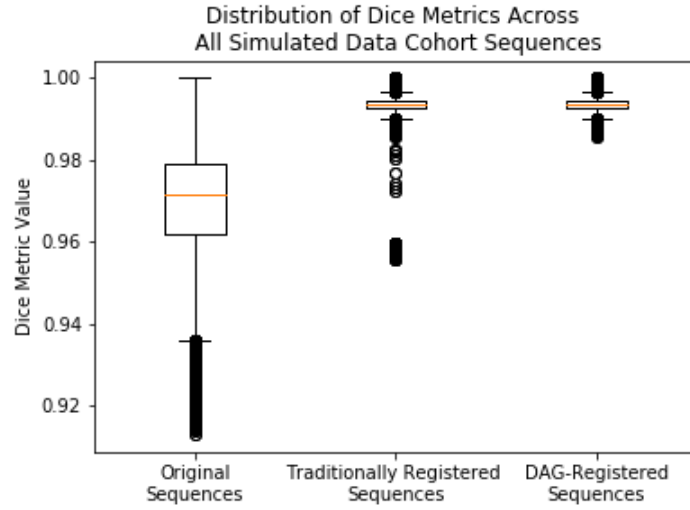


Figure 26: Boxplots of the values of all Dice matrices for the original sequences, the traditionally registered sequences, and the DAG-registered sequences for the simulated data.

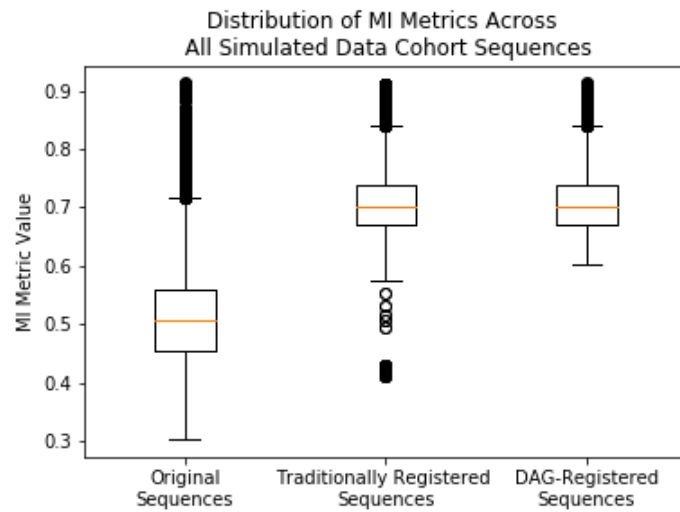


Figure 27: Boxplots of the values of all MI matrices for the original sequences, the traditionally registered sequences, and the DAG-registered sequences for the simulated data.

Table 4: The average true and false rates for both positive and negative voxels when comparing the IC component with the largest correlation to the DMN ROI over each simulated image.

Average Value	Traditionally Registered	DAG-Registered
TPR	0.587	0.623
FPR	0.104	0.00996
TNR	0.990	0.990
FNR	0.413	0.377

Table 5: The p-values determining whether the true and false rates for both positive and negative voxels differ between the traditionally registered and DAG-registered simulated sequences as calculated using the two-sided t-test.

Rate	2 Sided t-test p-value
TPR	0.441
FPR	0.729
TNR	0.729
FNR	0.441

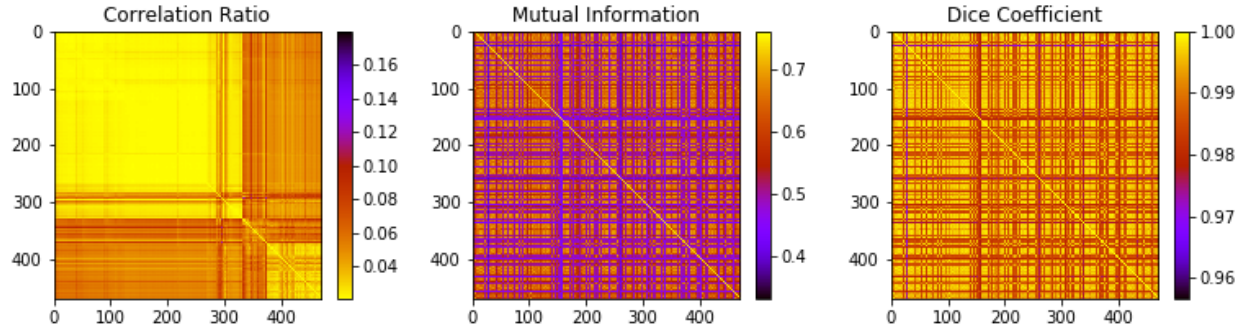


Figure 28: Examples of the three similarity matrices. Lighter colors represent more desirable values.

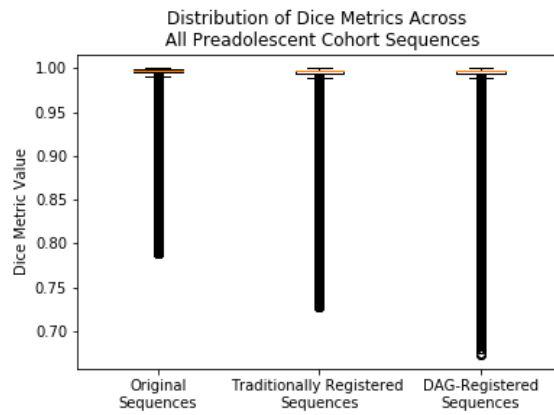


Figure 29: Boxplots of the values of all Dice matrices for the original sequences, the traditionally registered sequences, and the DAG-registered sequences for the preadolescent cohort.

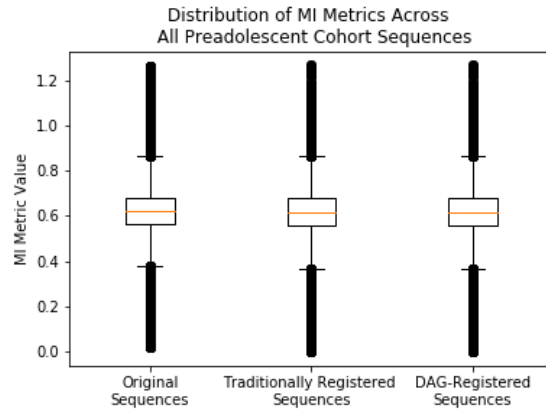


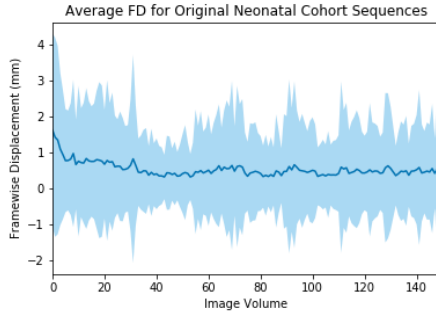
Figure 30: Boxplots of the values of all MI matrices for the original sequences, the traditionally registered sequences, and the DAG-registered sequences for the preadolescent cohort.

Table 6: The number of preadolescent subjects whose sequences of types S_1 and S_2 had different MI distributions.

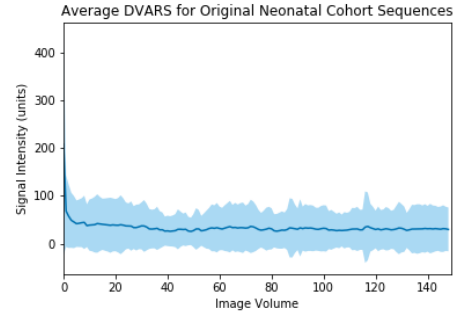
# Sequences Type 1 (S_1)	# Sequences Type 2 (S_2)	# Sequences $p < 0.05$	# Sequences $p < 0.005$
Original	Traditionally Registered	189	187
Original	DAG Registered	189	185
Traditionally Registered	DAG Registered	84	69

Table 7: The number of preadolescent subjects whose sequences of types S_1 and S_2 had different Dice distributions.

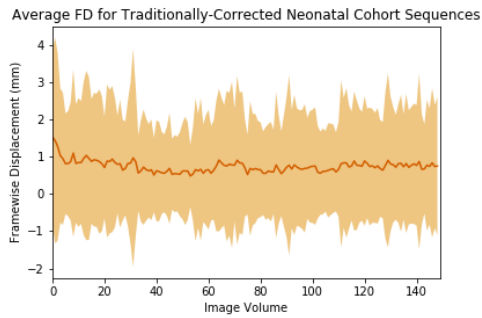
# Sequences Type 1 (S_1)	# Sequences Type 2 (S_2)	# Sequences $p < 0.05$	# Sequences $p < 0.005$
Original	Traditionally Registered	188	185
Original	DAG Registered	187	185
Traditionally Registered	DAG Registered	83	75



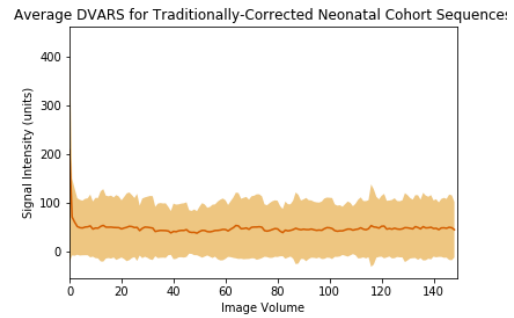
(a) FD of Original Sequences.



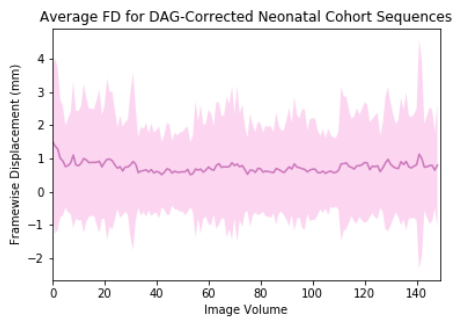
(b) DVARS of Original Sequences.



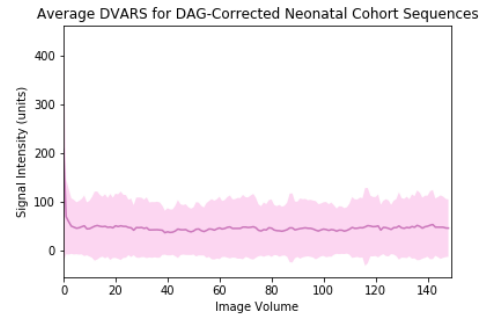
(c) FD of Traditionally Registered Sequences.



(d) DVARS of Traditionally Registered Sequences.



(e) FD of DAG-Registered Sequences.



(f) DVARS of DAG-Registered Sequences.

Figure 31: The means and standard deviations of the FD and DVARS metrics for all neonatal images both before and after registration.

Table 8: The number and percentage of image volumes across all sequences in the neonatal cohort which meet the usability thresholds of $FD < 0.2$ mm and $DVARS < 2.5\%$.

Threshold Met	Original Sequences	Traditionally Registered Sequences	DAG-Registered Sequences
FD (count)	16495	14264	14173
DVARS (count)	16820	13903	13752
Both (count)	15332	12837	12684
FD (%)	69.59	60.18	59.79
DVARS(%)	70.96	58.65	58.02
Both (%)	64.68	54.16	53.51

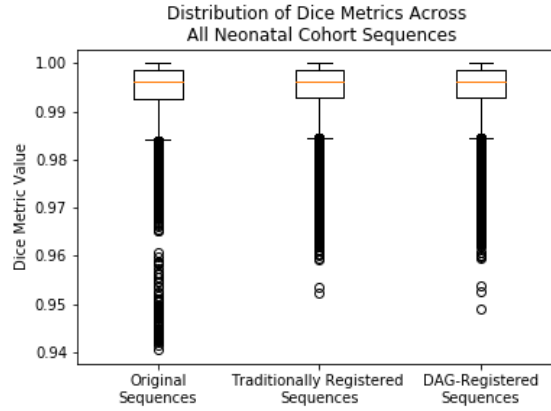


Figure 32: Boxplots of the values of all Dice matrices for the original sequences, the traditionally registered sequences, and the DAG-registered sequences for the neonatal cohort.

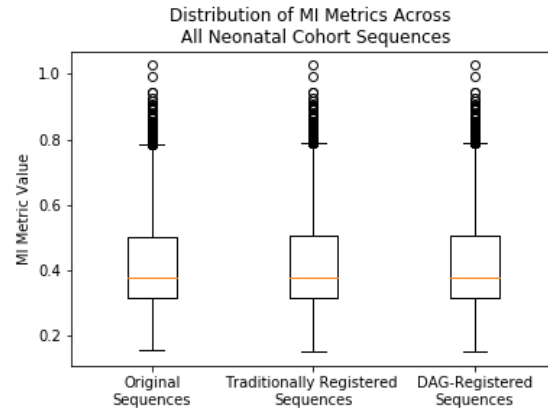


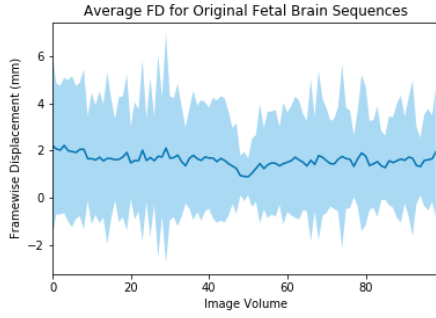
Figure 33: Boxplots of the values of all MI matrices for the original sequences, the traditionally registered sequences, and the DAG-registered sequences for the neonatal cohort.

Table 9: The number of neonatal subjects whose sequences of types S_1 and S_2 had different MI distributions.

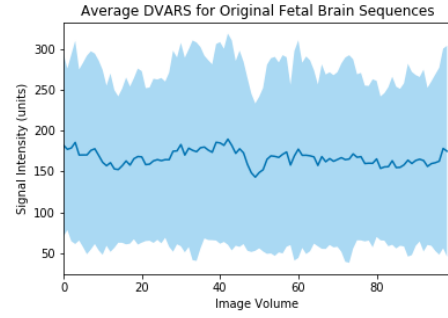
# Sequences Type 1 (S_1)	# Sequences Type 2 (S_2)	# Sequences $p < 0.05$	# Sequences $p < 0.005$
Original	Traditionally Registered	66	64
Original	DAG Registered	71	69
Traditionally Registered	DAG Registered	64	64

Table 10: The number of neonatal subjects whose sequences of types S_1 and S_2 had different Dice distributions.

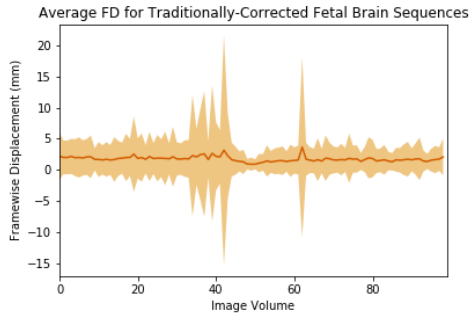
# Sequences Type 1 (S_1)	# Sequences Type 2 (S_2)	# Sequences $p < 0.05$	# Sequences $p < 0.005$
Original	Traditionally Registered	67	66
Original	DAG Registered	71	69
Traditionally Registered	DAG Registered	68	64



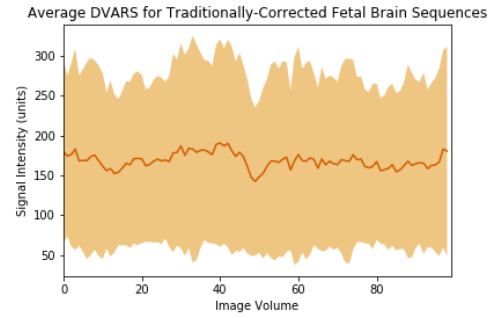
(a) FD of Original Sequences.



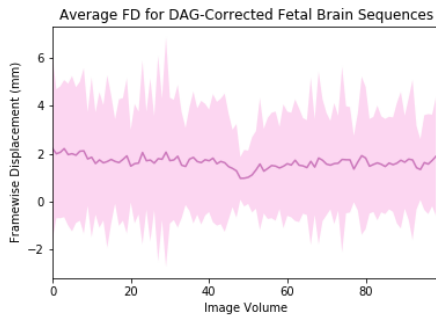
(b) DVARS of Original Sequences.



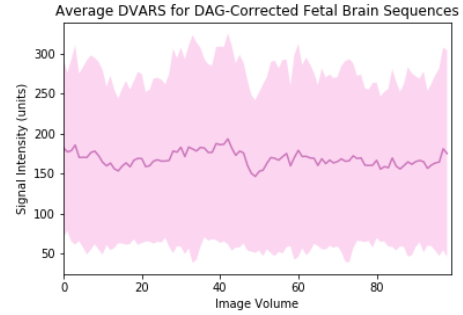
(c) FD of Traditionally Registered Sequences.



(d) DVARS of Traditionally Registered Sequences.



(e) FD of DAG-Registered Sequences.



(f) DVARS of DAG-Registered Sequences.

Figure 34: The means and standard deviations of the FD and DVARS metrics for all fetal brain images both before and after registration.

Table 11: The number and percentage of image volumes across all sequences in the fetal brain image data set which meet the usability thresholds of $FD < 0.2$ mm and $DVARS < 2.5\%$.

Threshold Met	Original Sequences	Traditionally Registered Sequences	DAG-Registered Sequences
FD (count)	575	581	561
DVARS (count)	7	84	7
Both (count)	7	80	7
FD (%)	4.775	4.854	4.659
DVARS(%)	0.058	0.702	0.058
Both (%)	0.058	0.668	0.058

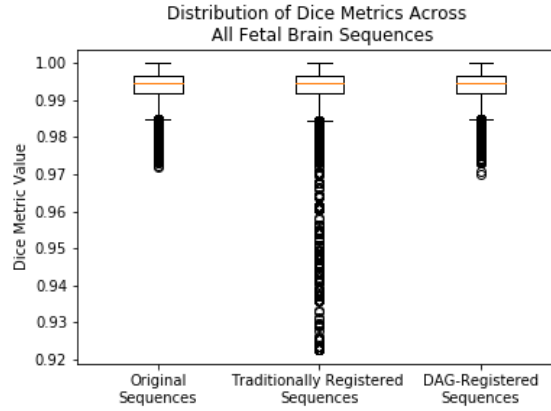


Figure 35: Boxplots of the values of all Dice matrices for the original sequences, the traditionally registered sequences, and the DAG-registered sequences for the fetal-brain images.

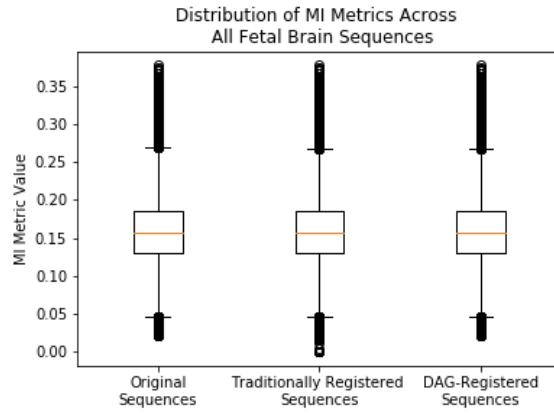
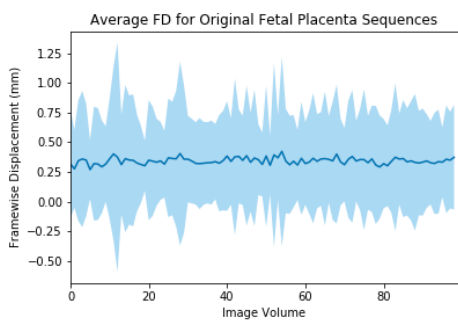


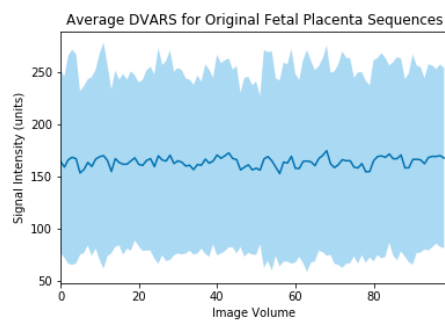
Figure 36: Boxplots of the values of all MI matrices for the original sequences, the traditionally registered sequences, and the DAG-registered sequences for the fetal brain images.

Table 12: The number of subjects whose sequences of types S_1 and S_2 had different MI distributions.

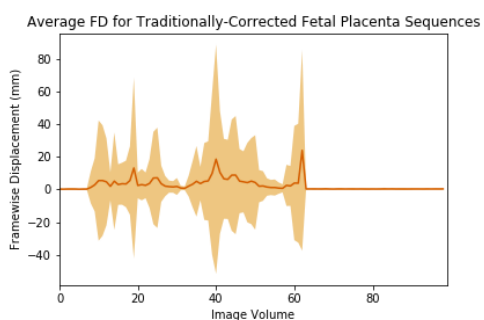
# Sequences Type 1 (S_1)	# Sequences Type 2 (S_2)	# Sequences $p < 0.05$	# Sequences $p < 0.005$
Original	Traditionally Registered	13	10
Original	DAG Registered	12	9
Traditionally Registered	DAG Registered	14	9



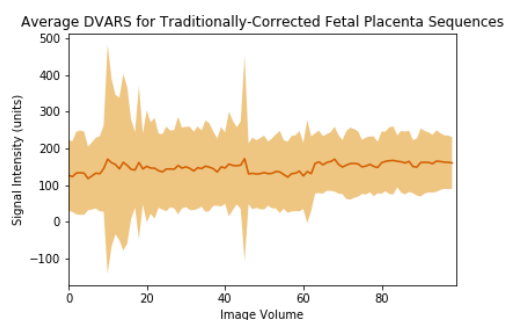
(a) FD of Original Sequences.



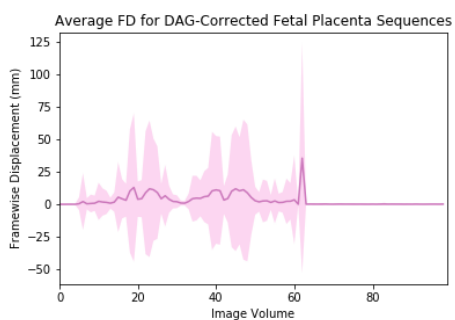
(b) DVARS of Original Sequences.



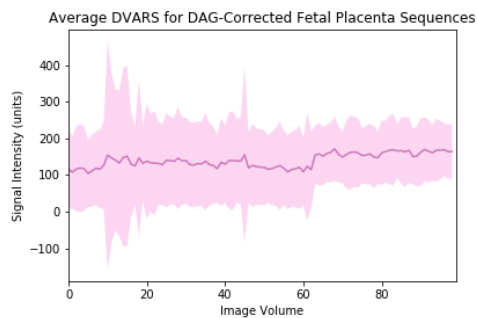
(c) FD of Traditionally Registered Sequences.



(d) DVARS of Traditionally Registered Sequences.



(e) FD of DAG-Registered Sequences.



(f) DVARS of DAG-Registered Sequences.

Figure 37: The means and standard deviations of the FD and DVARS metrics for all placenta images both before and after registration.

Table 13: The number and percentage of image volumes across all sequences in the fetal placenta image data set which meet the usability thresholds of FD <0.2 mm and DVARs $<2.5\%$.

Threshold Met	Original Sequences	Traditionally Registered Sequences	DAG-Registered Sequences
FD (count)	10017	4113	4005
DVARs (count)	17	1056	1624
Both (count)	17	599	996
FD (%)	43.646	44.245	45.020
DVARs(%)	0.170	11.36	18.255
Both (%)	0.170	6.444	11.196

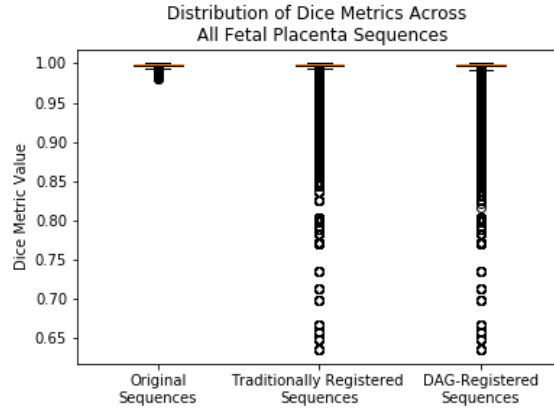


Figure 38: Boxplots of the values of all Dice matrices for the original sequences, the traditionally registered sequences, and the DAG-registered sequences for the placenta images.

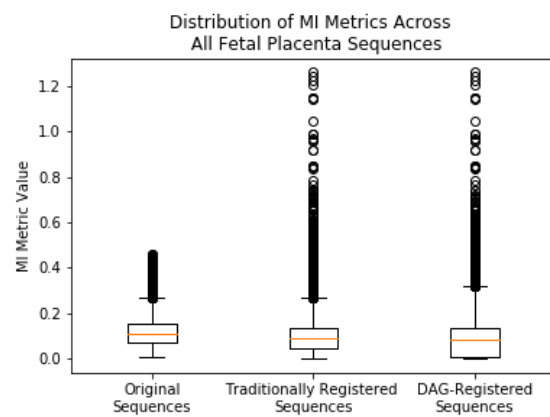


Figure 39: Boxplots of the values of all MI matrices for the original sequences, the traditionally registered sequences, and the DAG-registered sequences for the placenta images.

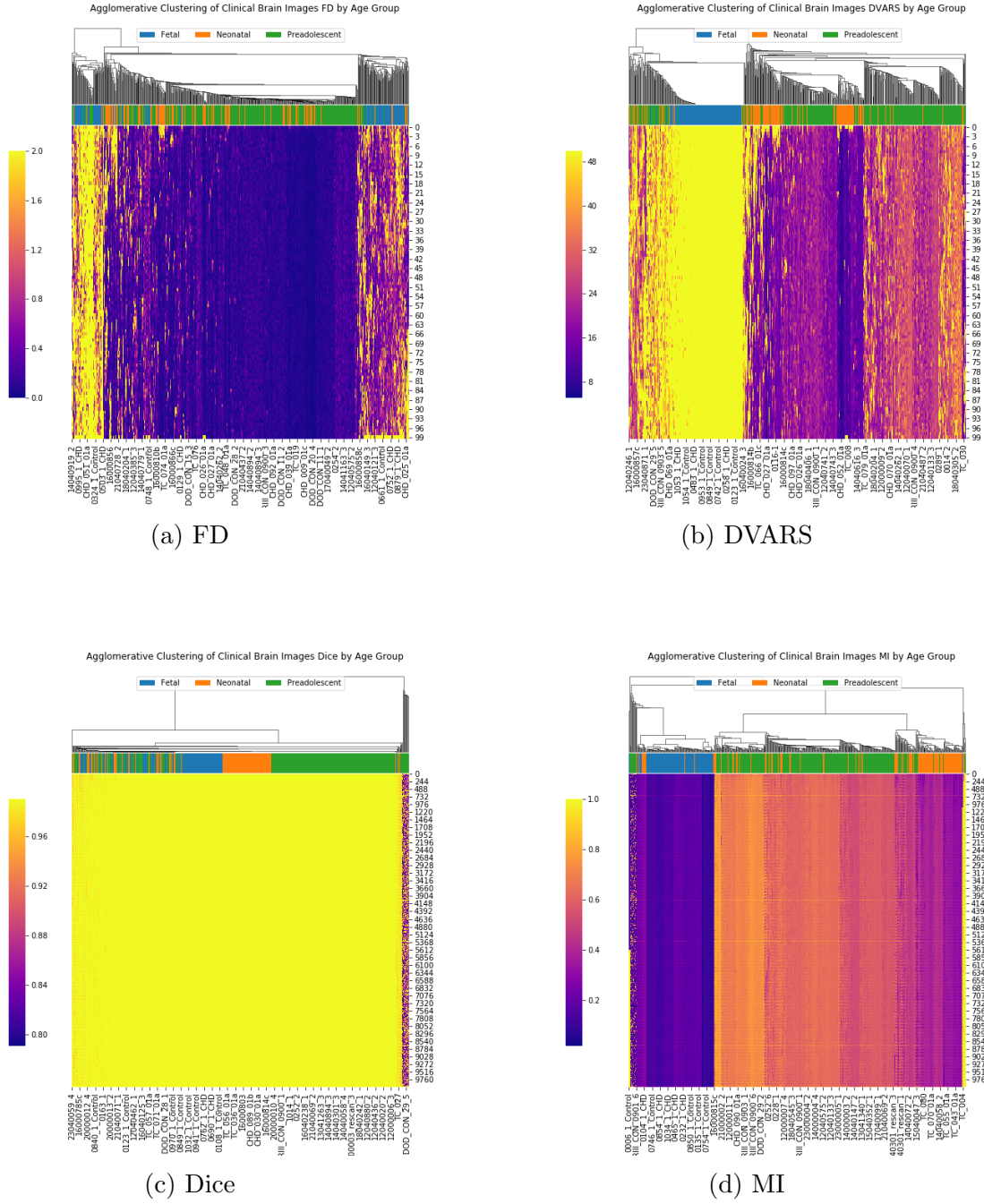


Figure 40: The preadolescent, neonatal, and fetal images clustered by each metric using agglomerative clustering and labeled by age group.

6.5.2 CHD and Control

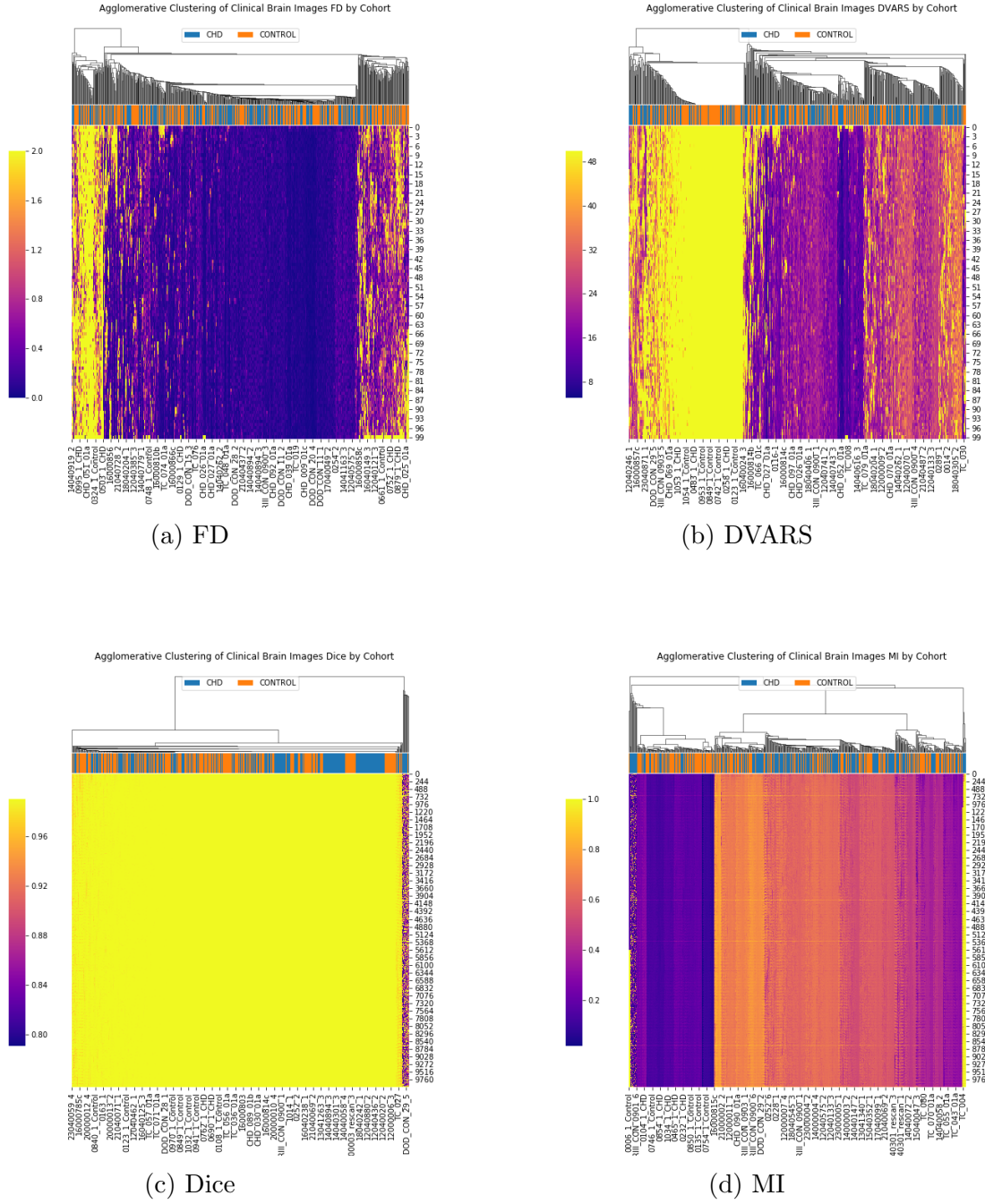


Figure 41: The preadolescent, neonatal, and fetal images clustered by each metric using agglomerative clustering and labeled by CHD/Control status.

7.0 DISCUSSION

7.1 COHORT-LEVEL ANALYSIS

Resting-state BOLD MR images are used to evaluate the functional architecture of a patient’s brain. Because resting-state BOLD images are highly susceptible to motion, development of strong post-acquisition motion correction techniques is vital. Current pipelines for mitigating motion after sequence acquisition vary in terms of efficacy and effectiveness, but all begin with global volume registration. In this study, we compared the corrective performance of two global volume registration methods, the traditional framework and a novel DAG-based framework, on a set of 17 neonatal rs-fMRIs.

The correlation ratio matrices, FD, and DVARS values were calculated for each sequence. The decrease in the mean and standard deviations of the correlation ratio matrices for the registered sequences indicate that global volume registration reduces some effects of motion in rs-fMRIs. The histograms of the FD and DVARS values in the registered sequences show that the DAG-based method was better able to correct volumes to meet Power et al’s thresholds than the traditional registration method. These results indicate that the DAG-based global registration method is better able to reduce the effects of motion than the traditional global registration method when correcting motion in neonatal images. While no entire sequences were recovered, some high-motion volumes within each sequence were recovered by the DAG-based registration method that were not recovered by the traditional registration method.

7.1.1 Simulated Cohort

7.1.2 Preadolescent Cohort

7.1.3 Neonatal Cohort

7.1.4 Fetal Cohort

The fetal scans were manually segmented, the masks used in the segmentation were created to be uniform across the whole sequence. The intention behind this process is to remove all voxel values not associated with the organ of interest. However, fetal motion is highly variable. It is possible for a subject to rotate in any direction. The subject may drastically change position in the middle of the scan, possibly several times. The manually created masks were developed using a software tool which allows 3D image masks to be applied to an entire 4D image sequence. The masks were required to be created to ensure the fetal brain or placenta would be inside the masked area at all times. The masks may cover some area that does not belong to the organ of interest.

This limitation is unique to the fetal images. Existing pre-processing pipelines exist for skull stripping for neonatal and preadolescent images. Development of a similar pipeline for fetal images, while a challenge, would make research surrounding fetal rs-fMRIs more accessible to the medical imaging community.

Alternatively, the field of computer vision offers some SOMETHING.

7.2 LIFESPAN ANALYSIS

Registration fixes positional effects of motion, not spin history or susceptibility effects Subject motion during rs-MRI scans affects both the recorded position and orientation of the subject as well as the established magnetic spin gradients within the skull. The DAG-based technique can correct the positional effects of motion, but it cannot correct the effects of the motion that disrupt the magnetic spin gradients. Methods for prospectively estimating subject motion exist and can be used to change slice positions in each volume

during acquisition. Retrospective techniques to correct for this effect will require shot-to-shot modeling of macroscopic B_0 fields and are beyond the scope of the present research.

7.3 RELATION TO EXISTING WORK

To the best of our knowledge, the only other study that has used a variant of the DAG-based method was performed by Liao et al ([Liao et al., 2016](#)). Liao et al.s dataset consisted of 10 fetal rs-fMRIs. In each of these sequences, the fetal brain, fetal liver, and placenta were manually segmented in the first volume of the sequence as well as in five other randomly chosen volumes. These overlap of these manual segmentations before and after registration as measured using the Dice coefficient was used to quantify the amount of motion in each sequence. Even though the Dice coefficients increase more in each sequence after Liao et al.s registration than after traditional registration, their measure of positional change fails to quantify any changes in position between any other pairs of volumes that do not have manual segmentations.

Satterthwaite et al. note that motion is often correlated with patient age in adolescent populations and specifically designed a study of adolescents ages 8-23 such that patient age and motion were uncorrelated (Satterthwaite 2012a?).

8.0 CONCLUSIONS

This is the second chapter of the present dissertation. It is more interesting than the first one, for it is the last one.

8.1 LIMITATIONS

8.2 FUTURE WORK

8.2.1 Adult Subject Population and Images

As the prognosis for patients with CHD improves, their life expectancy also increases. The aging CHD population presents new questions about the connection between CHD and neurocognitive challenges associated with aging. As patients age, there is an expectation that their images will contain less motion for a time. If a patient begins to show signs of cognitive impairment due to aging, it can be expected that their images will begin to contain more motion as their neurocognitive state deteriorates.

We include a cohort of adult subjects over a wide range of ages in our study. The purpose of using images from this cohort is to demonstrate the generalizability of the DAG-based framework to adult patients as well as its use in different clinical populations. This cohort is being studied as part of an ongoing, prospective study of CHD and neurodevelopment. The data collected for these subject includes rs-fMRIs, behavioral, and clinical data from healthy and CHD adult subjects.

APPENDIX A

VOLUME REGISTRATION PARAMETERS

The parameters used for the registration of pairs of image volumes can be seen below.

```
##
# Register a pair of image volumes
#
# Effects: save a copy of the registered image and the registration
#         ↪ parameters
#
# @param fixedImgFn The filename of the fixed image as a string
# @param movinImgFn The filename of the moving image as a string
# @param regImgOutFn The filename as a string specifying where to save the
#                   ↪ registered moving image
# @param transformPrefix
# @param initialize Optional parameter to specify the location of the
#                   ↪ transform matrix from the previous registration
# @param regType Optional parameter to specify the type of registration to
#                 ↪ use (affine ['Affine'] or nonlinear ['Syn']) Default: nonlinear
def registerVolumes(fixedImgFn, movinImgFn, regImgOutFn, transformPrefix,
#                 ↪ initialize=None, regtype='nonlinear'):
```

```

# Registration set up: for both Affine and SyN transforms
reg = Registration()
reg.inputs.fixed_image = fixedImgFn
reg.inputs.moving_image = movinImgFn
reg.inputs.output_transform_prefix = transformPrefix
reg.inputs.interpolation = 'NearestNeighbor'
reg.inputs.dimension = 3
reg.inputs.write_composite_transform = False
reg.inputs.collapse_output_transforms = False
reg.inputs.initialize_transforms_per_stage = False
reg.inputs.num_threads = 100
reg.inputs.output_warped_image = regImgOutFn

# Registration set up: Specify certain parameters for the Affine
    ↪ registration step
reg.inputs.transforms = ['Affine']
reg.inputs.transform_parameters = [(2.0,)]
reg.inputs.number_of_iterations = [[1500, 200]]
reg.inputs.metric = ['CC']
reg.inputs.metric_weight = [1]
reg.inputs.radius_or_number_of_bins = [5]
reg.inputs.convergence_threshold = [1.e-8]
reg.inputs.convergence_window_size = [20]
reg.inputs.smoothing_sigmas = [[1,0]]
reg.inputs.sigma_units = ['vox']
reg.inputs.shrink_factors = [[2,1]]
reg.inputs.use_estimate_learning_rate_once = [True]
reg.inputs.use_histogram_matching = [True] # This is the default, but
    ↪ specify it anyway

```



```

# Registration set up: nonlinear transforms only
if regtype == 'nonlinear':
    reg.inputs.transforms.append('SyN')
    reg.inputs.transform_parameters.append((0.25, 3.0, 0.0))
    reg.inputs.number_of_iterations.append([100, 50, 30])
    reg.inputs.metric.append('CC')
    reg.inputs.metric_weight.append(1)
    reg.inputs.radius_or_number_of_bins.append(5)
    reg.inputs.convergence_threshold.append(1.e-9)
    reg.inputs.convergence_window_size.append(20)
    reg.inputs.smoothing_sigmas.append([2,1,0])
    reg.inputs.sigma_units.append('vox')
    reg.inputs.shrink_factors.append([3,2,1])
    reg.inputs.use_estimate_learning_rate_once.append(True)
    reg.inputs.use_histogram_matching.append(True) # This is the default
    ↪ value, but specify it anyway

# If the registration is initialized, set a few more parameters
if initialize is not None:
    reg.inputs.initial_moving_transform = initialize
    reg.inputs.invert_initial_moving_transform = False

# Keep the user updated with the status of the registration
print("Starting", regtype, "registration_for", regImgOutFn)

# Run the registration
reg.run()

# Keep the user updated with the status of the registration
print("Finished", regtype, "registration_for", regImgOutFn)

```

APPENDIX B

COMPREHENSIVE SELECTION OF RESULTS TABLES AND FIGURES

B.1 SIMULATED DATA

B.1.1 Volume Registration: Power Thresholds

Table 14: Results from the t-tests comparing the counts for the numbers of images meeting the FD, DVARs, and FD and DVARs thresholds for sequence type S_1 and sequence type S_2 .

Sequence Type 1 (S_1)	Original	Original	Traditionally Registered
Sequence Type 2 (S_2)	Traditionally Registered	DAG Registered	DAG Registered
P(S_1 and S_2 have same FD counts)	1.05 E -16	4.49 E -11	0.127
P(S_1 and S_2 have same DVARs counts)	0.941	0.941	1.0
P(S_1 and S_2 have same FD and DVARs counts)	0.590	0.486	0.872

Table 15: The number of subjects whose sequences of types S_1 and S_2 had different FD distributions.

# Sequences Type 1 (S_1)	# Sequences Type 2 (S_2)	# Sequences $p < 0.05$	# Sequences $p < 0.005$
Original	Traditionally Registered	90	90
Original	DAG Registered	90	90
Traditionally Registered	DAG Registered	40	27

Table 16: The number of subjects whose sequences of types S_1 and S_2 had different DVARS distributions.

# Sequences Type 1 (S_1)	# Sequences Type 2 (S_2)	# Sequences $p < 0.05$	# Sequences $p < 0.005$
Original	Traditionally Registered	90	90
Original	DAG Registered	90	90
Traditionally Registered	DAG Registered	3	0

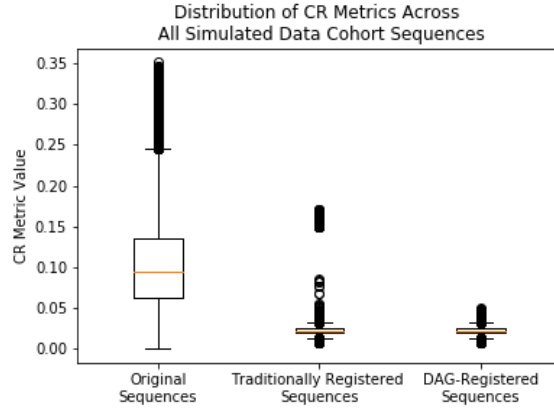


Figure 42: Boxplots of the values of all CR matrices for the original sequences, the traditionally registered sequences, and the DAG-registered sequences for the simulated data.

B.1.2 Volume Registration: Sequence Duration Motion

Table 17: Results of t-tests comparing the descriptive statistics of the correlation ratio matrices for the simulated data.

Sequence Type 1 (S_1)	Original	Original	Traditionally Registered
Sequence Type 2 (S_2)	Traditionally Registered	DAG Registered	DAG Registered
P(S_1 and S_2 have same minimums)	0.3487	0.3407	0.9821
P(S_1 and S_2 have same 1st quartile)	9.750 E -113	1.246 E -112	0.8019
P(S_1 and S_2 have same medians)	5.288 E -88	5.409 E -88	0.9997
P(S_1 and S_2 have same 3rd quartiles)	6.534 E -81	6.730 E -81	0.9577
P(S_1 and S_2 have same maximums)	2.536 E -98	6.180 E -103	0.4068

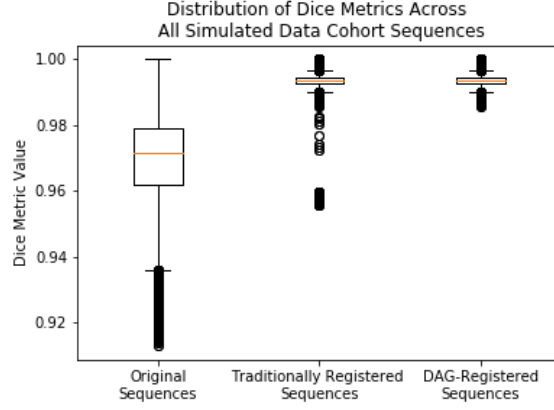


Figure 43: Boxplots of the values of all Dice matrices for the original sequences, the traditionally registered sequences, and the DAG-registered sequences for the simulated data.

Table 18: Results of t-tests comparing the descriptive statistics of the Dice matrices for the simulated data.

Sequence Type 1 (S_1)	Original	Original	Traditionally Registered
Sequence Type 2 (S_2)	Traditionally Registered	DAG Registered	DAG Registered
$P(S_1 \text{ and } S_2 \text{ have same minimums})$	9.976 E -105	2.520 E -110	0.3778
$P(S_1 \text{ and } S_2 \text{ have same 1st quartile})$	5.225 E -93	5.582 E -93	0.931
$P(S_1 \text{ and } S_2 \text{ have same medians})$	1.988 E -104	2.158 E -104	0.9578
$P(S_1 \text{ and } S_2 \text{ have same 3rd quartiles})$	1.679 E -131	2.190 E -131	0.842
$P(S_1 \text{ and } S_2 \text{ have same maximums})$	1.0	1.0	1.0

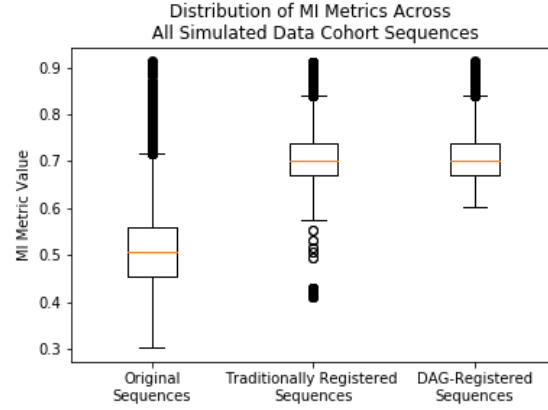


Figure 44: Boxplots of the values of all MI matrices for the original sequences, the traditionally registered sequences, and the DAG-registered sequences for the simulated data.

Table 19: Results of t-tests comparing the descriptive statistics of the MI matrices for the simulated data.

Sequence Type 1 (S_1)	Original	Original	Traditionally Registered
Sequence Type 2 (S_2)	Traditionally Registered	DAG Registered	DAG Registered
$P(S_1 \text{ and } S_2 \text{ have same minimums})$	5.016 E -114	6.328 E -126	0.5397
$P(S_1 \text{ and } S_2 \text{ have same 1st quartile})$	4.68 E -105	7.90 E -105	0.995
$P(S_1 \text{ and } S_2 \text{ have same medians})$	1.65 E -97	3.57 E -97	0.994
$P(S_1 \text{ and } S_2 \text{ have same 3rd quartiles})$	1.065 E -84	2.374 E -84	0.974
$P(S_1 \text{ and } S_2 \text{ have same maximums})$	0.00473	0.00794	0.8761

Table 20: The average true and false rates for both positive and negative voxels when comparing the IC component with the largest correlation to the DMN ROI over each simulated image.

Average Value	Traditionally Registered	DAG-Registered
TPR	0.587	0.623
FPR	0.104	0.00996
TNR	0.990	0.990
FNR	0.413	0.377

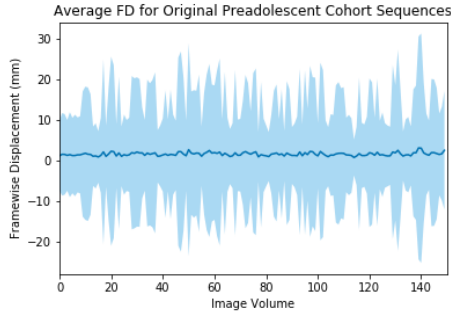
B.1.3 Volume Registration: Recovered Signal

Table 21: The p-values determining whether the true and false rates for both positive and negative voxels differ between the traditionally registered and DAG-registered simulated sequences as calculated using the two-sided t-test.

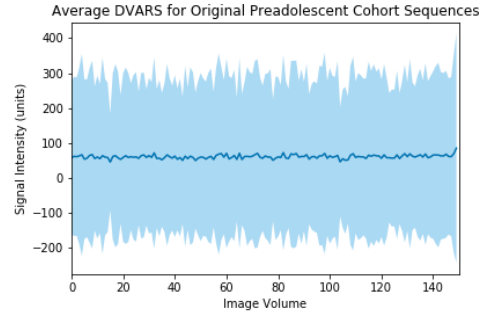
Rate	2 Sided t-test p-value
TPR	0.441
FPR	0.729
TNR	0.729
FNR	0.441

B.2 PREADOLESCENT COHORT

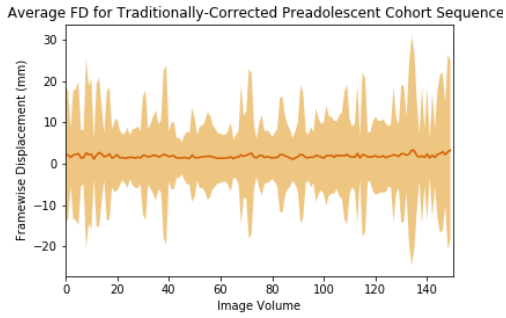
B.2.1 Volume Registration: Power Thresholds



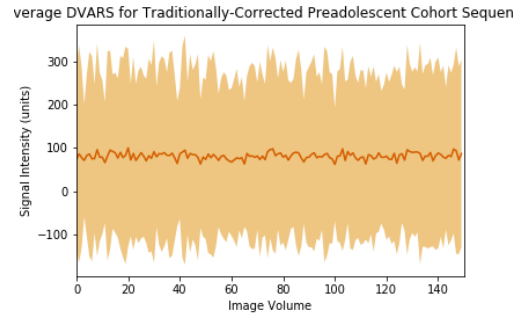
(a) FD of Original Sequences.



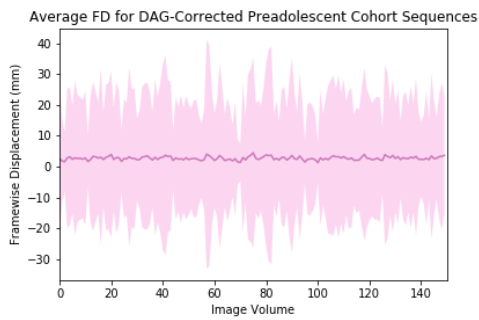
(b) DVARS of Original Sequences.



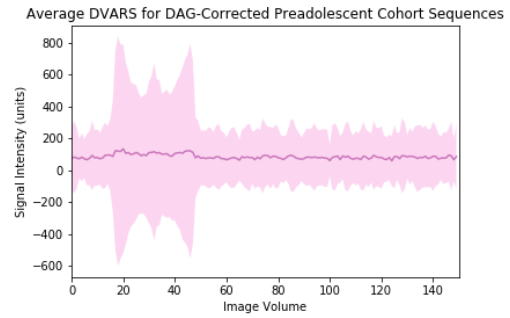
(c) FD of Traditionally Registered Sequences.



(d) DVARS of Traditionally Registered Sequences.



(e) FD of DAG-Registered Sequences.



(f) DVARS of DAG-Registered Sequences.

Figure 45: The means and standard deviations of the FD and DVARS metrics for all preadolescent images both before and after registration.

Table 22: The number and percentage of image volumes across all sequences in the preadolescent cohort which meet the usability thresholds of FD <0.2 mm and DVARS <2.5%.

Threshold Met	Original Sequences	Traditionally Registered Sequences	DAG-Registered Sequences
FD (count)	107879	72104	72114
DVARS (count)	87169	54056	53756
Both (count)	74107	45006	44682
FD (%)	60.17	40.22	40.26
DVARS(%)	48.62	30.15	30.01
Both (%)	41.33	25.10	24.94

Table 23: Results from the t-tests comparing the counts for the numbers of images meeting the FD, DVARS, and FD and DVARS thresholds for sequence type S_1 and sequence type S_2 .

Sequence Type 1 (S_1)	Original	Original	Traditionally Registered
Sequence Type 2 (S_2)	Traditionally Registered	DAG Registered	DAG Registered
P(S_1 and S_2 have same FD counts)	2.81 E -16	2.35 E -16	0.998
P(S_1 and S_2 have same DVARS counts)	9.43 E -12	5.30 E -12	0.950
P(S_1 and S_2 have same FD and DVARS counts)	1.12 E -11	5.60 E -12	0.938

Table 24: The number of subjects whose sequences of types S_1 and S_2 had different FD distributions.

# Sequences Type 1 (S_1)	# Sequences Type 2 (S_2)	# Sequences $p < 0.05$	# Sequences $p < 0.005$
Original	Traditionally Registered	331	326
Original	DAG Registered	332	328
Traditionally Registered	DAG Registered	19	17

Table 25: The number of subjects whose sequences of types S_1 and S_2 had different DVARS distributions.

# Sequences Type 1 (S_1)	# Sequences Type 2 (S_2)	# Sequences $p < 0.05$	# Sequences $p < 0.005$
Original	Traditionally Registered	334	331
Original	DAG Registered	334	333
Traditionally Registered	DAG Registered	22	19

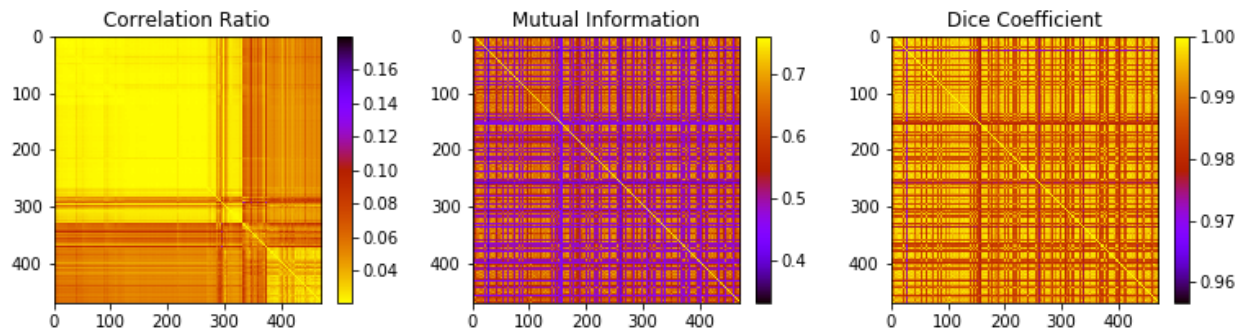


Figure 46: Examples of the three similarity matrices. Lighter colors represent more desirable values.

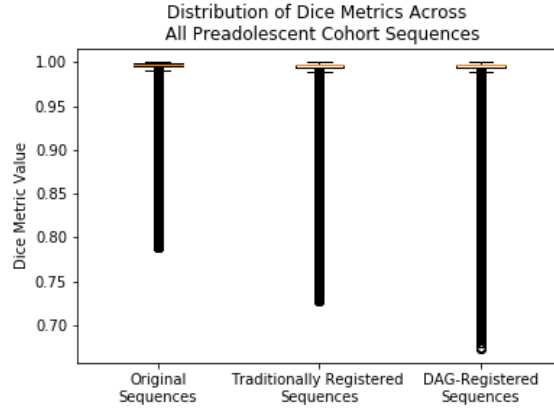


Figure 47: Boxplots of the values of all Dice matrices for the original sequences, the traditionally registered sequences, and the DAG-registered sequences for the preadolescent cohort.

B.2.2 Volume Registration: Sequence Duration Motion

Table 26: Results of t-tests comparing the descriptive statistics of the Dice matrices for the preadolescent data.

Sequence Type 1 (S_1)	Original	Original	Traditionally Registered
Sequence Type 2 (S_2)	Traditionally Registered	DAG Registered	DAG Registered
P(S_1 and S_2 have same minimums)	0.770	0.695	0.916
P(S_1 and S_2 have same 1st quartile)	0.976	0.906	0.880
P(S_1 and S_2 have same medians)	0.883	0.562	0.643
P(S_1 and S_2 have same 3rd quartiles)	0.000343	0.000586	0.390
P(S_1 and S_2 have same maximums)	1.0	1.0	1.0

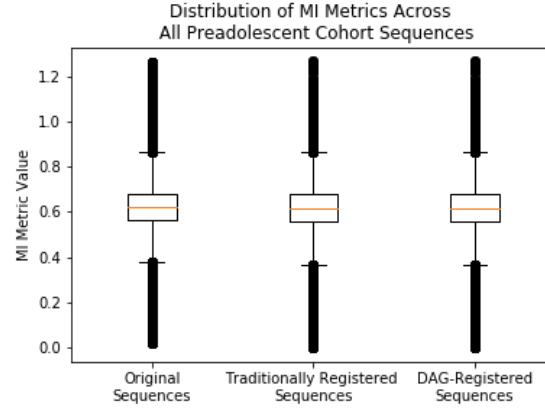


Figure 48: Boxplots of the values of all MI matrices for the original sequences, the traditionally registered sequences, and the DAG-registered sequences for the preadolescent cohort.

Table 27: Results of t-tests comparing the descriptive statistics of the MI matrices for the preadolescent data.

Sequence Type 1 (S_1)	Original	Original	Traditionally Registered
Sequence Type 2 (S_2)	Traditionally Registered	DAG Registered	DAG Registered
P(S_1 and S_2 have same minimums)	0.624	0.718	0.896
P(S_1 and S_2 have same 1st quartile)	0.489	0.497	0.992
P(S_1 and S_2 have same medians)	0.364	0.324	0.928
P(S_1 and S_2 have same 3rd quartiles)	0.121	0.0882	0.851
P(S_1 and S_2 have same maximums)	0.946	0.932	0.987

Table 28: The number of preadolescent subjects whose sequences of types S_1 and S_2 had different MI distributions.

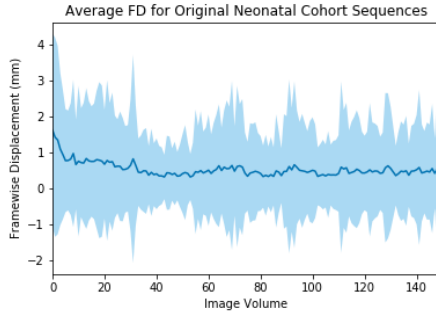
# Sequences Type 1 (S_1)	# Sequences Type 2 (S_2)	# Sequences $p < 0.05$	# Sequences $p < 0.005$
Original	Traditionally Registered	189	187
Original	DAG Registered	189	185
Traditionally Registered	DAG Registered	84	69

Table 29: The number of preadolescent subjects whose sequences of types S_1 and S_2 had different Dice distributions.

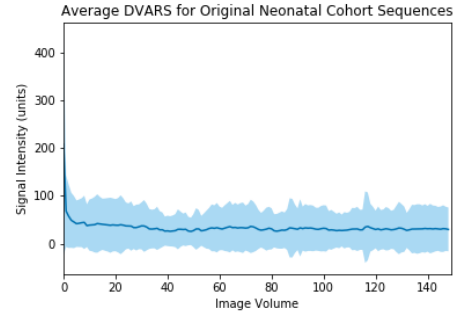
# Sequences Type 1 (S_1)	# Sequences Type 2 (S_2)	# Sequences $p < 0.05$	# Sequences $p < 0.005$
Original	Traditionally Registered	188	185
Original	DAG Registered	187	185
Traditionally Registered	DAG Registered	83	75

B.3 NEONATAL COHORT

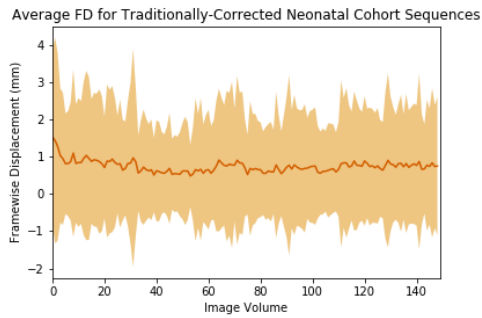
B.3.1 Volume Registration: Power Thresholds



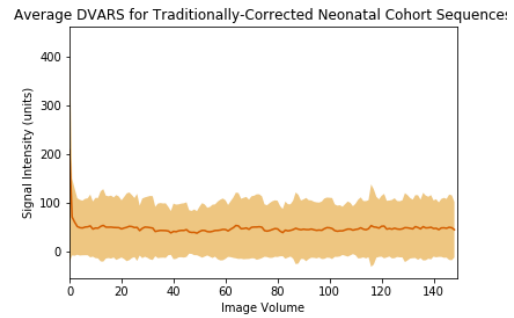
(a) FD of Original Sequences.



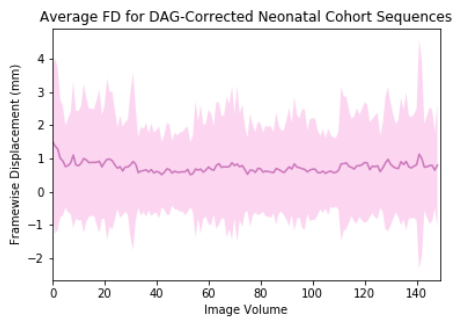
(b) DVARS of Original Sequences.



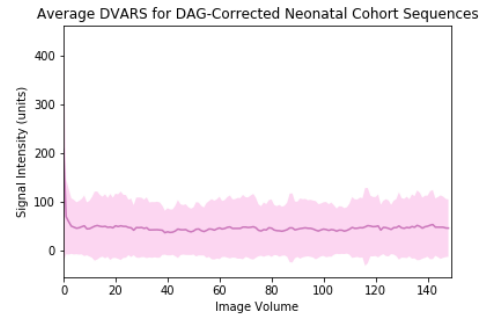
(c) FD of Traditionally Registered Sequences.



(d) DVARS of Traditionally Registered Sequences.



(e) FD of DAG-Registered Sequences.



(f) DVARS of DAG-Registered Sequences.

Figure 49: The means and standard deviations of the FD and DVARS metrics for all neonatal images both before and after registration.

Table 30: The number and percentage of image volumes across all sequences in the neonatal cohort which meet the usability thresholds of FD <0.2 mm and DVARs <2.5%.

Threshold Met	Original Sequences	Traditionally Registered Sequences	DAG-Registered Sequences
FD (count)	16495	14264	14173
DVARs (count)	16820	13903	13752
Both (count)	15332	12837	12684
FD (%)	69.59	60.18	59.79
DVARs(%)	70.96	58.65	58.02
Both (%)	64.68	54.16	53.51

Table 31: Results from the t-tests comparing the counts for the numbers of images meeting the FD, DVARs, and FD and DVARs thresholds for sequence type S_1 and sequence type S_2 .

Sequence Type 1 (S_1)	Original	Original	Traditionally Registered
Sequence Type 2 (S_2)	Traditionally Registered	DAG Registered	DAG Registered
P(S_1 and S_2 have same FD counts)	0.0110	0.00813	0.924
P(S_1 and S_2 have same DVARs counts)	0.00163	0.000942	0.880
P(S_1 and S_2 have same FD and DVARs counts)	0.00779	0.00475	0.879

Table 32: The number of subjects whose sequences of types S_1 and S_2 had different FD distributions.

# Sequences Type 1 (S_1)	# Sequences Type 2 (S_2)	# Sequences $p < 0.05$	# Sequences $p < 0.005$
Original	Traditionally Registered	36	32
Original	DAG Registered	42	38
Traditionally Registered	DAG Registered	13	5

Table 33: The number of subjects whose sequences of types S_1 and S_2 had different DVARS distributions.

# Sequences Type 1 (S_1)	# Sequences Type 2 (S_2)	# Sequences $p < 0.05$	# Sequences $p < 0.005$
Original	Traditionally Registered	44	39
Original	DAG Registered	45	44
Traditionally Registered	DAG Registered	11	5

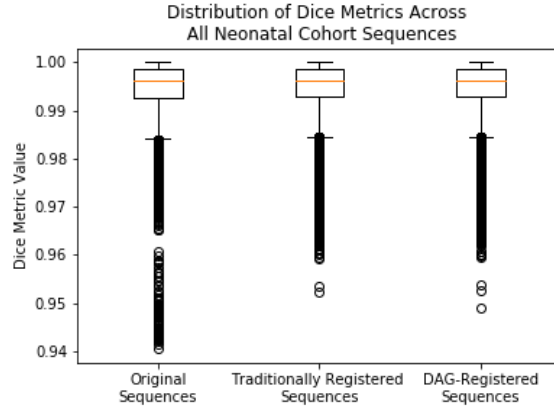


Figure 50: Boxplots of the values of all Dice matrices for the original sequences, the traditionally registered sequences, and the DAG-registered sequences for the neonatal cohort.

B.3.2 Volume Registration: Sequence Duration Motion

Table 34: Results of t-tests comparing the descriptive statistics of the Dice matrices for the neonatal cohort.

Sequence Type 1 (S_1)	Original	Original	Traditionally Registered
Sequence Type 2 (S_2)	Traditionally Registered	DAG Registered	DAG Registered
P(S_1 and S_2 have same minimums)	0.523	0.542	0.977
P(S_1 and S_2 have same 1st quartile)	0.468	0.515	0.933
P(S_1 and S_2 have same medians)	0.329	0.292	0.937
P(S_1 and S_2 have same 3rd quartiles)	0.149	0.115	0.890
P(S_1 and S_2 have same maximums)	1.0	1.0	1.0

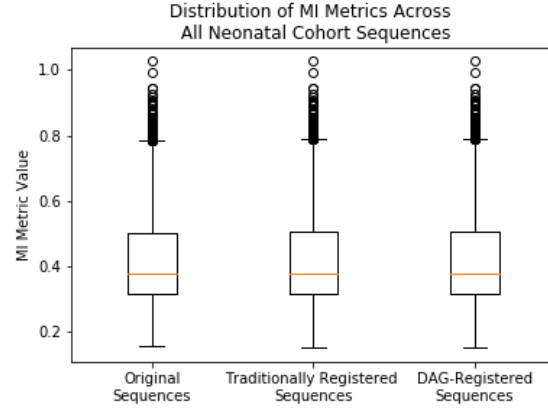


Figure 51: Boxplots of the values of all MI matrices for the original sequences, the traditionally registered sequences, and the DAG-registered sequences for the neonatal cohort.

Table 35: Results of t-tests comparing the descriptive statistics of the MI matrices for the neonatal data.

Sequence Type 1 (S_1)	Original	Original	Traditionally Registered
Sequence Type 2 (S_2)	Traditionally Registered	DAG Registered	DAG Registered
P(S_1 and S_2 have same minimums)	0.853	0.874	0.978
P(S_1 and S_2 have same 1st quartile)	0.794	0.809	0.985
P(S_1 and S_2 have same medians)	0.762	0.758	0.996
P(S_1 and S_2 have same 3rd quartiles)	0.755	0.743	0.987
P(S_1 and S_2 have same maximums)	0.956	0.938	0.982

Table 36: The number of neonatal subjects whose sequences of types S_1 and S_2 had different MI distributions.

# Sequences Type 1 (S_1)	# Sequences Type 2 (S_2)	# Sequences $p < 0.05$	# Sequences $p < 0.005$
Original	Traditionally Registered	66	64
Original	DAG Registered	71	69
Traditionally Registered	DAG Registered	64	64

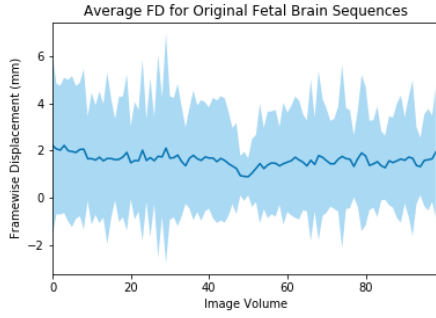
B.4 FETAL COHORT

B.4.1 Brain

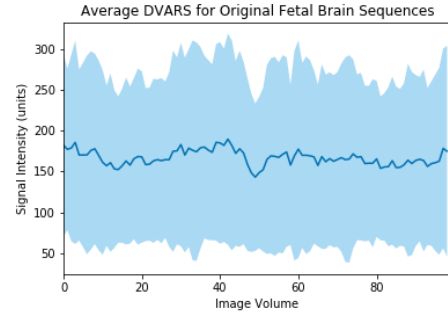
B.4.1.1 Volume Registration: Power Thresholds Table 39 shows the results of a set of t-tests which determine if the distribution of metric X for sequence type S_1 is the same as the distribution of metric X for sequence type S_2 . Fetal brain.

Table 37: The number of neonatal subjects whose sequences of types S_1 and S_2 had different Dice distributions.

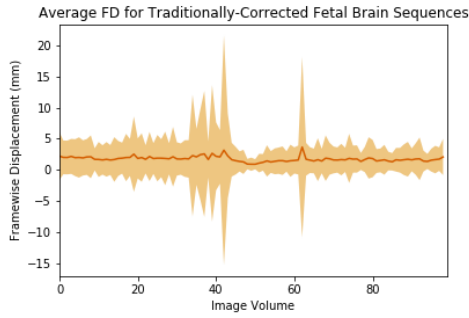
# Sequences Type 1 (S_1)	# Sequences Type 2 (S_2)	# Sequences $p < 0.05$	# Sequences $p < 0.005$
Original	Traditionally Registered	67	66
Original	DAG Registered	71	69
Traditionally Registered	DAG Registered	68	64



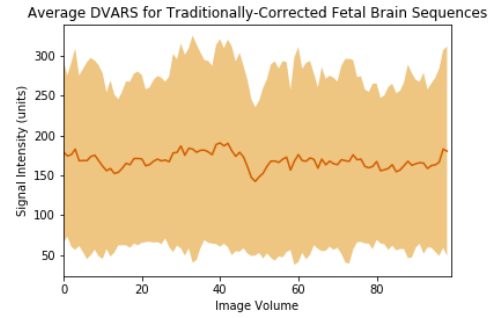
(a) FD of Original Sequences.



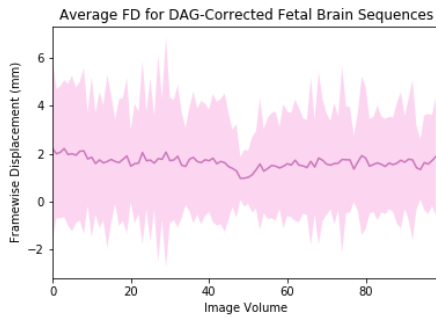
(b) DVARS of Original Sequences.



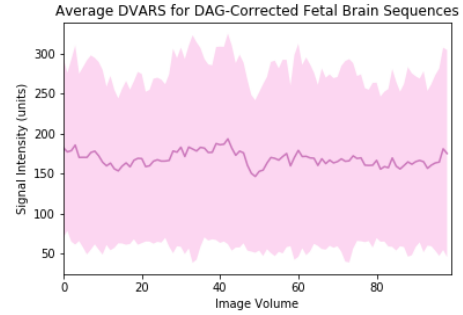
(c) FD of Traditionally Registered Sequences.



(d) DVARS of Traditionally Registered Sequences.



(e) FD of DAG-Registered Sequences.



(f) DVARS of DAG-Registered Sequences.

Figure 52: The means and standard deviations of the FD and DVARS metrics for all fetal brain images both before and after registration.

Table 38: The number and percentage of image volumes across all sequences in the fetal brain image data set which meet the usability thresholds of FD <0.2 mm and DVARs $<2.5\%$.

Threshold Met	Original Sequences	Traditionally Registered Sequences	DAG-Registered Sequences
FD (count)	575	581	561
DVARs (count)	7	84	7
Both (count)	7	80	7
FD (%)	4.775	4.854	4.659
DVARs(%)	0.058	0.702	0.058
Both (%)	0.058	0.668	0.058

Table 39: Results from the t-tests comparing the counts for the numbers of images meeting the FD, DVARs, and FD and DVARs thresholds for fetal brain sequence type S_1 and sequence type S_2 .

Sequence Type 1 (S_1)	Original	Original	Traditionally Registered
Sequence Type 2 (S_2)	Traditionally Registered	DAG Registered	DAG Registered
P(S_1 and S_2 have same FD counts)	0.811	0.926	0.883
P(S_1 and S_2 have same DVARs counts)	0.159	1.0	0.159
P(S_1 and S_2 have same FD and DVARs counts)	0.159	1.0	0.159

Table 40: The number of subjects whose sequences of types S_1 and S_2 had different FD distributions according to the Kolmogorov-Smirnov test.

# Sequences Type 1 (S_1)	# Sequences Type 2 (S_2)	# Sequences $p < 0.05$	# Sequences $p < 0.005$
Original	Traditionally Registered	14	9
Original	DAG Registered	2	2
Traditionally Registered	DAG Registered	13	9

Table 41: The number of subjects whose sequences of types S_1 and S_2 had different DVARS distributions according to the Kolmogorov-Smirnov test.

# Sequences Type 1 (S_1)	# Sequences Type 2 (S_2)	# Sequences $p < 0.05$	# Sequences $p < 0.005$
Original	Traditionally Registered	3	3
Original	DAG Registered	2	1
Traditionally Registered	DAG Registered	2	2

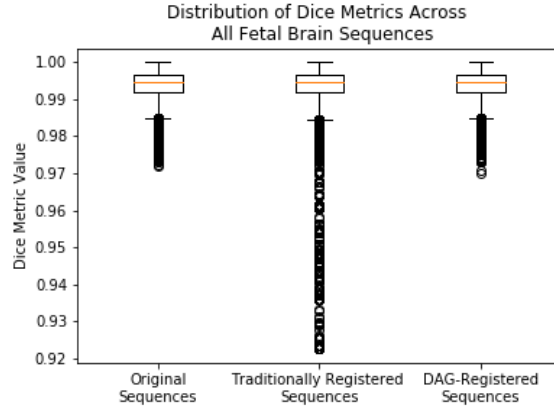


Figure 53: Boxplots of the values of all Dice matrices for the original sequences, the traditionally registered sequences, and the DAG-registered sequences for the fetal-brain images.

B.4.1.2 Volume Registration: Sequence Duration Motion

Table 42: Results of t-tests comparing the descriptive statistics of the Dice matrices for the fetal brain data.

Sequence Type 1 (S_1)	Original	Original	Traditionally Registered
Sequence Type 2 (S_2)	Traditionally Registered	DAG Registered	DAG Registered
P(S_1 and S_2 have same minimums)	0.259	0.932	0.289
P(S_1 and S_2 have same 1st quartile)	0.254	0.996	0.252
P(S_1 and S_2 have same medians)	0.658	0.970	0.686
P(S_1 and S_2 have same 3rd quartiles)	0.973	0.921	0.896
P(S_1 and S_2 have same maximums)	1.0	1.0	1.0

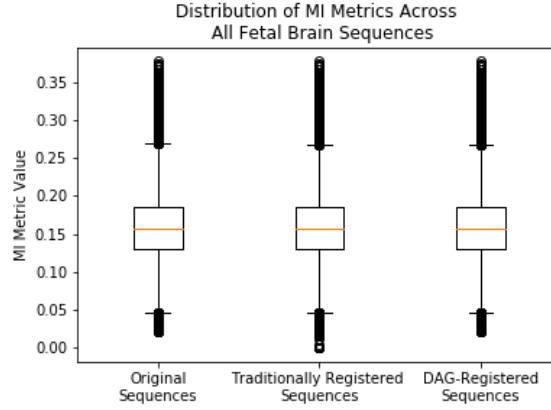


Figure 54: Boxplots of the values of all MI matrices for the original sequences, the traditionally registered sequences, and the DAG-registered sequences for the fetal brain images.

Table 43: Results of t-tests comparing the descriptive statistics of the MI matrices for the fetal brain data.

Sequence Type 1 (S_1)	Original	Original	Traditionally Registered
Sequence Type 2 (S_2)	Traditionally Registered	DAG Registered	DAG Registered
P(S_1 and S_2 have same minimums)	0.673	0.845	0.816
P(S_1 and S_2 have same 1st quartile)	0.765	0.963	0.798
P(S_1 and S_2 have same medians)	0.764	0.963	0.798
P(S_1 and S_2 have same 3rd quartiles)	0.760	0.959	0.797
P(S_1 and S_2 have same maximums)	0.539	0.999	0.539

Table 44: The number of subjects whose sequences of types S_1 and S_2 had different MI distributions.

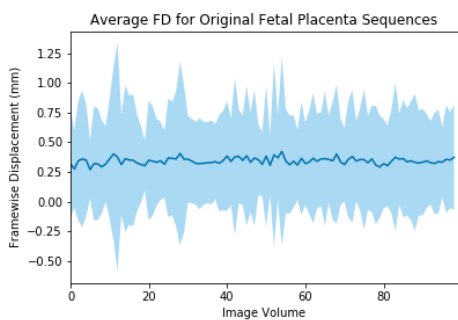
# Sequences Type 1 (S_1)	# Sequences Type 2 (S_2)	# Sequences $p < 0.05$	# Sequences $p < 0.005$
Original	Traditionally Registered	13	10
Original	DAG Registered	12	9
Traditionally Registered	DAG Registered	14	9

Table 45: The number of subjects whose sequences of types S_1 and S_2 had different Dice distributions.

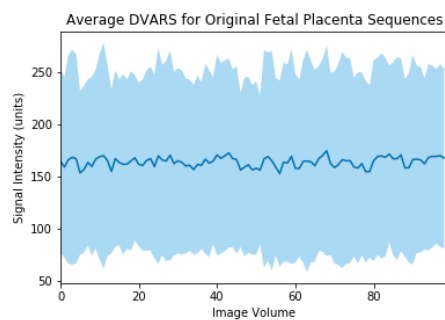
# Sequences Type 1 (S_1)	# Sequences Type 2 (S_2)	# Sequences $p < 0.05$	# Sequences $p < 0.005$
Original	Traditionally Registered	11	9
Original	DAG Registered	7	7
Traditionally Registered	DAG Registered	10	8

B.4.2 Placenta

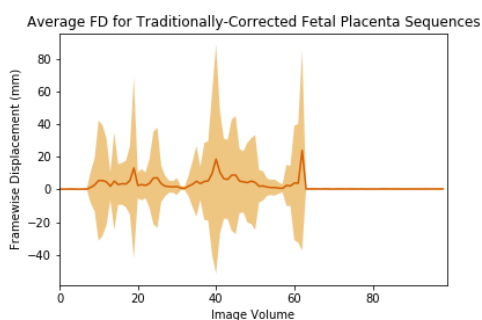
B.4.2.1 Volume Registration: Power Thresholds



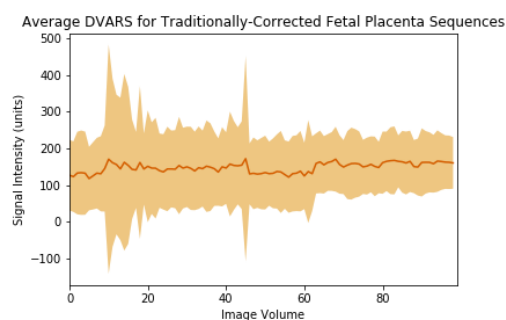
(a) FD of Original Sequences.



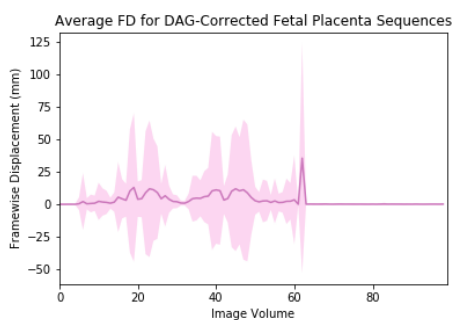
(b) DVARS of Original Sequences.



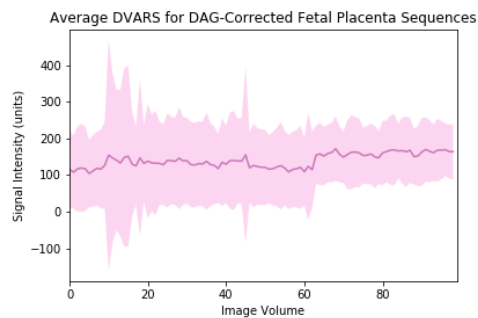
(c) FD of Traditionally Registered Sequences.



(d) DVARS of Traditionally Registered Sequences.



(e) FD of DAG-Registered Sequences.



(f) DVARS of DAG-Registered Sequences.

Figure 55: The means and standard deviations of the FD and DVARS metrics for all placenta images both before and after registration.

Table 46: The number and percentage of image volumes across all sequences in the fetal placenta image data set which meet the usability thresholds of FD <0.2 mm and DVARs <2.5%.

Threshold Met	Original Sequences	Traditionally Registered Sequences	DAG-Registered Sequences
FD (count)	10017	4113	4005
DVARs (count)	17	1056	1624
Both (count)	17	599	996
FD (%)	43.646	44.245	45.020
DVARs(%)	0.170	11.36	18.255
Both (%)	0.170	6.444	11.196

Table 47: Results from the t-tests comparing the counts for the numbers of images meeting the FD, DVARs, and FD and DVARs thresholds for fetal placenta sequence type S_1 and sequence type S_2 .

Sequence Type 1 (S_1)	Original	Original	Traditionally Registered
Sequence Type 2 (S_2)	Traditionally Registered	DAG Registered	DAG Registered
P(S_1 and S_2 have same FD counts)	0.519	0.350	0.775
P(S_1 and S_2 have same DVARs counts)	5.38 E -6	5.65 E -9	0.101
P(S_1 and S_2 have same FD and DVARs counts)	5.18 E -6	1.92 E -8	0.0571

Table 48: The number of placental images whose sequences of types S_1 and S_2 had different FD distributions according to the Kolmogorov-Smirnov test.

# Sequences Type 1 (S_1)	# Sequences Type 2 (S_2)	# Sequences $p < 0.05$	# Sequences $p < 0.005$
Original	Traditionally Registered	21	21
Original	DAG Registered	32	30
Traditionally Registered	DAG Registered	31	20

Table 49: The number of placental images whose sequences of types S_1 and S_2 had different DVARS distributions according to the Kolmogorov-Smirnov test.

# Sequences Type 1 (S_1)	# Sequences Type 2 (S_2)	# Sequences $p < 0.05$	# Sequences $p < 0.005$
Original	Traditionally Registered	20	20
Original	DAG Registered	29	29
Traditionally Registered	DAG Registered	19	19

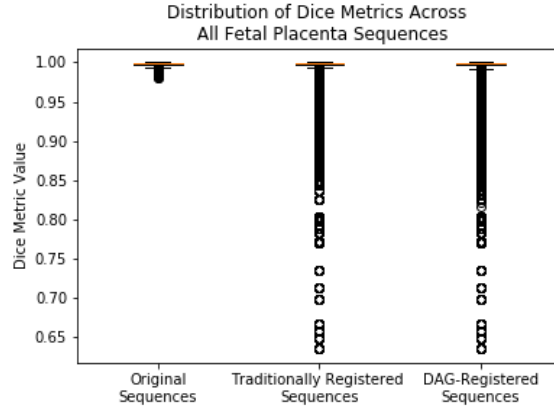


Figure 56: Boxplots of the values of all Dice matrices for the original sequences, the traditionally registered sequences, and the DAG-registered sequences for the placenta images.

B.4.2.2 Volume Registration: Sequence Duration Motion

Table 50: Results of t-tests comparing the descriptive statistics of the Dice matrices for the fetal placenta data.

Sequence Type 1 (S_1)	Original	Original	Traditionally Registered
Sequence Type 2 (S_2)	Traditionally Registered	DAG Registered	DAG Registered
P(S_1 and S_2 have same minimums)	6.39 E -5	3.43 E -7	0.257
P(S_1 and S_2 have same 1st quartile)	6.54 E -5	2.35 E -6	0.257
P(S_1 and S_2 have same medians)	0.000310	9.46 E -5	0.816
P(S_1 and S_2 have same 3rd quartiles)	0.096	0.104	0.902
P(S_1 and S_2 have same maximums)	1.0	1.0	1.0

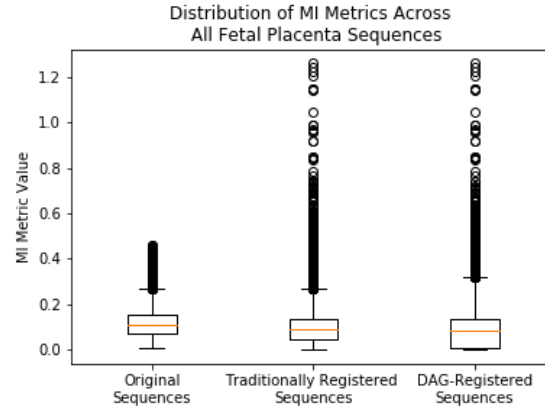


Figure 57: Boxplots of the values of all MI matrices for the original sequences, the traditionally registered sequences, and the DAG-registered sequences for the placenta images.

Table 51: Results of t-tests comparing the descriptive statistics of the MI matrices for the fetal placenta data.

Sequence Type 1 (S_1)	Original	Original	Traditionally Registered
Sequence Type 2 (S_2)	Traditionally Registered	DAG Registered	DAG Registered
P(S_1 and S_2 have same minimums)	0.00980	0.00168	0.536
P(S_1 and S_2 have same 1st quartile)	0.00742	0.00132	0.548
P(S_1 and S_2 have same medians)	0.00713	0.00116	0.535
P(S_1 and S_2 have same 3rd quartiles)	0.00807	0.00118	0.506
P(S_1 and S_2 have same maximums)	0.00145	8.28 E -6	0.212

Table 52: The number of subjects whose placenta sequences of types S_1 and S_2 had different MI distributions.

# Sequences Type 1 (S_1)	# Sequences Type 2 (S_2)	# Sequences $p < 0.05$	# Sequences $p < 0.005$
Original	Traditionally Registered	22	22
Original	DAG Registered	39	39
Traditionally Registered	DAG Registered	38	38

Table 53: The number of subjects whose placenta sequences of types S_1 and S_2 had different Dice distributions.

# Sequences Type 1 (S_1)	# Sequences Type 2 (S_2)	# Sequences $p < 0.05$	# Sequences $p < 0.005$
Original	Traditionally Registered	22	22
Original	DAG Registered	39	39
Traditionally Registered	DAG Registered	30	30

B.5 CHARACTERIZING MOTION

B.5.1 Age Groups

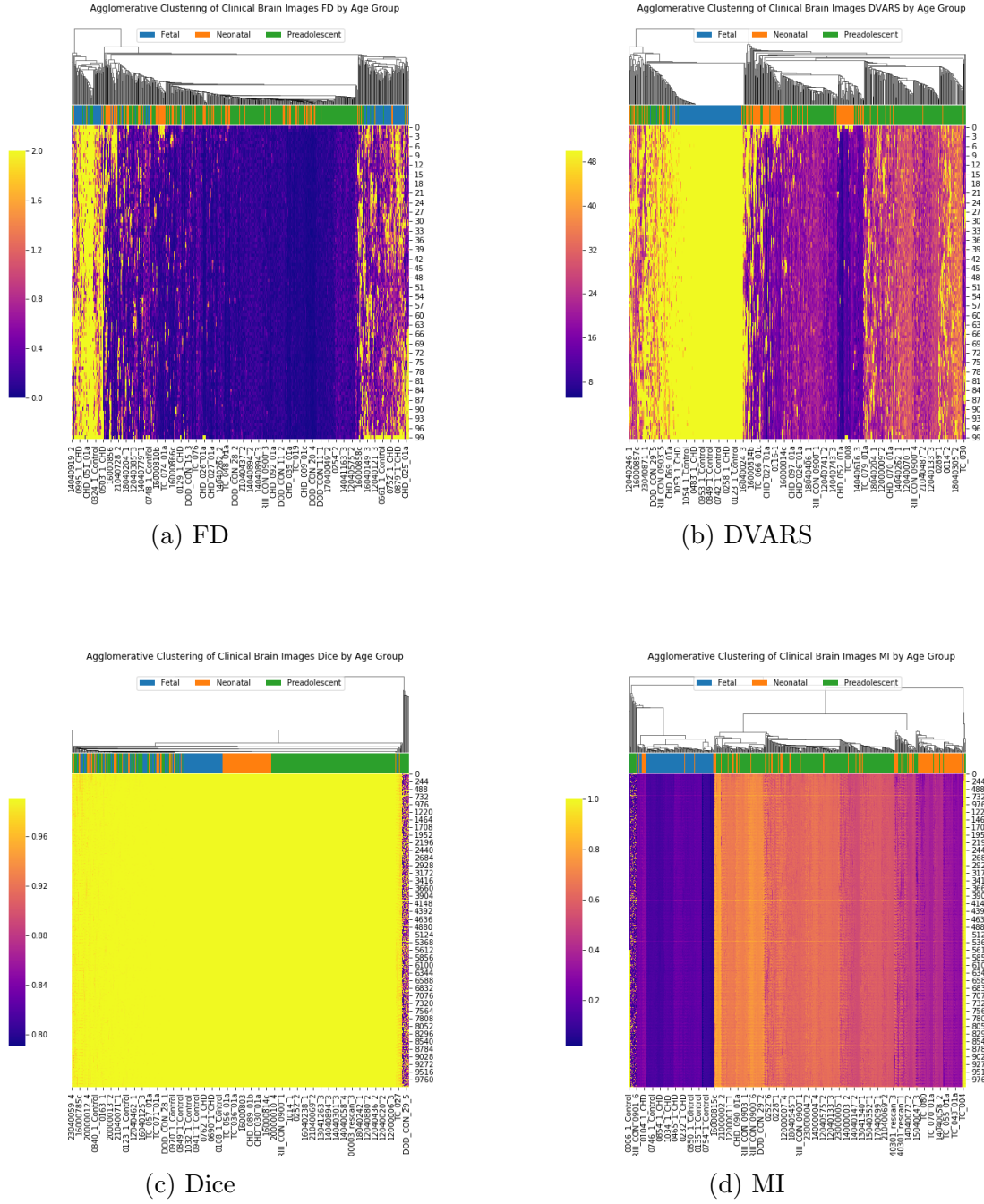


Figure 58: The preadolescent, neonatal, and fetal images clustered by each metric using agglomerative clustering and labeled by age group.

B.5.2 CHD and Control

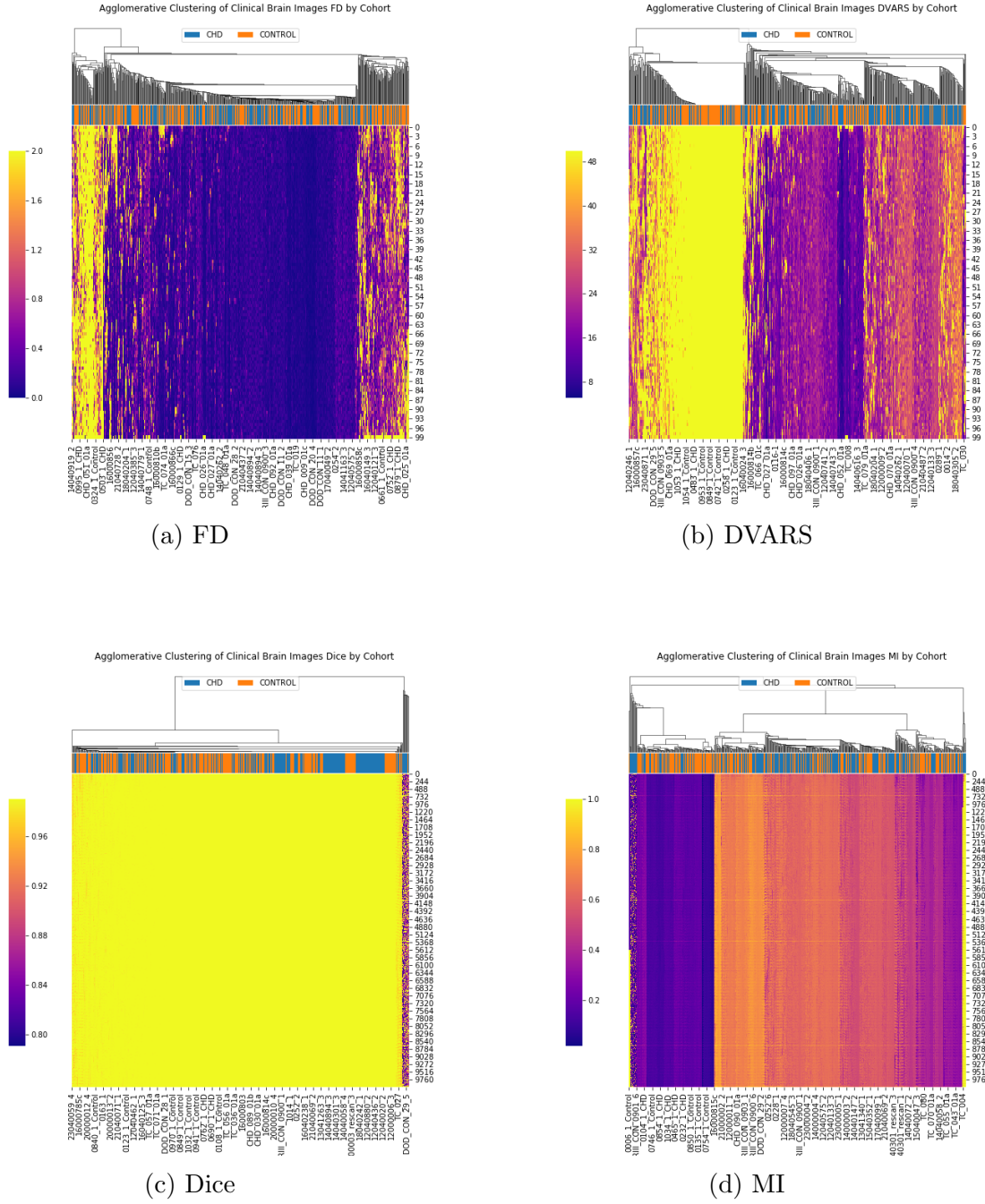


Figure 59: The preadolescent, neonatal, and fetal images clustered by each metric using agglomerative clustering and labeled by CHD/Control status.

BIBLIOGRAPHY

TensorFlow Projector.

Abdi, H. and Williams, L. J. (2010). Principal component analysis. *WIREs Computational Statistics*, 2:433–459.

Afacan, O., Erem, B., Roby, D. P., Roth, N., Roth, A., Prabhu, S. P., and Warfield, S. K. (2016). Evaluation of motion and its effect on brain magnetic resonance image quality in children. *Pediatric Radiology*, 46(12):1728–1735.

Aksoy, M., Newbould, R., Straka, M., Holdsworth, S. J., Skare, S. T., Santos, J. M., and Bammer, R. (2008). A Real Time Optical Motion Correction System Using a Single Camera and 2D Marker. *Proceedings of the 16th Scientific Meeting of ISMRM*, 16:3120.

Alexander, M. (2012). Managing Patient Stress in Pediatric Radiology. *Radiologic Technology*, 83(6):549–560.

Altmann, A., Ng, B., Landau, S. M., Jagust, W. J., Greicius, M. D., and Alzheimer’s Disease Neuroimaging Initiative (2015). Regional brain hypometabolism is unrelated to regional amyloid plaque burden. *Brain : a journal of neurology*, 138(Pt 12):3734–46.

Assaf, M., Jagannathan, K., Calhoun, V. D., Miller, L., Stevens, M. C., Sahl, R., O’Boyle, J. G., Schultz, R. T., and Pearlson, G. D. (2010). Abnormal functional connectivity of default mode sub-networks in autism spectrum disorder patients. *NeuroImage*, 53(1):247–256.

Avants, B. B., Tustison, N. J., Stauffer, M., Song, G., Wu, B., and Gee, J. C. (2014). The Insight ToolKit image registration framework. *Frontiers in Neuroinformatics*, 8(April).

Ayres, L. P. (1920). The correlation ratio. *The Journal of Educational Research*, 2(1):452–456.

Barnea-Goraly, N., Weinzimer, S. A., Ruedy, K. J., Mauras, N., Beck, R. W., Marzelli, M. J., Mazaika, P. K., Aye, T., White, N. H., Tsalikian, E., Fox, L., Kollman, C., Cheng, P., and Reiss, A. L. (2014). High success rates of sedation-free brain MRI scanning in young children using simple subject preparation protocols with and without a commercial mock

- scanner - the Diabetes Research in Children Network (DirecNet) experience. *Pediatric Radiology*, 44(2):181–186.
- Barnes, K. A., Nelson, S. M., Cohen, A. L., Power, J. D., Coalson, R. S., Miezin, F. M., Vogel, A. C., Dubis, J. W., Church, J. A., Petersen, S. E., and Schlaggar, B. L. (2011). Parcellation in left lateral parietal cortex is similar in adults and children. *Cerebral Cortex*, 22(5):1148–1158.
- Beckmann, C. F., Deluca, M., Devlin, J. T., and Smith, S. M. Investigations into Resting-state Connectivity using Independent Component Analysis (FMRIB Technical Report TR05CB1).
- Beckmann, C. F. and Smith, S. M. (2004). Probabilistic Independent Component Analysis for Functional Magnetic Resonance Imaging. *IEEE Transactions on Medical Imaging*, 23(2):137–152.
- Behzadi, Y., Restom, K., Liau, J., and Liu, T. T. (2007). A component based noise correction method (CompCor) for BOLD and perfusion based fMRI. *NeuroImage*, 37(1):90–101.
- Bharatha, A., Hirose, M., Hata, N., Warfield, S. K., Ferrant, M., Zou, K. H., Suarez-Santana, E., Ruiz-Alzola, J., D’Amico, A., Cormack, R. A., Kikinis, R., Jolesz, F. A., and Tempany, C. M. (2001). Evaluation of three-dimensional finite element-based deformable registration of pre- and intraoperative prostate imaging. *Medical Physics*, 28(12):2551–60.
- Biswal, B. B., Kannurpatti, S. S., and Rypma, B. (2007). Hemodynamic scaling of fMRI-BOLD signal: validation of low-frequency spectral amplitude as a scalability factor. *Magnetic Resonance Imaging*, 25(10):1358–1369.
- Coté, C. J. and Wilson, S. (2016). Guidelines for Monitoring and Management of Pediatric Patients Before, During, and After Sedation for Diagnostic and Therapeutic Procedures: Update 2016. *Pediatrics*.
- Dewey, M., Schink, T., and Dewey, C. F. (2007). Claustrophobia during magnetic resonance imaging: Cohort study in over 55,000 patients. *Journal of Magnetic Resonance Imaging*, 26(5):1322–1327.
- Dice, L. R. (1945). Measures of the Amount of Ecologic Association Between Species. *Ecology*, 26(3):297–302.
- Dosenbach, N. U., Koller, J. M., Earl, E. A., Miranda-Dominguez, O., Klein, R. L., Van, A. N., Snyder, A. Z., Nagel, B. J., Nigg, J. T., Nguyen, A. L., Wesevich, V., Greene, D. J., and Fair, D. A. (2017). Real-time motion analytics during brain MRI improve data quality and reduce costs. *NeuroImage*, 161(January):80–93.
- Fair, D. A., Dosenbach, N. U. F., Church, J. A., Cohen, A. L., Brahmbhatt, S., Miezin, F. M., Barch, D. M., Raichle, M. E., Petersen, S. E., and Schlaggar, B. L. (2007). Development

- of distinct control networks through segregation and integration. *Proceedings of the National Academy of Sciences of the United States of America*, 104(33):13507–12.
- Fonov, V., Evans, A., McKinstry, R., Almli, C., and Collins, D. (2009). Unbiased nonlinear average age-appropriate brain templates from birth to adulthood. *NeuroImage*, 47:S102.
- Fonov, V., Evans, A. C., Botteron, K., Almli, C. R., McKinstry, R. C., and Collins, D. L. (2011). Unbiased average age-appropriate atlases for pediatric studies. *NeuroImage*, 54(1):313–327.
- Forman, C., Aksoy, M., Hornegger, J., and Bammer, R. (2011). Self-encoded marker for optical prospective head motion correction in MRI. *Medical Image Analysis*, 15(5):708–719.
- Fox, C. K., Sidney, S., and Fullerton, H. J. (2015). Community-based case-control study of childhood stroke risk associated with congenital heart disease. *Stroke*, 46(2):336–340.
- Fransson, P., Skiöld, B., Horsch, S., Nordell, A., Blennow, M., Lagercrantz, H., and Aden, U. (2007). Resting-state networks in the infant brain. *Proceedings of the National Academy of Sciences of the United States of America*, 104(39):15531–6.
- Friston, K. J., Ashburner, J., Frith, C. D., Poline, J. ., Heather, J. D., and Frackowiak, R. S. (1995). Spatial registration and normalization of images. *Human Brain Mapping*, 3(3):165–189.
- Friston, K. J., Williams, S., Howard, R., Frackowiak, R. S. J., and Turner, R. (1996). Movement-Related effects in fMRI time-series. *Magnetic Resonance in Medicine*, 35(3):346–355.
- Gale, C., Jeffries, S., Logan, K. M., Chappell, K. E., Uthaya, S. N., and Modi, N. (2013). Avoiding sedation in research MRI and spectroscopy in infants: our approach, success rate and prevalence of incidental finding. *Arch Dis Child Fetal Neonatal Ed*, 98:F267–F268.
- Garcia-Palacios, A., Hoffman, H. G., Richards, T. R., Seibel, E. J., and Sharar, S. R. (2007). Use of Virtual Reality Distraction to Reduce Claustrophobia Symptoms during a Mock Magnetic Resonance Imaging Brain Scan: A Case Report. *CyberPsychology and Behavior*, 10(3):485–488.
- Giang, K. W., Mandalenakis, Z., Dellborg, M., Lappas, G., Eriksson, P., Hansson, P.-O., and Rosengren, A. (2018). Long-Term Risk of Hemorrhagic Stroke in Young Patients With Congenital Heart Disease. *Stroke*, pages 1155–1162.
- Gorgolewski, K., Burns, C. D., Madison, C., Clark, D., Halchenko, Y. O., Waskom, M. L., and Ghosh, S. S. (2011). Nipype : a flexible , lightweight and extensible neuroimaging data processing framework in Python. *Frontiers in Neuroinformatics*, 5(August).

- Greicius, M. D., Krasnow, B., Reiss, A. L., and Menon, V. (2003). Functional connectivity in the resting brain: A network analysis of the default mode hypothesis. *Proceedings of the National Academy of Sciences of the United States of America*, 100(1):253–258.
- Harned, R. K. and Strain, J. D. (2001). MRI-compatible audio / visual system : impact on pediatric sedation. *Pediatric Radiology*, pages 247–250.
- Hartigan, J. A. and Wong, M. A. (1979). Algorithm AS 136 A K-Means Clustering Algorithm. *Journal of the Royal Statistical Society*, 28(1):100–108.
- Hofman, M. B., Paschal, C. B., Li, D., Haacke, E. M., Van Rossum, A. C., and Sprenger, M. (1995). Mri of coronary arteries: 2d breath-hold vs 3d respiratory-gated acquisition. *Journal of Computer Assisted Tomography*, 19(1):56–62.
- Hu, X., Le, T. H., Parrish, T., and Erhard, P. (1995). Retrospective estimation and correction of physiological fluctuation in functional MRI. *Magnetic Resonance in Medicine*, 34(2):201–212.
- Jenkinson, M., Bannister, P., Brady, M., and Smith, S. (2002). Improved Optimization for the Robust and Accurate Linear Registration and Motion Correction of Brain Images. *NeuroImage*, 17:825–841.
- Jenkinson, M. and Smith, S. (2001). A global optimisation method for robust affine registration of brain images. *Medical Image Analysis*, 5:143–156.
- Jo, H. J., Gotts, S. J., Reynolds, R. C., Bandettini, P. A., Martin, A., Cox, R. W., and Saad, Z. S. (2013). Effective preprocessing procedures virtually eliminate distance-dependent motion artifacts in resting state fMRI. *Journal of Applied Mathematics*, 2013.
- Jo, H. J., Saad, Z. S., Simmons, W. K., Milbury, L. A., and Cox, R. W. (2010). Mapping sources of correlation in resting state fMRI, with artifact detection and removal. *NeuroImage*, 52(2):571–582.
- Jones, T. B., Bandettini, P. A., Kenworthy, L., Case, L. K., Milleville, S. C., Martin, A., and Birn, R. M. (2010). Sources of group differences in functional connectivity: an investigation applied to autism spectrum disorder. *NeuroImage*, 49(1):401–14.
- Juan, A. and Vidal, E. (1998). Fast Median Search in Metric Spaces. In *Joint IAPR International Workshops on Statistical Techniques in Pattern Recognition (SPR) and Structural and Syntactic Pattern Recognition (SSPR)*, pages 905–912. Springer.
- Kaufman, L. and Rousseeuw, P. J. (1987). Clustering By Means Of Medoids. In *Statistical Data Analysis Based on the $\| \cdot \|_1$ Norm and Related Methods*, pages 405–416. North Holland/Elsevier, Amsterdam.
- Kennedy, D. P. and Courchesne, E. (2008). The intrinsic functional organization of the brain is altered in autism. *NeuroImage*, 39(4):1877–85.

- Khalil, A., Aggarwal, R., Thirupuram, S., and Arora, R. (1994). Incidence of Congenital Heart Disease Among Hospital Live Births in India. *Journal of Indian Pediatrics*, 31:519–527.
- Khan, J. J., Donnelly, L. F., Koch, B. L., Curtwright, L. A., Dickerson, J. M., Hardin, J. L., Hutchinson, S., Wright, J., and Gessner, K. E. (2007). A program to decrease the need for pediatric sedation for CT and MRI. *Applied Radiology*, April:30–33.
- KinetiCor Biometric Intelligence (2019). The kinetikor platform.
- Laumann, T. O., Gordon, E. M., Adeyemo, B., Snyder, A. Z., Joo, S. J., Chen, M.-Y., Gilmore, A. W., McDermott, K. B., Nelson, S. M., Dosenbach, N. U., Schlaggar, B. L., Mumford, J. A., Poldrack, R. A., and Petersen, S. E. (2015). Functional System and Areal Organization of a Highly Sampled Individual Human Brain. *Neuron*, 87(3):657–670.
- Li, W. (1990). Mutual Information Functions versus Correlation Functions. *Journal of Statistical Physics*, 60(5/6):823–837.
- Liao, R., Krolik, J. L., and McKeown, M. J. (2005). An information-theoretic criterion for intrasubject alignment of fMRI time series: Motion corrected independent component analysis. *IEEE Transactions on Medical Imaging*, 24(1):29–44.
- Liao, R., Turk, E. A., Zhang, M., Luo, J., Ellen Grant, P., Adalsteinsson, E., and Golland, P. (2016). Temporal registration in in-utero volumetric MRI time series. *Lecture Notes in Computer Science (including subseries Lecture Notes in Artificial Intelligence and Lecture Notes in Bioinformatics)*, 9902 LNCS:54–62.
- Maclaren, J., Herbst, M., Speck, O., and Zaitsev, M. (2013). Prospective motion correction in brain imaging: A review. *Magnetic Resonance in Medicine*, 69(3):621–636.
- MacQueen, J. (1967). Some methods for classification and analysis of multivariate observations. In *Proceedings of the fifth Berkeley symposium on mathematical statistics and probability*, volume 1, pages 281–297. Oakland, CA, USA.
- Malviya, S., Voepel-Lewis, T., Prochaska, G., and Tait, A. R. (2000). Prolonged Recovery and Delayed Side Effects of Sedation for Diagnostic Imaging Studies in Children. *Pediatrics*, 105(3).
- Mathur, A. M., Neil, J. J., McKinstry, R. C., and Inder, T. E. (2008). Transport, monitoring, and successful brain MR imaging in unsedated neonates. *Pediatric Radiology*, 38(3):260–264.
- McInnes, L., Healy, J., and Melville, J. (2018). UMAP: Uniform Manifold Approximation and Projection for Dimension Reduction. *arXiv preprint arXiv:1802.03426*.

- Mebius, M. J., Kooi, E. M., Bilardo, C. M., and Bos, A. F. (2017). Brain Injury and Neurodevelopmental Outcome in Congenital Heart Disease: A Systematic Review. *Pediatrics*, 140(1):e20164055.
- Mozaffarian, D., Benjamin, E. J., Go, A. S., Arnett, D. K., Blaha, M. J., Cushman, M., Das, S. R., Ferranti, S. D., Després, J.-p., Fullerton, H. J., Howard, V. J., Huffman, M. D., Isasi, C. R., Jiménez, M. C., Judd, S. E., Kissela, B. M., Lichtman, J. H., Lisabeth, L. D., Liu, S., Mackey, R. H., Magid, D. J., McGuire, D. K., Mohler, E. R., Moy, C. S., Muntner, P., Mussolino, M. E., Nasir, K., Neumar, R. W., Nichol, G., Palaniappan, L., Pandey, D. K., Reeves, M. J., Rodriguez, C. J., Rosamond, W., Sorlie, P. D., Stein, J., Towfighi, A., Turan, T. N., Virani, S. S., Woo, D., Yeh, R. W., and Turner, M. B. (2016). *Heart Disease and Stroke Statistics 2016 Update A Report From the American Heart Association*. American Heart Association.
- Murphy, K. J. and Brunberg, J. A. (1997). Adult claustrophobia, anxiety and sedation in MRI. *Magnetic Resonance Imaging*, 15(1):51–54.
- Nadler, B. and Galun, M. (2007). Fundamental limitations of spectral clustering. *Advances in Neural Information Processing Systems*, pages 1017–1024.
- Ng, A. Y., Jordan, M. I., and Weiss, Y. (2002). On spectral clustering: Analysis and an algorithm. In *Advances in neural information processing systems*, pages 849–856.
- Nikyar, B., Sedehi, M., Mirfazeli, A., Qorbani, M., and Gholipour, M.-J. (2011). Prevalence and Pattern of Congenital Heart Disease among Neonates in Gorgan, Northern Iran (2007-2008). *Iranian Journal of Pediatrics*, 21(3):307–12.
- Parkes, L., Fulcher, B. D., Yucel, M., and Fornito, A. (2017). An evaluation of the efficacy, reliability, and sensitivity of motion correction strategies for resting-state functional MRI. *bioRxiv*.
- Patel, A. X., Kundu, P., Rubinov, M., Jones, P. S., Vértes, P. E., Ersche, K. D., Suckling, J., and Bullmore, E. T. (2014). A wavelet method for modeling and despiking motion artifacts from resting-state fMRI time series. *NeuroImage*, 95:287–304.
- Patriat, R., Reynolds, R. C., and Birn, R. M. (2017). An improved model of motion-related signal changes in fMRI. *NeuroImage*, 144:74–82.
- Power, J. D., Barnes, K. A., Snyder, A. Z., Schlagger, B. L., and Petersen, S. E. (2012). Spurious but systematic correlations in functional connectivity MRI networks arise from subject motion. *NeuroImage*, 59(3):2142–2154.
- Power, J. D., Mitra, A., Laumann, T. O., Snyder, A. Z., Schlaggar, B. L., and Petersen, S. E. (2014). Methods to detect, characterize, and remove motion artifact in resting state fMRI. *NeuroImage*, 84:320–341.

- Power, J. D., Schlaggar, B. L., and Petersen, S. E. (2015). Recent progress and outstanding issues in motion correction resting state fmri. *NeuroImage*, 105:536–551.
- Pruim, R. H., Mennes, M., van Rooij, D., Llera, A., Buitelaar, J. K., and Beckmann, C. F. (2015). ICA-AROMA: A robust ICA-based strategy for removing motion artifacts from fMRI data. *NeuroImage*, 112:267–277.
- Qu, Y., Liu, X., Zhuang, J., Chen, G., Mai, J., Guo, X., Ou, Y., Chen, J., Gong, W., Gao, X., Wu, Y., and Nie, Z. (2016). Incidence of Congenital Heart Disease: The 9-Year Experience of the Guangdong Registry of Congenital Heart Disease, China. *PLOS ONE*, 11(7):e0159257.
- Rahim, F., Ebadi, A., Saki, G., and Remazani, A. (2008). Prevalence of Congenital Heart Disease in Iran: A Clinical Study. *Journal of Medical Sciences(Faisalabad)*, 8(6):547–552.
- Raichle, M. E., MacLeod, A. M., Snyder, A. Z., Powers, W. J., Gusnard, D. A., and Shulman, G. L. (2001). A default mode of brain function. *Proceedings of the National Academy of Sciences*, 98(2):676–682.
- Roche, A., Malandain, G., Ayache, N., and Pennec, X. (1998a). *Multimodal image registration by maximization of the correlation ratio*. PhD thesis, INRIA.
- Roche, A., Malandain, G., Pennec, X., and Ayache, N. (1998b). The correlation ratio as a new similarity measure for multimodal image registration. *Proceedings of MICCAI*, pages 1115–1124.
- Rugg, H. O. (1917). *Statistical methods applied to education: A textbook for students of education in the quantitative study of school problems*. Houghton Mifflin.
- Rutman, M. S. (2009). Sedation for emergent diagnostic imaging studies in pediatric patients. *Current Opinion in Pediatrics*, 21(3):306–312.
- Salimi-Khorshidi, G., Douaud, G., Beckmann, C. F., Glasser, M. F., Griffanti, L., and Smith, S. M. (2014). Automatic denoising of functional MRI data: Combining independent component analysis and hierarchical fusion of classifiers. *NeuroImage*, 90:449–468.
- Satterthwaite, T. D., Elliott, M. A., Gerraty, R. T., Ruparel, K., Loughhead, J., Calkins, M. E., Eickhoff, S. B., Hakonarson, H., Gur, R. C., Gur, R. E., and Wolf, D. H. (2013). An improved framework for confound regression and filtering for control of motion artifact in the preprocessing of resting-state functional connectivity data. *NeuroImage*, 64(1):240–256.
- Satterthwaite, T. D., Wolf, D. H., Loughhead, J., Ruparel, K., Elliott, M. A., Hakonarson, H., Gur, R. C., and Gur, R. E. (2012). Impact of In-Scanner Head Motion on Multiple Measures of Functional Connectivity: Relevance for Studies of Neurodevelopment in Youth. *NeuroImage*, 60(1):623–632.

- Saxena, A. (2005). Congenital Heart Disease in India: A Status Report. *Indian Journal of Pediatrics*, 72(7):595–598.
- Shah, G., Singh, M., Pandey, T., Kalakheti, B., and Bhandari, G. (2008). Incidence of congenital heart disease in tertiary care hospital. *Kathmandu University Medical Journal*, 6(1):33–36.
- Shannon, C. E. (1948). A Mathematical Theory of Communication. *Bell System Technical Journal*, 27(3):379–423.
- Shirer, W. R., Ryali, S., Rykhlevskaia, E., Menon, V., and Greicius, M. D. (2012). Decoding subject-driven cognitive states with whole-brain connectivity patterns. *Cerebral Cortex*, 22(1):158–165.
- Smith, S. M., Jenkinson, M., Woolrich, M. W., Beckmann, C. F., Behrens, T. E. J., Johansenberg, H., Bannister, P. R., Luca, M. D., Drobnjak, I., Flitney, D. E., Niazy, R. K., Saunders, J., Vickers, J., Zhang, Y., Stefano, N. D., Brady, J. M., and Matthews, P. M. (2004). Advances in functional and structural MR image analysis and implementation as FSL. *NeuroImage*, 23:208–219.
- Smyser, C. D., Inder, T. E., Shimony, J. S., Hill, J. E., Degnan, A. J., Snyder, A. Z., and Neil, J. J. (2010). Longitudinal analysis of neural network development in preterm infants. *Cerebral Cortex*, 20(12):2852–2862.
- Smyser, C. D. and Neil, J. J. (2015). Use of resting state functional MRI to study brain development and injury in neonates. *Seminars in Perinatology*, 39(2):130–140.
- Smyser, C. D., Snyder, A. Z., and Neil, J. J. (2011). Functional connectivity MRI in infants: exploration of the functional organization of the developing brain. *NeuroImage*, 56(3):1437–52.
- Togo, H., Rokicki, J., Yoshinaga, K., Hisatsune, T., Matsuda, H., Haga, N., and Hanakawa, T. (2017). Effects of field-map distortion correction on resting state functional connectivity MRI. *Frontiers in Neuroscience*, 11(DEC):1–10.
- TracInnovations (2019). Tracinnovations mri markerless motion tracker and monitor system.
- United States Food and Drug Administration (2016). Drug Safety and Availability - FDA Drug Safety Communication: FDA review results in new warnings about using general anesthetics and sedation drugs in young children and pregnant women. Technical report, United States Food and Drug Administration.
- van der Linde, D., Konings, E. E., Slager, M. A., Witsenburg, M., Helbing, W. A., Takkenberg, J. J., and Roos-Hesselink, J. W. (2011). Birth Prevalence of Congenital Heart Disease Worldwide. *Journal of the American College of Cardiology*, 58(21):2241–2247.
- van der Maaten, L. and Hinton, G. (2008). Visualizing data using t-SNE. *Journal of Machine Learning Research*, 9(Nov):2579—2605.

- van Dijk, K. R., Hedden, T., Venkataraman, A., Evans, K. C., Lazar, S. W., and Buckner, R. L. (2010). Intrinsic functional connectivity as a tool for human connectomics: Theory, properties, and optimization. *Journal of Neurophysiology*, 103(1):297–321.
- van Dijk, K. R., Sabuncu, M. R., and Buckner, R. L. (2012). The influence of head motion on intrinsic functional connectivity MRI. *NeuroImage*, 59(1):431–438.
- Varoquaux, G. (2019). K-means Clustering.
- Ward, J. H. . (1963). Hierarchical Grouping to Optimize an Objective Function. *Journal of the American Statistical Association*, 58(301):236–244.
- Waskom, M. L. (2018). seaborn.clustermap.
- Webb, G., Mulder, B. J., Aboulhosn, J., Daniels, C. J., Elizari, M. A., Hong, G., Horlick, E., Landzberg, M. J., Marelli, A. J., O'Donnell, C. P., Oechslin, E. N., Pearson, D. D., Pieper, E. P., Saxena, A., Schwerzmann, M., Stout, K. K., Warnes, C. A., and Khairy, P. (2015). The care of adults with congenital heart disease across the globe: Current assessment and future perspective: A position statement from the International Society for Adult Congenital Heart Disease (ISACHD). *International Journal of Cardiology*, 195:326–333.
- Windram, J. D., Grosse-Wortmann, L., Shariat, M., Greer, M.-L., and Yoo, S.-J. (2011). The Feed and Sleep method: how to perform a cardiac MRI in the 1st year of life without the need for General Anesthesia. *Journal of Cardiovascular Magnetic Resonance*, 13(Suppl 1):P224.
- Woolrich, M. W., Behrens, T. E. J., Beckmann, C. F., Jenkinson, M., and Smith, S. M. (2004). Multilevel linear modelling for fMRI group analysis using Bayesian inference. *NeuroImage*, 21:1732–1747.
- Yan, C. G., Cheung, B., Kelly, C., Colcombe, S., Craddock, R. C., Di Martino, A., Li, Q., Zuo, X. N., Castellanos, F. X., and Milham, M. P. (2013a). A comprehensive assessment of regional variation in the impact of head micromovements on functional connectomics. *NeuroImage*, 76:183–201.
- Yan, C.-G., Craddock, R. C., He, Y., and Milham, M. P. (2013b). Addressing head motion dependencies for small-world topologies in functional connectomics. *Frontiers in Human Neuroscience*, 7(December):1–19.
- Zaitsev, M., Burak, A., LeVan, P., and Knowles, B. R. (2017). Prospective Motion Correction in Functional MRI. *NeuroImage*, pages 33–42.
- Zaitsev, M., Dold, C., Sakas, G., Hennig, J., and Speck, O. (2006). Magnetic resonance imaging of freely moving objects: prospective real-time motion correction using an external optical motion tracking system. *NeuroImage*, 31(3):1038–1050.

- Zang, Y. F., Yong, H., Chao-Zhe, Z., Qing-Jiu, C., Man-Qiu, S., Meng, L., Li-Xia, T., Tian-Zi, J., and Yu-Feng, W. (2007). Altered baseline brain activity in children with ADHD revealed by resting-state functional MRI. *Brain and Development*, 29(2):83–91.
- Zhao, Q. M., Liu, F., Wu, L., Ma, X. J., Niu, C., and Huang, G. Y. (2019). Prevalence of Congenital Heart Disease at Live Birth in China. *Journal of Pediatrics*, 204:53–58.
- Zijdenbos, A. P., Dawant, B. M., Margolin, R. A., and Palmer, A. C. (1994). Morphometric Analysis of White Matter Lesions in MR Images: Method and Validation. *IEEE Transactions on Medical Imaging*, 13(4):716–724.
- Zou, K. H., Warfield, S. K., Bharatha, A., Tempany, C. M., Kaus, M. R., Haker, S. J., Wells, W. M., Jolesz, F. A., and Kikinis, R. (2004). Statistical Validation of Image Segmentation Quality Based on a Spatial Overlap Index. *Academic Radiology*, 11(2):178–189.